Inverse Statistical Mechanics, Lattice Packings, and Glasses

Étienne Marcotte

A Dissertation
Presented to the Faculty
of Princeton University
in Candidacy for the Degree
of Doctor of Philosophy

Recommended for Acceptance
by the Department of
Physics
Adviser: Salvatore Torquato

November 2013

Abstract

Computer simulation methods enable the investigation of systems and properties that are intractable by purely analytical or experimental approaches. Each chapter of this dissertation contains an application of simulation methods to solve complex physical problems consisting of interacting many-particle or many-spin systems. The problems studied in this dissertation can be divided up into the following two broad categories: *inverse* and *forward* problems.

The inverse problems considered are those in which we construct an interaction potential such that the corresponding ground state is a targeted configuration. In Chapters 2 and 3, we devise convex pair-potential functions that result in low-coordinated ground states. Chapter 2 describes targeted ground states that are the square and honeycomb crystals, while in Chapter 3 the targeted ground state is the diamond crystal. Chapter 4 applies similar techniques to explicitly enumerate all unique ground states up to a given system size, for spin configurations that interact according to generalized isotropic Ising potentials with finite range.

We also consider forward statistical-mechanical problems. In Chapter 5, we adapt a linear programming algorithm to find the densest lattice packings across Euclidean space dimensions. In Chapter 6, we demonstrate that for two different glass models a signature of the glass transition is apparent well before the transition temperature is reached. In both models, this signature appears as nonequilibrium length scales that grow upon supercooling.

Acknowledgements

I offer my most profound thanks to my advisor, Professor Salvatore Torquato, for the guidance he offered me during the five years I was at Princeton University. This dissertation would not exist without his encouragements and intriguing project ideas. I also thank Frank H. Stillinger, with whom I collaborated for many of my projects, for sharing his insight and knowledge with me.

I thank all of my fellow group members, Yang Jiao, Robert D. Batten, Chase E. Zachary, Adam B. Hopkins, Ge Zhang, Steven Atkinson, Duyu Chen, Miroslav Hejna, Ruggero Gabbrielli, and Cédric J. Gommes, for the many fascinating and enlightening discussions we had over the years. I am furthermore indebted to Robert A. DiStasio Jr and Gregory J. Finkelstein for their help in writing this dissertation.

Finally, I am deeply grateful for everyone who supported me this far, most importantly my parents, Sylvie and Patrice.

Part of this work has been financially supported by the Natural Science and Engineering Council of Canada and the Fonds Québécois de la Recherche sur la Nature et les Technologies.

Contents

List of Tables

List of Figures

Chapter 1

Introduction

The properties of many interacting systems cannot be successfully studied using analytical statistical-mechanical approaches, either due to complex interactions or behaviors that only become apparent at large length scales. Instead, advanced simulation techniques must be used. Even some of the most fundamental properties of seemingly simple models, such as the ground state configuration of particles that interact according to the well-studied Lennard-Jones potential, have still not been fully demonstrated through analytical proofs. This dissertation is dedicated to answering some fascinating questions about statistical-mechanical models that have so far remained intractable through the use of purely analytical methods.

The first question that this dissertation addresses is whether or not it is possible for many-particle systems that interact according to purely radial and repulsive potentials to self-assemble into low-coordinated structures as classical ground states. The second question is a generalization of the first, but for a different class of materials: what configurations can a spin system relax to at zero temperature if the spins interact according to a radial potential with a finite range? The last two topics are distinctly different. We ask if the densest lattice sphere packings currently known are indeed the densest possible, and whether supercooled liquids have some glass signature prior

to reaching the glass transition temperature. The following paragraphs provide an outline for how each of these questions is answered.

Statistical-mechanical methods involving ground-state configurations of interacting systems fall into two distinct approaches: *forward* and *inverse* methods. With forward methods, one starts with a single interaction and computes the corresponding ground state (or any other emergent property) of a system using a variety of techniques, such as explicit enumeration of configurations, energy minimization, and many others. If a specific ground-state configuration is desired, the only recourse of forward methods is to try a wide variety of different interactions until the ground state matches the target. Inverse methods work in the opposite direction: starting from a given target configuration, such methods seek to discover an interaction which leads the system to have the desired configuration as its ground state. It should be mentioned that the use of one approach does not preclude the use of the other. For instance, direct methods are of great importance when using inverse methods in allowing us to explicitly verify whether or not the inverse method resulting interaction is valid. Furthermore, while this dissertation only tackles the challenge of finding interactions with given ground states, inverse methods are not restricted to this problem. For example, inverse methods can be applied to the design of materials with specific properties in mind.

Systems consisting of identical point particles with no internal degrees of freedom (rotational or otherwise), and which behavior is described by a potential function that only depends on the distance between each pair of particles are able to accurately model a wide variety of physical systems. While the behavior of such systems can vary due to thermodynamical variables, such as temperature or pressure, their most important property lies in the potential function that describes the underlying interaction between any particle pair. If the potential function has a well at a specific distance, then it is intuitively understandable that in the system ground state, the

particles will tend to arrange themselves such that they are separated by that characteristic distance. In the case of a purely repulsive potential function, intuition leads us to believe that the particles will try to be as far as possible from one another and thus the ground state should be a dense packing, which maximizes nearest-neighbor distances for a given density. Chapter 2 demonstrates that this intuitive answer is incorrect, and that purely repulsive isotropic pair potentials in two-dimensional Euclidean space can lead to low-coordinated ground states, such as the square and honeycomb crystals. As such, the results in Chapter 2 were previously published as:

- É. Marcotte, F. H. Stillinger, and S. Torquato, *Optimized Monotonic Convex Pair Potentials Stabilize Low-Coordinated Crystals*, Soft Matter **7**, 2332 (2011).
- É. Marcotte, F. H. Stillinger, and S. Torquato, *Unusual Ground States via Monotonic Convex Pair Potentials*, J. Chem. Phys. **134**, 164105 (2011).

Chapter 3 continues with another inverse problem, namely to show that purely repulsive isotropic pair potentials in three-dimensional Euclidean space can also lead to low-coordinated ground states; in particular, such potentials can lead to a four-coordinated diamond crystal ground state. The results in Chapter 3 were also previously published as:

- É. Marcotte, F. H. Stillinger, and S. Torquato, *Designed Diamond Ground State via Optimized Isotropic Monotonic Pair Potentials*, Journal of Chemical Physics **138**, 061101 (2013).

Many-particle systems are not the only classical models of interest in this dissertation. For instance, such models cannot accurately represent magnetic solids, where each magnetic atom is fixed in space, but can vary in magnetic orientation (spin). Chapter 4 is an enumeration study using inverse statistical-mechanical techniques similar to those employed in Chapters 2 and 3 to discover all spin configurations (up to modest size governed only by computational resources) that can be unique ground

states of an isotropic spin-spin potential. This ability to find all possible unique ground states does not simply rely on the feasibility of enumerating spin configurations (as there exists only a finite number of them for a given system size), but also on the fact that the techniques used herein can rigorously prove that specific spin configurations can never be unique ground states for any spin-spin potential with finite range. The results in Chapter 4 have been submitted, and will appear as:

- É. Marcotte, R. A. DiStasio Jr, F. H. Stillinger, and S. Torquato, *Designer Spin Systems via Inverse Statistical Mechanics II: Ground State Enumeration and Classification*, Phys. Rev. B (submitted).

This dissertation not only contains inverse statistical-mechanics topics, but also some that belong squarely in the realm of direct statistical mechanics. One such topic is the search for the densest configuration (packing) of non-overlapping identical spheres in d-dimensional Euclidean space. This is strictly equivalent to calculating the ground state of a many-particle system in which the pair potential function is infinite for distances within the sphere diameter and identically zero beyond it, under positive pressure. Chapter 5 presents a numerical method to quickly solve this problem across Euclidean space dimensions, although it is restricted to configurations where the spheres form a lattice. While this method was not able to discover denser lattice packings than those that were already known in the literature, it is much faster than other known algorithms and allows us to find many new nearly-optimal lattice packings. The results in Chapter 5 were previously published as:

- É. Marcotte and S. Torquato, *Efficient Linear Programming Algorithm to Generate the Densest Lattice Sphere Packings*, Physical Review E **87**, 063303 (2013).

This dissertation concludes with Chapter 6, which contains the sole project that is not concerned with ground states. In Chapter 6, we instead search for signatures of long-range order of many-particle systems as they are rapidly cooled past their

freezing temperature, resulting in non-equilibrium supercooled liquids. We show the existence of nonequilibrium static growing length scales in these supercooled liquids as they approach the glass transition. For this purpose, the interactions within the many-particle systems are chosen to be those for which obtaining the ground state is nearly impossible, allowing us to study their supercooled liquid phases without crystallization. The results in Chapter 6 were previously published as:

- É. Marcotte, F. H. Stillinger, and S. Torquato, *Nonequilibrium Static Growing Length Scales in Supercooled Liquids on Approaching the Glass Transition*, Journal of Chemical Physics **138**, 12A508 (2013).

Each chapter of this dissertation is meant to be read individually, since it describes a particular project. As such, each chapter has its own introduction, conclusion, and bibliography. Other than Chapter 2, which should be read before Chapters 3 and 4, the chapters can be read in any order.

Chapter 2

Unusual Ground States via Monotonic Convex Pair Potentials

2.1 Introduction

The study of particle self-assembly has been an ongoing area of research since Whitesides [1] coined the term two decades ago. Self-assembly is defined as the spontaneous organization of particles, be they atoms, molecules or supramolecules, into a given many-particle configuration. This organization occurs without any external force through noncovalent interaction between the particles. Naturally occurring examples include the formation of DNA double helices, lipid bilayers, and ionic crystals.

There are two main methods one can take to design self-assembling systems: the forward and the inverse approaches. The forward approach begins with a many-particle system with specified interactions, and obtains the stable many-particle configuration. This approach, used both computationally and experimentally, has led to the discovery of a wide variety of novel many-particle configurations [2, 3, 4, 5, 6, 7, 8, 9], but is not best suited to find new many-particle configurations with targeted properties. To do this, it is necessary to use the inverse approach, which attempts to

find the optimal interactions that yield a targeted many-particle configuration with desirable bulk physical properties.

This work continues our program on using inverse approaches to optimize pair interactions to achieve novel targeted ground-state configurations in d-dimensional Euclidean space $\mathbb{R}^d$. Previous investigations reported optimized pair interactions that stabilize low-coordinated crystals as ground states, including the square and honeycomb crystals [10] in $\mathbb{R}^2$ and simple cubic [11] and diamond [12] crystals in $\mathbb{R}^3$, materials with negative thermal expansion [13], and negative Poisson's ratio [14]. Moreover, potentials possessing disordered ground states [15, 16] have been produced with novel optical properties [16, 17]. We envision using colloids and/or polymers to realize such designed potentials because it is possible to manipulate and control their interactions [6, 18, 19, 20].

Earlier uses of the inverse approach [10] did not regard experimental feasibility as a constraint. These investigations allowed a largely unconstrained class of spherically symmetric pair potentials. In some of these instances, multiple potential wells were utilized to achieve the desired target configurations [10, 12], which may be difficult to realize experimentally. Our objective in the present study is to stabilize low-coordinated crystal configurations in Euclidean space, restricting ourselves to a class of monotonically decreasing pair potentials, which are relatively easy to produce experimentally. However, encoding information in monotonic potentials to yield low-coordinated ground-state configurations in Euclidean space is nontrivial. These potentials must not only successfully discriminate against close-packed (highly coordinated) crystal configurations, but also the infinitesimally close configurations obtained by slightly deforming the target crystal. In addition, both of these theoretical challenges are further complicated by the monotonicity constraint.

We are motivated by the work of Cohn and Kumar [21], who have rigorously constructed potentials that stabilize unusual targeted configurations on the surface

of a d-dimensional sphere using only monotonic convex pair potentials. A crucial difference between the work of Ref. [21] and this study is that we consider noncompact (infinite) Euclidean spaces. The fact that Cohn and Kumar restricted themselves to compact spaces made their problem comparatively easy to solve because their pair potentials had compact support set by the sphere radius. A consequence of using repulsive monotonic potentials is that the studied systems are required to be under positive pressure, a condition that is easily enforceable experimentally.

In this chapter, we specifically use the inverse approach to obtain repulsive monotonic convex potentials whose ground states in $\mathbb{R}^2$ are either the square lattice or the honeycomb crystal. Thus, our work is a theoretical proof of concept that monotonic convex potentials can counterintuitively stabilize low-coordinated two-dimensional crystals. A summary of preliminary results is available [22], but in this chapter we present a detailed explanation of our numerical methods, a complete analysis of the stability of the resulting crystalline ground states, and a thorough demonstration of how monotonic convex potentials can stabilize the studied unusual ground states. To better explain the characteristic features of the optimized potentials, we introduce a new measure, the *generalized coordination functions*, which to our knowledge have not been previously used. We show the utility of these functions to enable the stabilization of the square and honeycomb crystals via a large family of potential functions.

This chapter is organized as follows: Sec. 2.2 is devoted to a technical explanation of how the new potentials are devised. Section 2.3 presents the family of monotonic convex potentials that we use and analyzes their energetic and mechanical-stability properties for the square and honeycomb crystal ground states. We also relax the convexity condition to see whether the square lattice can still be produced as a ground-state configuration. Finally, Sec. 2.4 summarizes the impacts of these new results and speculates on how they could be extended.

2.2 Theory

2.2.1 Background

Pair potentials

We consider a system of N particles, with positions $\mathbf{r}_1$, $\mathbf{r}_2$, ..., $\mathbf{r}_N$ in a volume V contained in $\mathbb{R}^d$. In the absence of an external field, the potential energy of the system $\Phi_N\left(\mathbf{r}^N\right)$ is a function of the particle positions:

$$\Phi_N\left(\mathbf{r}^N\right) = \sum_{i<j} v_2(\mathbf{r}_i, \mathbf{r}_j) + \sum_{i<j<k} v_3(\mathbf{r}_i, \mathbf{r}_j, \mathbf{r}_k) + \cdots, \tag{2.1}$$

where the v_n are the intrinsic n-particle potentials. Our focus is on those cases in which only the pair potential v_2 is present, and where it is also isotropic (*i.e.*, a radial function): $v_2(\mathbf{r}_i, \mathbf{r}_j) \equiv v(r_{ij})$, with $r_{ij} = |\mathbf{r}_i - \mathbf{r}_j|$. This reduces the total potential expression to

$$\Phi_N\left(\mathbf{r}^N\right) = \sum_{i<j} v(r_{ij}). \tag{2.2}$$

We recognize that systems encountered in the laboratory typically exhibit some non-pairwise contributions, but we defer for later study how these contributions could be minimized by selection of the specific systems for analysis, and what their residual effects would be.

If the number density $\rho = N/V$ is kept constant, Φ_N is asymptotically proportional to N, so it is useful to define a normalized energy value using their ratio. In this chapter, a key quantity that we will consider is twice the energy per particle, *i.e.*,

$$u = 2\Phi_N/N. \tag{2.3}$$

Finding the classical ground state

For a system with a given number of particles N in some volume V and with a potential energy function $\Phi_N\left(\mathbf{r}^N\right)$, the classical ground state is defined as the configuration set of the particles positions $\mathbf{r}^N$ with the globally minimal potential energy. To find the putative targeted ground states, we use the well-known simulated annealing method [10]. We begin with an initial configuration of N particles chosen from a Poisson point process in a box of volume V with periodic boundary conditions. Initially, a large temperature T is selected and the particles are moved according to the Metropolis Monte Carlo algorithm. The temperature T is then gradually reduced to zero. If this procedure is done slowly enough, the resulting configuration is likely the ground state. To improve the efficiency of our method, we use a steepest-descent method to relax the particles at the end of the simulated annealing. Furthermore, since simulated annealing calculations tend often to become trapped in deep local minima, we repeat this process many times, only keeping the final configuration with the lowest potential energy.

2.2.2 Methodology

Functional form

To simplify the notation, let us define a configuration C as a set of particle positions $\mathbf{r}_1, \mathbf{r}_2, \ldots$ in $\mathbb{R}^d$. A configuration defined in this sense is perfectly general, incorporating both periodic as well as disordered point processes.

Let us assume that a certain pair potential v has the target configuration C^* as its ground state. Thus, we have

$$u(v, C^*) \leq u(v, C) \qquad \forall C, \tag{2.4}$$

where u is defined by relation (2.3). Intuitively, it should be possible to find a valid potential v by expressing it in terms of a list of M parameters $a_1, \ldots, a_M$, and varying the parameters until inequality (2.4) is satisfied for all possible configurations:

$$v \equiv v(a_1, \ldots, a_M). \tag{2.5}$$

Since checking all possible configurations is impossible (because there is an uncountably infinite number of them), we restrict ourselves to a subset, which we call the "competitor" configurations $\mathbf{C}$. In this way, we can redefine the problem as an optimization [10], where we seek to maximize the energy difference between the targeted configuration C^* and its closest competitor configurations. To do so, we introduce Δ, a utility variable which is maximized while constrained by:

$$u\big(v(a_1, \ldots, a_M), C^*\big) \leq u\big(v(a_1, \ldots, a_M), C\big) - \Delta \qquad \forall C \in \mathbf{C}. \tag{2.6}$$

For a given potential v, Δ can be as large as the smallest energy difference, $u\left(v, C\right) - u\left(v, C^*\right)$, between a competitor and the targeted configurations. Therefore, allowing v to vary the optimization procedure enables us to find the potential that maximizes the energy difference between the target configuration and its closest competitor.

In the case where we do not want all competitors to be treated on an equal footing and seek to prioritize some of them, we can add a modulating factor $m(C)$ to the inequality:

$$u\big(v(a_1, \ldots, a_M), C^*\big) \leq u\big(v(a_1, \ldots, a_M), C\big) - m(C)\Delta \qquad \forall C \in \mathbf{C}. \tag{2.7}$$

One particularly useful property of the modulating factor is that it can be chosen to be very small for configurations close to C^*. Even the limiting case $C^* \in \mathbf{C}$ can be considered if $m(C^*) = 0$ is enforced.

Potential form

For inequality (2.7) to be usable, $v(\{a_i\})$, $\mathbf{C}$ and $m(S)$ must be defined. The first choice to be made is the form of the pair potential function $v(\{a_i\})$. Since inequality (2.7) is linear with respect to twice the energies per particle $u(v, C)$, and the $u(v, C)$ are linear in terms of the pair potential $v(\{a_i\})$ for each configuration C, making the pair potential linear in the parameters $\{a_i\}$ ensures the overall linearity of the system:

$$v(r) = \sum_{i=1}^{M} a_i f_i(r), \tag{2.8}$$

$$\Phi(v, C) = \sum_{j<k} \sum_{i=1}^{M} a_i f_i(r_{jk}) = \sum_{i=1}^{M} a_i \left[\sum_{j<k} f_i(r_{jk}) \right]. \tag{2.9}$$

This simplifies the optimization problem, since it allows one to use many of the standard linear programming methods to determine the optimal parameters, such as the simplex algorithm. Another advantage of using a linear form for the pair potential is apparent from Eq. (2.9): we need only to sum over all particle pairs once for a given configuration, greatly reducing the computational cost. It bears mentioning that the sums over j and k are over *all* particles of the configuration, making them infinite in the large system limit. However, if the configuration is periodic, by using u instead of Φ, the normalized sum reverts to a bounded lattice sum.

For this chapter, the $f_i(r)$ are taken to be negative powers of r, with a common cutoff at some distance $R > 0$:

$$v(r) \equiv \begin{cases} \displaystyle\sum_{i=1}^{M} \frac{a_i}{r^i} & r \leq R, \\ 0 & r > R. \end{cases} \tag{2.10}$$

Since we not only desire to have both the pair potential $v(r)$ and the corresponding force $-dv/dr$ be continuous, but need also to be able to calculate phonon spectra, we

require $v(r)$ and both its first and second derivatives to be continuous at $r = R$. This is equivalent to adding the following constraints:

$$\begin{aligned} \sum_{i=1}^{M} \frac{a_i}{R^i} &= 0, \\ \sum_{i=1}^{M} \frac{i a_i}{R^{i+1}} &= 0, \\ \sum_{i=1}^{M} \frac{i(i+1) a_i}{R^{i+2}} &= 0. \end{aligned} \tag{2.11}$$

The rationale for using the functions from Eq. (2.10) is that they can accurately reproduce most other functions since they become Taylor series in terms of $1/r$ as M and R grow larger. Additionally, they can naturally reproduce a quasi-hard-core repulsion: $\lim_{r \to 0^+} v(r) = \infty$, as long as $a_M > 0$. Other potentials have been tried, such as those involving positive powers of r, but numerical experiments show that they are less stable and more affected by numerical imprecisions, particularly with longer cutoffs.

It is easy to see from Eq. (2.7) that multiplying all of the a_i by some positive constant amounts to multiplying the objective Δ by the same constant. From there, it is clear that the problem as written is not bounded, and that if it is possible to obtain a solution for which Δ is greater than zero, then solutions exist for any positive Δ, including arbitrarily large values. To impose a scale, we fix the value of the potential at the nearest-neighbor distance of the target configuration as unity, which leads to the following constraint:

$$v(r = 1) = \sum_{i=1}^{M} a_i = 1. \tag{2.12}$$

Additionally, the a_i are all constrained to be in the $[-1000, +1000]$ range, since the problem still is not totally bounded after fixing $v(r = 1)$.

While previous papers [10, 11, 12] have succeeded in obtaining pair potentials resulting in specific crystal ground-state configurations, their functions use extrema (minima and maxima) to either favor or disfavor certain nearest neighbor distances. Doing so may allow the determination of pair potentials with the desired classical ground state, but at the same time, leads to potentials that may not be experimentally realizable. In an attempt to find potentials that are more experimentally feasible, two additional constraints have been added: $v(r)$ must be both monotonically decreasing [for all $r' > r$, $v(r') \leq v(r)$] and convex [for all r, r' and $b \in [0,1]$, $v\left(br + (1-b)r'\right) \leq bv(r) + (1-b)v(r')$]. For our potential form, these conditions can be written as:

$$-\frac{dv}{dr} = \sum_{i=1}^{M} \frac{ia_i}{r^{i+1}} \quad \geq \quad 0 \qquad \forall r < R, \tag{2.13}$$

$$\frac{d^2v}{dr^2} = \sum_{i=1}^{M} \frac{i(i+1)a_i}{r^{i+2}} \quad \geq \quad 0 \qquad \forall r < R. \tag{2.14}$$

Inequalities (2.13) and (2.14) are both linear. However, they introduce a condition for every possible value of r. To avoid the numerical impossibility of dealing with an infinite number of conditions, we restrict ourselves to a large, but finite, number of values of r at which we enforce the conditions.

Competitors

Once the functional form is chosen, the competitor set $\mathbf{C}$ and modulation $m(C)$ still have to be selected. Since a well chosen $\mathbf{C}$ is sufficient to either find, or disprove, the existence of a potential with the desired ground state, here we restrict ourselves to a constant $m(C) = 1$ modulation. However, such a choice puts all competitors on an equal footing, which often results in potentials that do not discriminate against distinctly different configurations.

The method employed to specify $\mathbf{C}$ is to start with it containing only a single competitor (typically the triangular lattice) and to create a trial potential v_1 from

that initial $\mathbf{C}$, as described in Sec. 2.2.2. After calculating the trial potential ground state C_1, its energy with the trial potential is compared with that of the targeted configuration C^*. If the energy of C_1 is lower than that of C^*, the trial potential is incorrect, so we add C_1 to the set of competitors and repeat the process with a new trial potential v_2. Otherwise, the ground state of the trial potential is the target configuration and the trial potential is the desired potential [23].

Our method is an adaptation of the one presented by Cohn and Kumar [21]. It was modified to use simulated annealing instead of a gradient descent method to find the ground states of the trial potentials due to the typically numerous local minima of the $\Phi_N\left(\mathbf{r}^N\right)$ energy landscape, which makes it almost impossible to find the ground state by simply using a gradient descent technique. A second difference is that we only add configurations to the set of competitors if they have a lower energy than the target for the current trial potential. Adding all of the obtained configurations was found to be highly unstable because imperfect energy minimizations led to adding configurations close to the target, causing inequality (2.7) to only consider close competitors.

Eventually, this algorithm will, in principle, find an optimal potential v^*, or prove that no such potential exists with the functional form used. But to do so, an infinite number of iterations can be required, since over time it fills $\mathbf{C}$ with all possible configurations but C^*, reverting slowly to inequality (2.4). In practice, this is not necessary. For most, but not all, of the studied target configurations in two-dimensions, having only the triangular lattice as a competitor is enough to find an optimal potential.

2.2.3 Generalized coordination functions

For isotropic pair potentials, the list of the neighbor separations and their multiplicities is a crucial piece of information for understanding which configurations are energetically favorable. However, while this list is useful when dealing with pair potentials that have well-defined minima or maxima, it does not convey much information

for strongly constrained pair potentials, such as the monotonic convex potentials considered in this chapter. Therefore, we introduce *generalized coordination functions*, a new measure that amplifies the differences between configurations that are relevant to the restricted potentials. This is preferred, especially if such differences can be correlated to the features of the potentials. Of particular interest are the *coordination functions of order n*, which apply to potentials that have n-th order derivatives restricted to either being non-negative or non-positive (depending on the parity of n).

Writing u, twice the energy per particle [cf. Eq. (2.3)], in terms of the set of particle positions C, we get:

$$u = \frac{1}{N} \sum_{\mathbf{p} \neq \mathbf{q} \in C} v(|\mathbf{p} - \mathbf{q}|). \tag{2.15}$$

By replacing the sum with an integral using delta functions, we now have a function that describes the radial distribution of the neighbors,

$$u = \int_{r=0}^{\infty} dr v(r) \left[\frac{1}{N} \sum_{\mathbf{p} \neq \mathbf{q} \in C} \delta(r - |\mathbf{p} - \mathbf{q}|) \right] = \int_{r=0}^{\infty} dr v(r) \mathcal{Z}_0(r), \tag{2.16}$$

where $\mathcal{Z}_0(r)$ is the coordination function of order 0, defined as:

$$\mathcal{Z}_0(r) \equiv \frac{1}{N} \sum_{\mathbf{p} \neq \mathbf{q} \in C} \delta(r - |\mathbf{p} - \mathbf{q}|). \tag{2.17}$$

Assuming that $\mathcal{Z}_0(r)$ is zero at $r = 0$, and that $v(r)$ and all its derivatives go to zero as r goes to infinity, we can use integration by parts to write u as a function of the derivatives of $v(r)$. Let us first define the coordination function of order n, $\mathcal{Z}_n(r)$, recursively:

$$\mathcal{Z}_{n+1}(r) \equiv \int_{r'=0}^{r} dr' \mathcal{Z}_n(r'). \tag{2.18}$$

Then, we have

$$\begin{aligned} u &= \int_{r=0}^{\infty} dr v(r) \mathcal{Z}_0(r), && (2.19) \\ &= \left(\frac{dv}{dr} \mathcal{Z}_1(r) \right)_{r=0}^{\infty} - \int_{r=0}^{\infty} dr \frac{dv}{dr} \mathcal{Z}_1(r), && (2.20) \\ &= -\int_{r=0}^{\infty} dr \frac{dv}{dr} \mathcal{Z}_1(r). && (2.21) \end{aligned}$$

The integration by parts can be repeated as many times as $v(r)$ is differentiable:

$$u = (-1)^n \int_{r=0}^{\infty} dr \frac{d^n v}{dr^n} \mathcal{Z}_n(r). \tag{2.22}$$

Equation (2.22) is particularly relevant when we restrict ourselves to pair potentials with constrained derivatives. As an example, if we know that for two distinct configurations A and B that $\mathcal{Z}_2^A(r) < \mathcal{Z}_2^B(r)$ for all values of r, then the configuration A will always have a lower energy than the configuration B in the presence of a convex pair potential. Hence, no such potential will have the configuration B as a ground state.

The $\mathcal{Z}_n(r)$ functions can be generalized to yield information for any problem where it is possible for the pair potential to be expressed as a linear combination of a family of functions $f(r,s)$: $v(r) = \int_s ds c(s) f(r,s)$, especially when the coefficients $c(s)$ are restricted to be non-negative:

$$\begin{aligned} u &= \int_{r=0}^{\infty} dr v(r) \mathcal{Z}_0(r), && (2.23) \\ &= \int_{r=0}^{\infty} dr \int_s ds c(s) f(r,s) \mathcal{Z}_0(r), && (2.24) \\ &= \int_s ds c(s) \int_{r=0}^{\infty} dr f(r,s) \mathcal{Z}_0(r), && (2.25) \\ &= \int_s ds c(s) \widetilde{\mathcal{Z}}_f(s). && (2.26) \end{aligned}$$

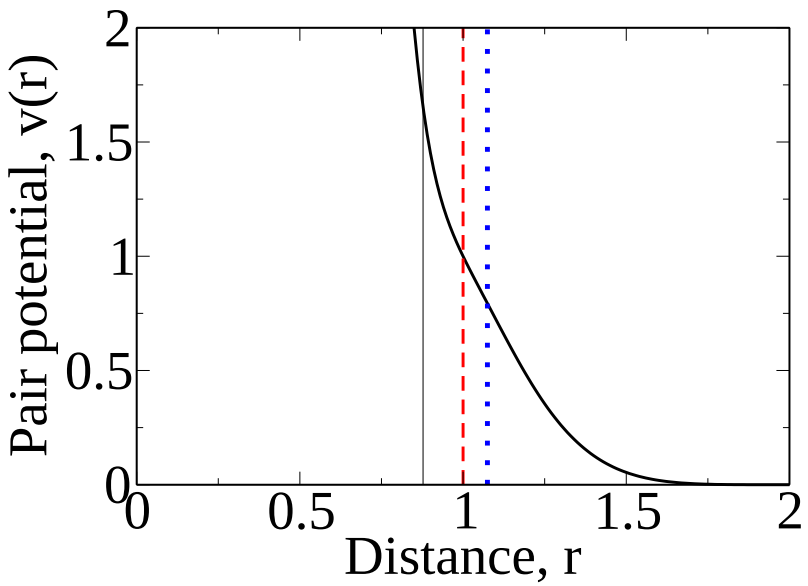

Figure 2.1: (Color online) Optimized monotonic convex pair potential from Eq. (2.28) targeting the square lattice at unit number density. The three vertical lines represent the nearest-neighbor distances for the honeycomb crystal (black solid), the square lattice (red dashed) and the triangular lattice (blue dotted) at the same number density. The value of $v(r)$ at these distances is 1.6542, 1 and 0.7937, respectively.

Here $\widetilde{\mathcal{Z}}_f(s)$ (the subscript f denoting a family of functions) is defined as:

$$\widetilde{\mathcal{Z}}_f(s) \equiv \int_{r=0}^{\infty} dr f(r,s)\mathcal{Z}_0(r). \tag{2.27}$$

Equation (2.22) can be obtained from Eq. (2.26) by using $c(s) = (-1)^n \frac{d^n v}{dr^n}(r = s)$ and $f(r,s) = \Theta(s-r)(s-r)^{n-1}/(n-1)!$.

2.3 Results

The method presented in Sec. 2.2.2 is applied to two target configurations in two-dimensions: the square and honeycomb crystals. The obtained optimized pair potentials and their properties are presented in Sec. 2.3.1 and 2.3.2, respectively.

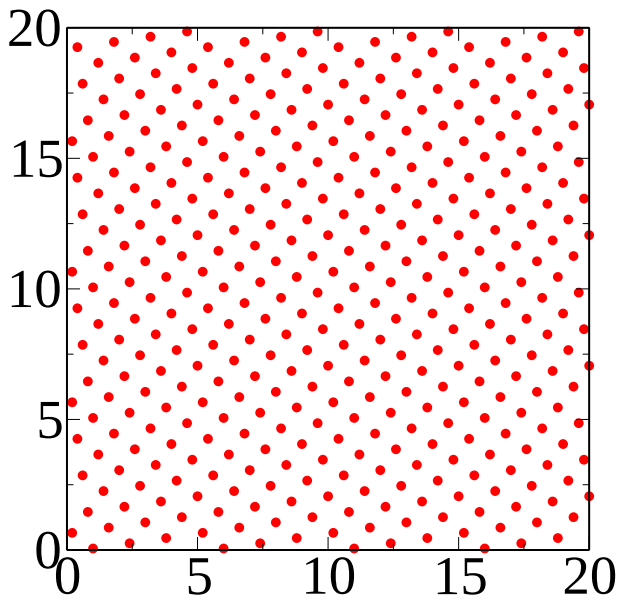

Figure 2.2: (Color online) Ground state of the potential (2.28) with 400 particles in a 20×20 box with periodic boundary conditions as obtained by slowly annealing the system starting from a fluid. For illustration purposes, the point particles are shown to have finite sizes. This rotated square lattice has the same u as would a square lattice aligned with the box boundaries.

2.3.1 Square lattice

Consider a square lattice with a nearest neighbor distance of unity as the target configuration. We restrict our optimization to monotonic convex pair potentials with a cutoff of $R = 2$. The simulated-annealing optimization method results in the following pair potential:

$$v(r) = \begin{cases} \left(\dfrac{28.424}{r} - \dfrac{245.756}{r^2} + \dfrac{786.742}{r^3} - \dfrac{1000}{r^4} \right. \\ \quad - \dfrac{24.043}{r^5} + \dfrac{1000}{r^6} - \dfrac{47.967}{r^7} - \dfrac{1000}{r^8} \\ \left. \quad + \dfrac{64.527}{r^9} + \dfrac{1000}{r^{10}} - \dfrac{712.166}{r^{11}} + \dfrac{151.240}{r^{12}} \right) & r \le 2 \\ 0 & r > 2 \end{cases} . \tag{2.28}$$

This function is plotted in Fig. 2.1. The choice of $M = 12$ terms in our potential is a compromise between using many terms to strongly discriminate against competitors

and using few terms to avoid numerical instabilities. Potential (2.28) is an illustrative example from an infinite class of monotonic convex pair potentials that have the square lattice as their ground state.

To confirm that the ground state of potential (2.28) is indeed the square lattice configuration, we performed simulated annealing calculations. The result of these calculations is shown in Fig. 2.2. Examining many different simulated-annealing solutions, no other configuration is of lower energy than the square lattice. Of the four slowest simulated annealing calculations performed, three of them reach the target ground state. In the remaining case, the particles align in a square lattice, but do not align correctly within the periodic simulation box, resulting in a line defect where the lattice meets its periodic image. As with all other calculations (with more rapid annealing) that did not reach the perfect square-lattice configuration, the imperfect lattice total energy is higher than that for the perfect square lattice.

Simulated annealing calculations are also conducted on systems where the central cell shape is not kept constant. Even if the central cell is allowed to deform to any parallelogram of constant area, no configuration is found to be of lower energy than the square lattice. This strengthens our confidence that the square lattice is indeed the ground state for potential (2.28).

Discrimination against other crystals

Since we are using a pair potential with a short-ranged cutoff, the value of twice the energy per particle u only depends on the first few coordination shells. At unit

density, we can explicitly write u for the square, triangular and honeycomb crystals:

$$u_{SQ} = 4v\,(r=1) + 4v\,(r=1.414) = 4.4556, \tag{2.29}$$

$$u_{TR} = 6v\,(r=1.075) + 6v\,(r=1.861) = 4.7635, \tag{2.30}$$

$$u_{HC} = 3v\,(r=0.877) + 6v\,(r=1.520) + 3v\,(r=1.755) = 5.2363. \tag{2.31}$$

Furthermore, as can be seen in Fig. 2.1, potential (2.28) decreases very quickly, being equal to only 0.1139 at the square lattice second neighbor ($r = 1.414$). Therefore, examining only the nearest neighbors provides insight on why potential (2.28) succeeds at stabilizing the square-lattice configuration. While the potential is definitely higher for the square-lattice nearest neighbors [$v(r = 1) = 1$] than for the triangular-lattice nearest neighbors [$v(r = 1.075) = 0.7937$], its coordination number is smaller (four compared to six), and hence its total energy is the lowest. The same argument does not hold for the honeycomb crystal, since it has only three nearest neighbors. A much higher associated energy [$v(r = 0.877) = 1.6542$] prevents the honeycomb crystal from having a lower total energy than the square lattice.

While looking at the occupancy numbers of the successive coordination shells and the associated interactions of these shells aids our understanding of why potential (2.28) stabilizes the square lattice, it does not explain how such a monotonic convex potential can exist. However, the differences between the coordination functions of second order $\mathcal{Z}_2$ of the square lattice and the triangular and honeycomb crystals (Fig. 2.3) illustrate the necessary features for a monotonic convex potential to favor the square lattice over the triangular or honeycomb crystals. First, discriminating against the honeycomb crystal is easy, as its $\mathcal{Z}_2$ is larger than the square $\mathcal{Z}_2$ near $r = 1$. Therefore a potential with a very large second derivative for values of r close to 1 will strongly discriminate against the honeycomb crystal. Second, there is a range

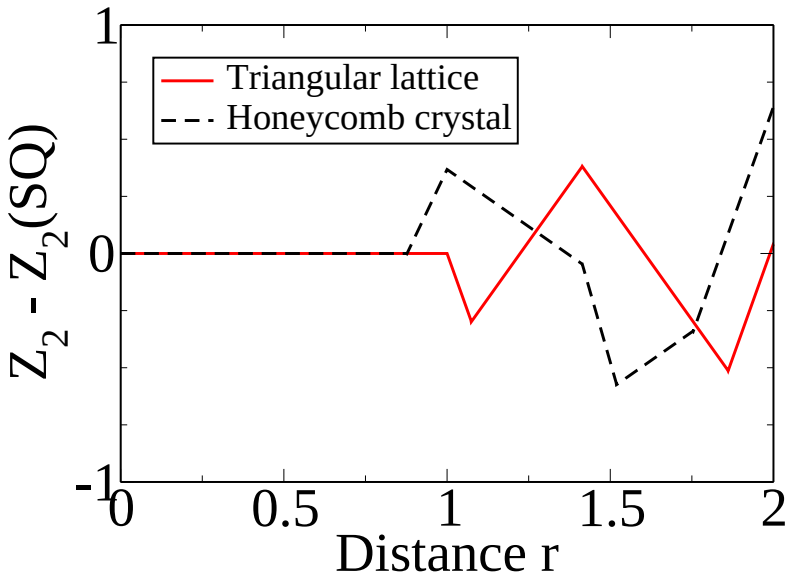

Figure 2.3: (Color online) Differences between the coordination functions of second order $\mathcal{Z}_2$ of the triangular lattice and the honeycomb crystal and the square lattice. All three lattices have a number density of unity.

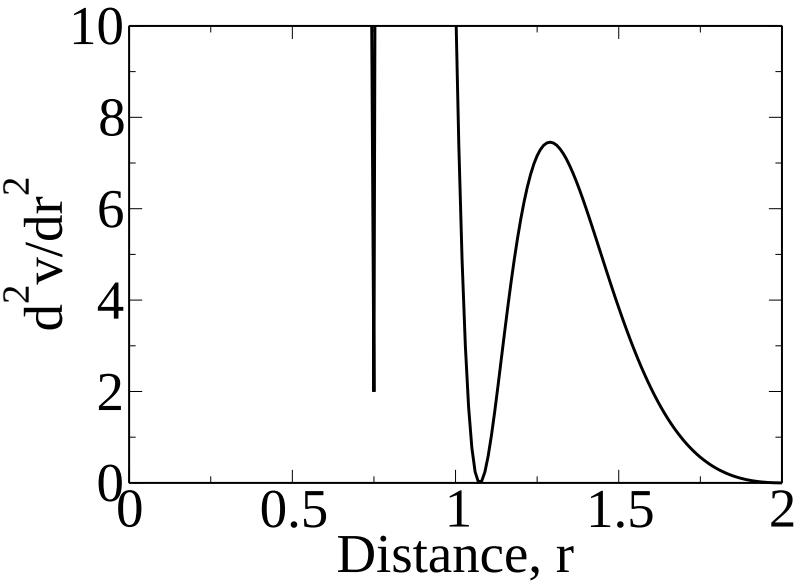

Figure 2.4: Second derivative of the pair potential d^2v/dr^2 from Eq. (2.28) versus the distance r.

of values of r where both the triangular and the honeycomb crystals' $\mathcal{Z}_2$'s are larger that of for the square lattice, specifically from $r \sim 1.2$ to $r \sim 1.4$. So a potential with a large second derivative in that range will favor the square lattice. Third, the triangular lattice $\mathcal{Z}_2$ is smaller around $r \sim 1.1$ and $r \sim 1.8$. Thus the second derivative must be close to zero at these points. Finally, the differences between the $\mathcal{Z}_2$'s become quite chaotic for larger values of r (not shown here), something which worsen if more competing configurations are considered. Consequently there is no advantage in increasing the cutoff R to larger values. As can be seen in Fig. 2.4, the pair potential function (2.28) possesses all of these features, which explains how it succeeds in having the square lattice as its ground state.

As a test to see if $\mathcal{Z}_2$ can be used to design a monotonic convex potential, we build a piecewise-polynomial potential using only information from the $\mathcal{Z}_2$ analysis,

$$v(r) = \begin{cases} 5r^2 - 10.45r + 5.61875 & r \leq 1, \\ -0.45r + 0.61875 & 1 < r \leq 1.15, \\ 0.5r^2 - 1.6r + 1.28 & 1.15 < r \leq 1.6, \\ 0 & 1.6 < r, \end{cases} \tag{2.32}$$

which has a second derivative of

$$\frac{d^2v}{dr^2} = \begin{cases} 10 & r \leq 1, \\ 0 & 1 < r \leq 1.15, \\ 1 & 1.15 < r \leq 1.6, \\ 0 & 1.6 < r. \end{cases} \tag{2.33}$$

Simulated annealing simulations confirm that this potential has the square lattice as its ground state, which proves that the precise form of the potential (2.28) is not necessary to have the square lattice as a ground state, however, potential (2.32) is flawed, as its second derivative is not continuous at the first neighbor distance ($r = 1$),

preventing its phonon spectrum from being calculated. Furthermore, since potential (2.32)'s second derivative is exactly zero for r's slightly larger than 1, at lower densities the square lattice will not be the ground-state; it is replaced by a rectangular lattice. Nevertheless, potential (2.32) proves that it is possible to construct a potential that stabilizes the square lattice using only information from the generalized coordination functions. Furthermore, since such requirements are relatively nonrestrictive, there is still a large class of potentials that stabilize the square lattice, one of which is potential function (2.32).

Stability

There are three basic criteria which impact whether the configurations created using the proposed potential are stable square lattices: their response to changes in the number density, their oscillation (phonon) stability and their response to slight modifications in the potential. This last criterion is not formally studied here, due to the difficulty of modifying the value of a polynomial only over a short range. However, as shown in Sec. 2.3.1, as long as the modified potential second derivative displays the features described therein, the modified potential will keep its square-lattice ground state.

Figure 2.5 shows the squared frequency of the different phonon modes for the square lattice as a function of their wave vectors. For any wave vector, if one of the modes has a negative squared frequency, then the resulting imaginary frequency mode is unstable, a sign that the square lattice is not a local minimum in the energy landscape. Since none of the mode squared frequency are negative for any wave vector, the square lattice is indeed at least a local minimum for potential function (2.28). All branches except one between the Γ and X points show a high deformation energy. In addition, the low energy $\Gamma - X$ branch contains shear deformations modes,

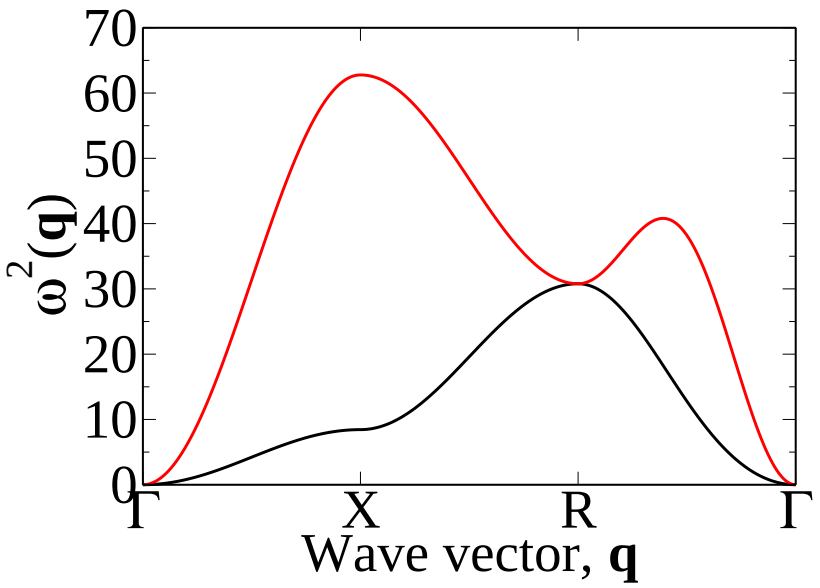

Figure 2.5: (Color online) Phonon spectrum for the potential function (2.28) on a square lattice with unit nearest neighbor distance ($\rho = 1$). Only a representative subset the wave vectors is presented here, but all of wave vectors have been tested to confirm that no mode is unstable.

which are less energetic than compression deformations for isotropic pair potentials, since they only slightly modify interparticle distances.

Figure 2.6 presents the lattice sums of the triangular, square and honeycomb crystals for different number densities. The lattice sum for a given particle configuration C, in which each particle is equivalent to all others, is defined as the sum of the potential interaction energies between one of the particles p and all the others. Twice the energy per particle, u, is a generalization of the lattice sums that is well-defined for any configuration, including those for which particles are not equivalent.

At $\rho^{-1} = 1$, the value of u for the square, triangular and honeycomb crystal configurations is 4.4556, 4.7635 and 5.2363, respectively. It is worthwhile to note that the honeycomb crystal u never comes close to the square lattice u, and thus can be discarded from the analysis. Over the $\rho^{-1} \in [0.9, 1.2]$ range, the square lattice has a lower energy than the triangular lattice. However, outside the $\rho^{-1} \in [0.91, 1.04]$ range, simulated annealing calculations produce configurations with lower

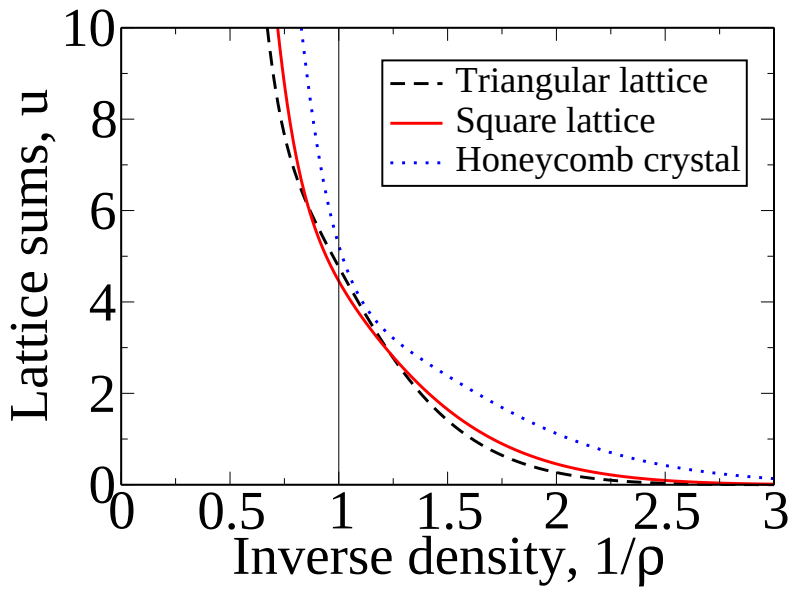

Figure 2.6: (Color online) Lattice sums in term of the inverse number density for the potential function (2.28). The black vertical line shows the number density ($\rho^{-1} = 1$) at which the optimization is conducted.

energy than the square lattice. At $\rho^{-1} < 0.91$, a deformed triangular lattice becomes the ground state; while at $\rho^{-1} > 1.04$, a rectangular lattice is the ground state. In the case of the rectangular lattice, its nearest neighbor distance stays close to $r = 1$. This is due to the near linear dependence of the potential for values of r slightly greater than one (as the second derivative nearly vanishes). For such potentials, u decreases linearly with the sum of the distances of the four nearest neighbors, which is larger for a rectangular lattice than for a square lattice with an equal number density. Furthermore, rectangular lattices have farther third nearest neighbors than the corresponding second nearest neighbors of the square lattice.

While the positivity of the phonon spectrum ensures that the square lattice is stable under local deformations, it does not lead to any insight as to how potential (2.28) succeeds in stabilizing it. Alternatively, we can look at how u is affected when the square lattice is sheared, which is equivalent to the phonon modes near the Γ-point. The lattices obtained by the two independent shear modes are the rectangular lattice, with basis vectors $(1+\varepsilon, 0)$ and $(0, (1+\varepsilon)^{-1})$, and the rhomboidal lattice,

with basis vectors $(1, \varepsilon)$ and $(0, 1)$. For the rectangular lattice,

$$\begin{aligned} u_{rect}(\varepsilon) &= u_{square} + \left[4v'(1) + 8\sqrt{2}v'(\sqrt{2}) + 4v''(1)\right]\varepsilon^2 + O(\varepsilon^3), \\ &= u_{square} + \left[4(-2.943) + 8\sqrt{2}(-0.917) + 4(10.640)\right]\varepsilon^2 + O(\varepsilon^3), \\ &= u_{square} + 20.407\varepsilon^2 + O(\varepsilon^3), \end{aligned} \tag{2.34}$$

and for the rhomboidal lattice,

$$\begin{aligned} u_{rect}(\varepsilon) &= u_{square} + \left[2v'(1) + \sqrt{2}v'(\sqrt{2}) + 2v''(\sqrt{2})\right]\varepsilon^2 + O(\varepsilon^3), \\ &= u_{square} + \left[2(-2.943) + \sqrt{2}(-0.917) + 2(5.702)\right]\varepsilon^2 + O(\varepsilon^3), \\ &= u_{square} + 4.220\varepsilon^2 + O(\varepsilon^3). \end{aligned} \tag{2.35}$$

We now clearly see that the monotonicity condition, which forces the first derivative to always be negative, requires the second derivative to be large at both the first and second neighbors in order to achieve stability, since each appears in only one of the shear modes. An additional benefit of this analysis is that it explains how the square lattice is stable for a non-zero number density range; since both the first and second derivatives of potential (2.28) are continuous, the nearest-neighbor distance has to be modified by a positive amount before the $O(\varepsilon^2)$ terms in the shearing mode energies become negative (note: due to its symmetry, the $O(\varepsilon)$ term is always zero for the square lattice).

Point defects

While looking for the ground state of the potential function (2.28), we do not always obtain the actual ground state shown in Fig. 2.2. When an insufficiently slow annealing is applied to the system, the end result often contains defects. Among these are polycrystalline configurations, where line defects show up at the boundaries between

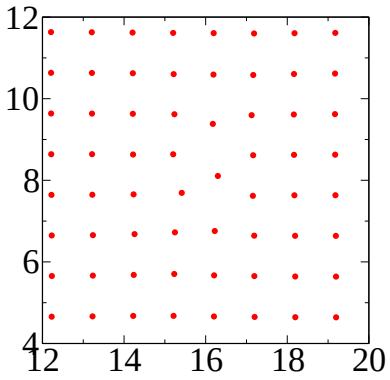

Figure 2.7: (Color online) Sample monovacancy defect on a 399-particle system (only part of which is shown) with $\rho = 1$ for the potential function (2.28).

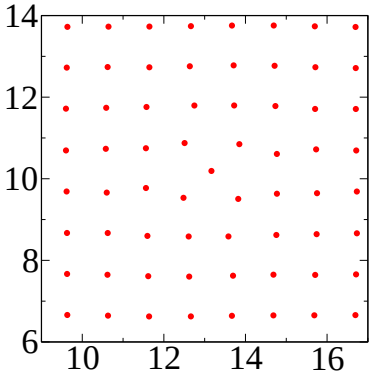

Figure 2.8: (Color online) Sample interstitial defect on a 401-particle system (only part of which is shown) with $\rho = 1$ for the potential function (2.28).

grains. However, some localized defects also arise. Such defects are caused by the presence (or absence) of an extra particle in the lattice.

Simply removing (or adding) a particle in the square lattice ground state does not reveal the actual behavior of such point defects. The presence of a defect locally deforms the lattice, which is necessary to minimize its energy. Starting with a square lattice to which a particle is either added or removed (while changing the lattice spacing to keep the overall number density constant at $\rho = 1$), the configuration is then relaxed using simulated annealing. The simulated annealing temperature is chosen to be low enough that the lattice is not destroyed by melting, and high enough that the location of the defect can move through the lattice.

Figure 2.7 shows a mechanically stable structure for a monovacancy point defect, with a total energy difference of 0.62425 between the configuration with a single defect and the perfect square lattice. Figure 2.8 presents the interstitial defect, with an energy difference of 0.39646. These results are computed using modified 20×20 lattices, with 399 and 401 particles, respectively, but larger systems give essentially the same numbers. Starting with multiple defects also gives consistent results, although vacancies tend to attract each other. These single-defect numbers need to be compared with twice the energy per particle of the square lattice: $u = 4.45561$. It should be noted that there is no particular significance to which defect is the most energetic, since calculations with a similar potential (but with a larger cut-off R) find the interstitial defect to be the more energetic of the two.

An unexpected result is the complete absence of symmetry of the vacancy point defect configuration in Fig. 2.7. The results of 100 slow annealing simulations confirm that the configuration shown in Fig. 2.7 is indeed the stable configuration containing a monovacancy. Out of these, the system converges to a configuration of the type shown in Fig. 2.7, 69 times. In all of the 31 other cases, the system reaches a single type of alternative defect configuration. That other configuration has a defect energy of 0.63223, only 0.00798 higher than the lowest one. It is also more symmetrical, since it possesses a single axis of symmetry. The failure to find any other configuration than these two, especially one with lower energy, is compelling evidence that the configuration shown in Fig. 2.7 is indeed the lowest-energy-vacancy defect for this potential, even if it is asymmetric.

Dropping the convexity condition

It is possible to achieve the square-lattice ground state without the convexity constraint, keeping only the monotonicity requirement. Figure 2.9 depicts such an optimized potential. Since the potential presented in Fig. 2.9 has a short-range cutoff

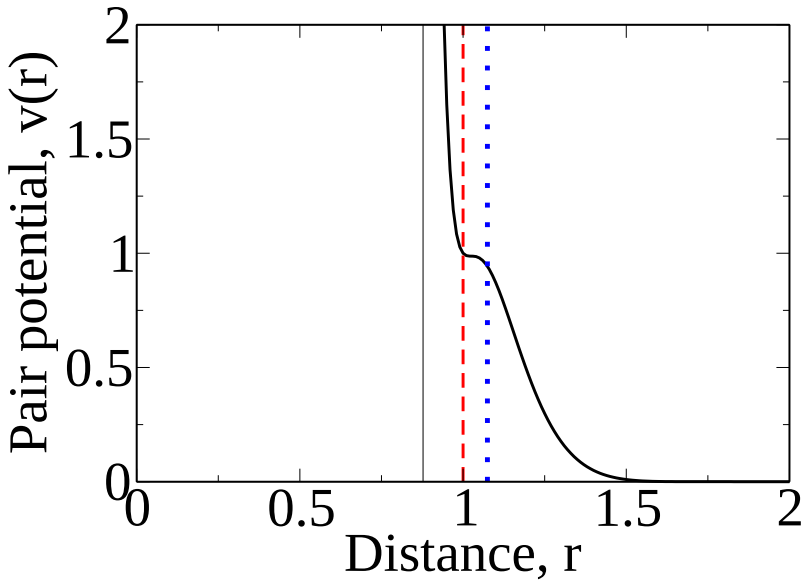

Figure 2.9: (Color online) Optimized monotonic non-convex pair potential, targeting the square lattice at unit number density. The three vertical lines represent the nearest-neighbor distances for the honeycomb crystal (black solid), the square lattice (red dashed) and the triangular lattice (blue dotted), at the same number density. The value of $v(r)$ at these distances is 14.4371, 1 and 0.9428, respectively.

radial distance $r = R = 2$, u only depends on the first few coordination shells. Similar to the analysis in Sec. 2.3.1, we can explicitly write u for the square, triangular and honeycomb crystals at unit density as:

$$u_{SQ} = 4v\,(r = 1) + 4v\,(r = 1.414) = 4.1611, \tag{2.36}$$

$$u_{TR} = 6v\,(r = 1.075) + 6v\,(r = 1.861) = 5.6571, \tag{2.37}$$

$$u_{HC} = 3v\,(r = 0.877) + 6v\,(r = 1.520) + 3v\,(r = 1.755) = 43.3517. \tag{2.38}$$

Again, since the Fig. 2.9 potential decreases steeply, almost all of the energy contributions stem from the nearest neighbors. For instance, the value of the potential at the square lattice second nearest neighbors is only $v(r = 1.414) = 0.0403$, which is much lower than its value at the nearest neighbors $v(r = 1) = 1$. While $v(r)$ is very low close to the second square neighbor, it is mostly constant between the square and

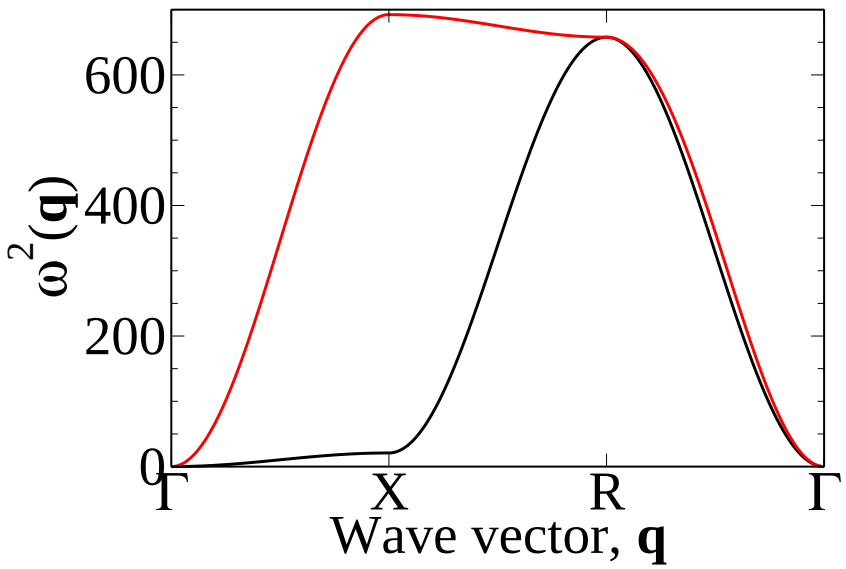

Figure 2.10: (Color online) Phonon spectrum for the potential shown in Fig. 2.9 on a square lattice with unit nearest neighbor distance ($\rho = 1$). Only a representative subset of wave vectors is presented here, but all of wave vectors have been tested to confirm that no mode is unstable.

triangular lattices nearest neighbors, only going down to $v(r = 1.075) = 0.9428$ at the triangular lattice nearest neighbors. This fact, combined with the higher nearest-neighbor coordination number of the triangular lattice (six versus the four for the square lattice), explains why the total energy of the triangular lattice is significantly higher than the total energy of the square lattice. In summary, removing the convexity requirement increases the set of possible potential functions that stabilize the square lattice. This is additional evidence that there exists a large family of monotonic potentials that stabilize the square lattice.

There are two important weaknesses of the method used to obtain the optimized potential. While intuition predicts that removing restrictions should result in a "better" potential, the phonon spectrum (Fig. 2.10) and the lattice sums (Fig. 2.11) indicate a ground state that is less stable than the monotonic convex potential (compare Figs. 2.5 and 2.6). This behavior occurs because for the Fig. 2.9 potential, only the triangular lattice is considered a competitor, and the optimizer simply tries to maximize the energy difference between both lattices at a single number density. This

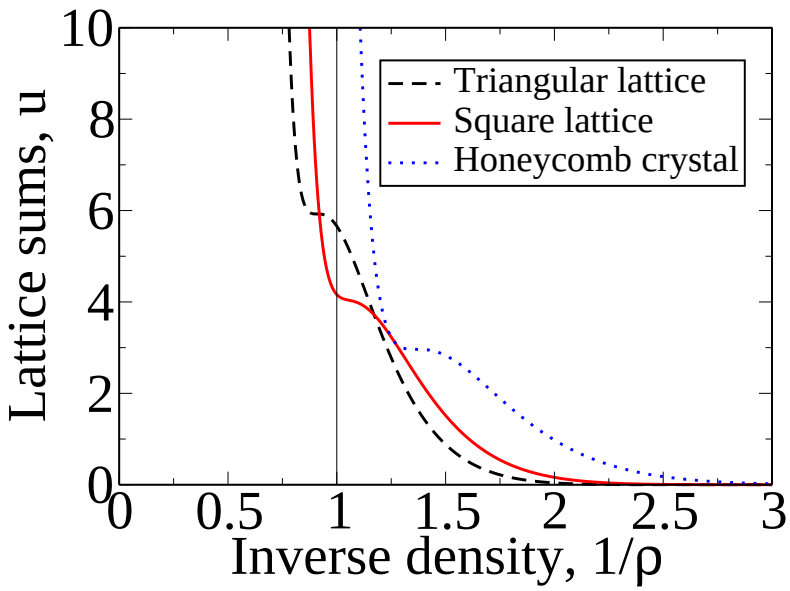

Figure 2.11: (Color online) Lattice sums in term of the inverse number density for the potential shown in Fig. 2.9. The vertical black line shows the number density ($\rho^{-1} = 1$) at which the optimization is conducted.

is done at the expense of the stability of the lattice, represented by number density variations (lattice sums) and local fluctuations (the phonon spectrum).

2.3.2 Honeycomb crystal

As with the square lattice, we also use our method to obtain a pair potential for the honeycomb crystal with a nearest neighbor distance of unity ($\rho = 4/3\sqrt{3}$). The optimization is restricted to monotonic convex potentials with a cutoff at $r = 3$. While intuition leads one to believe that the presence of the square lattice in the competitor set $\mathbf{C}$ is required to find an optimized potential for which the ground state is the honeycomb lattice, this is not the case, since a set $\mathbf{C}$ consisting only of the triangular lattice is sufficient to obtain a potential with the desired ground state.

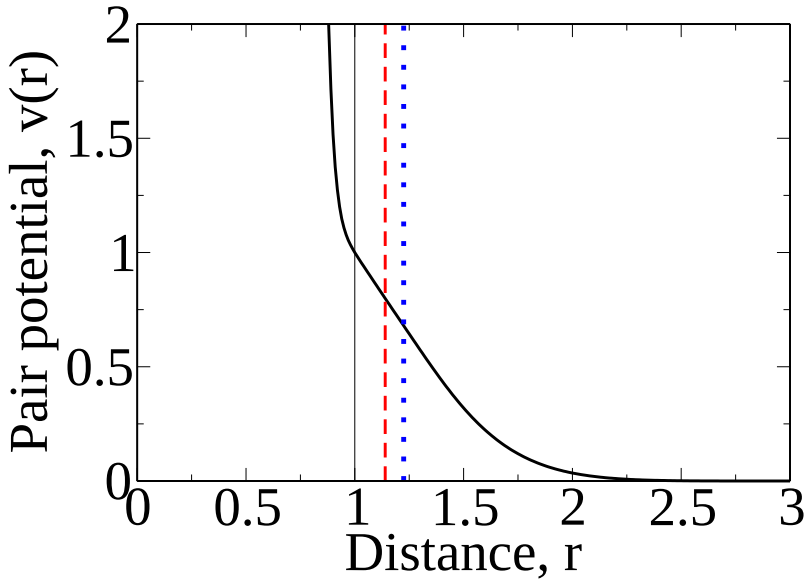

Figure 2.12: (Color online) Optimized convex pair potential function (2.39), targeting the honeycomb crystal at $\rho = 4/3\sqrt{3}$. The three vertical lines represent the nearest-neighbor distances for the honeycomb crystal (black solid), the square lattice (red dashed) and the triangular lattice (blue dotted), at $\rho = 4/3\sqrt{3}$. The value of $v(r)$ at these distances is 1, 0.7990 and 0.6795, respectively.

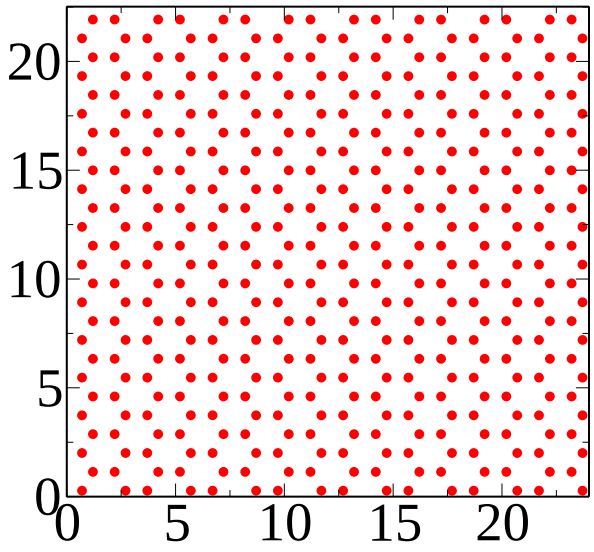

Figure 2.13: (Color online) The ground state of the potential function (2.39) with 416 particles in a $24\times13\sqrt{3}$ box with periodic boundary conditions, obtained by slowly annealing the system from a fluid.

The resulting optimized potential is

$$v(r) = \begin{cases} \left(\dfrac{3.767}{r} - \dfrac{48.246}{r^2} + \dfrac{230.514}{r^3} - \dfrac{451.639}{r^4}\right. \\ \quad + \dfrac{56.427}{r^5} + \dfrac{1000}{r^6} - \dfrac{868.468}{r^7} - \dfrac{776.495}{r^8} \\ \left. \quad + \dfrac{1000}{r^9} + \dfrac{521.638}{r^{10}} - \dfrac{1000}{r^{11}} + \dfrac{333.502}{r^{12}}\right) & r \leq 3, \\ 0 & r > 3. \end{cases} \tag{2.39}$$

This function is plotted in Fig. 2.12. Figure 2.13 shows the ground-state configuration of potential (2.39), obtained using simulated annealing down to zero temperature, starting with a random arrangement of particles generated by a Poisson point process. Whether the ground state is reached for a given simulation depends greatly on the orientation the crystal takes during cooling. Due to the boundary conditions, only two orientations allow the honeycomb crystal to be formed without defects, which makes reaching the ground state difficult. However, when the crystal is not oriented correctly, the resulting configuration is still visibly a honeycomb crystal, albeit with minor defects and deformation, as well as a higher energy than the perfect honeycomb crystal configuration. During the ground state simulations, no other configuration is found to have a lower energy than the honeycomb crystal. Out of the four slowest simulated-annealing calculations executed with this potential, two of them reach the perfect honeycomb crystal. The two others do not align correctly with the boundary conditions and thus converge to honeycomb crystals with a slight shear and some localized defects.

As with the square-lattice potential, we conduct simulated-annealing calculations with variable periodic-box dimensions. For boxes of constant area, all converged configurations have higher energy than the honeycomb crystal, reinforcing our conclusion that potential (2.39) has the honeycomb-crystal configuration as its ground state.

Discrimination against other crystals

Since we are using a pair potential with a short-ranged cutoff, the value of twice the energy per particle u only depends on the first few coordination shells. At $\rho = 4/3\sqrt{3}$, we can explicitly write u for the honeycomb, triangular and square crystals:

$$\begin{aligned} u_{HC} &= 3v\,(r=1) + 6v\,(r=1.732) + \\ &\quad 3v\,(r=2) + 6v\,(r=2.646) = 3.8812, \end{aligned} \tag{2.40}$$

$$\begin{aligned} u_{TR} &= 6v\,(r=1.225) + 6v\,(r=2.121) + \\ &\quad 12v\,(r=2.449) = 4.1919, \end{aligned} \tag{2.41}$$

$$\begin{aligned} u_{SQ} &= 4v\,(r=1.140) + 4v\,(r=1.612) + \\ &\quad 4v\,(r=2.280) + 8v\,(r=2.649) = 4.0755. \end{aligned} \tag{2.42}$$

That potential (2.39) succeeds in having a lower u for the honeycomb crystal than the triangular lattice is readily explained by the observation that the triangular-lattice coordination number is twice that of the honeycomb crystal. The triangular-lattice nearest neighbors have an interaction energy of $v(r = 1.225) = 0.6795$, which is much higher than half of the honeycomb-crystal nearest-neighbors interaction $[v(r = 1) = 1]$. The square lattice also has a larger coordination number than the honeycomb crystal, with a value equivalent to four-thirds of the latter. The square-lattice nearest neighbors have an interaction energy slightly larger than three-fourths of the honeycomb-crystal nearest neighbors $[v(r = 1.140) = 0.7990$ versus $v(r = 1) = 1]$. This energy difference is further supplemented by the second-nearest neighbors of the square lattice, which are closer than those of the honeycomb crystal. Even if they are less numerous (four instead of six), their interaction energy is much larger $[v(r = 1.612) = 0.2123$ versus $v(r = 1.732) = 0.1292]$.

As with the square lattice, the coordination function of second order $\mathcal{Z}_2$ can be used to determine which features are required in a potential's second derivative if the

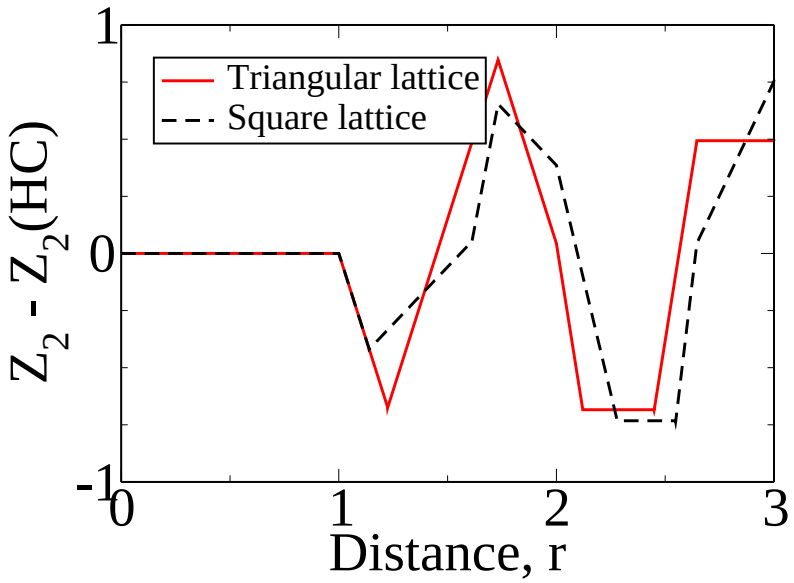

Figure 2.14: (Color online) Differences between the coordination functions of second order $\mathcal{Z}_2$ of the triangular and square lattices and the honeycomb crystal. All three crystal have a number density of $4/3\sqrt{3}$.

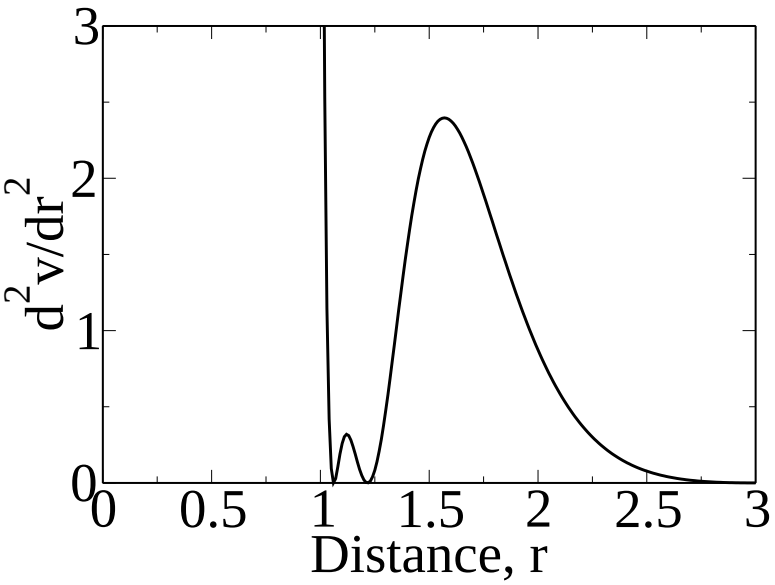

Figure 2.15: Second derivative of the pair potential d^2v/dr^2 from Eq. (2.39) versus the distance r.

potential is to have the honeycomb crystal as its ground state. Figure 2.14 shows the differences in $\mathcal{Z}_2$ between the honeycomb crystal and its two main competitors, the triangular and the square lattices. In this figure, we see that after the quasi-hard-core repulsion region ($r < 1$), the second derivative must be close to zero up to $r \sim 1.5$, before becoming large up to $r \sim 2$, in order for the triangular and square lattices to be energetically unfavorable relative to the honeycomb crystal. This behavior can be observed in the second derivative of the proposed potential (Fig. 2.15). The reason the second derivative has two distinct r values at which it goes down to zero is a consequence of the potential-function form restrictions, which does not allow a wide well without adding another minimum.

As with the square lattice, we use the information extracted from $\mathcal{Z}_2$ to build a piecewise-polynomial potential for which the honeycomb crystal is the ground state,

$$v(r) = \begin{cases} 5r^2 - 10.5r + 5.875 & r \leq 1, \\ -0.5r + 0.875 & 1 < r \leq 1.5, \\ 0.5r^2 - 2r + 2 & 1.5 < r \leq 2, \\ 0 & 2 < r, \end{cases} \tag{2.43}$$

with a second derivative

$$\frac{d^2v}{dr^2} = \begin{cases} 10 & r \leq 1, \\ 0 & 1 < r \leq 1.5, \\ 1 & 1.5 < r \leq 2, \\ 0 & 2 < r. \end{cases} \tag{2.44}$$

Simulated annealing calculations show that the ground state of potential (2.43) is indeed the honeycomb crystal. However, as is the case for the square lattice equivalent potential [cf. Eq. (2.32)], some caveats apply; mainly the discontinuity of the second

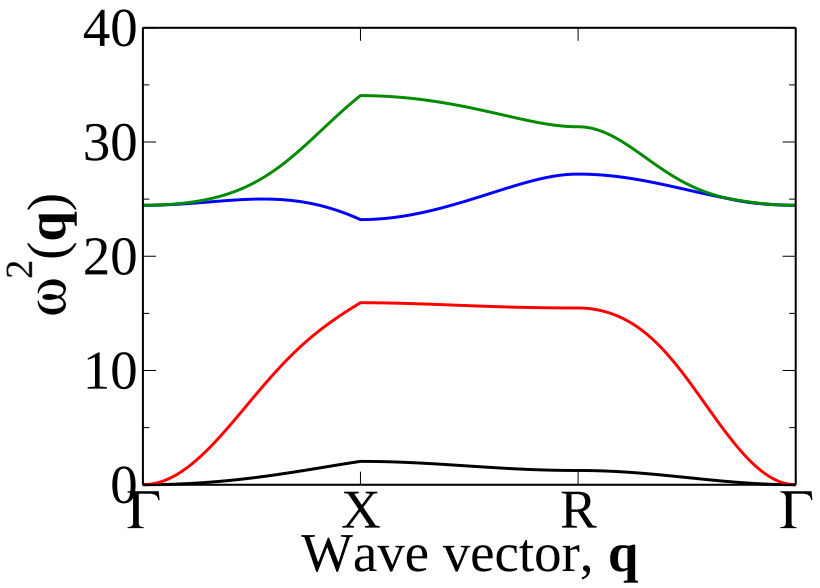

Figure 2.16: (Color online) Phonon spectrum for potential (2.39) on a honeycomb crystal with unit nearest neighbor distance ($\rho = 4/3\sqrt{3}$). Only a representative subset of wave vectors is presented here, but all wave vectors have been tested to confirm that no mode is unstable.

derivative at $r = 1$ prevents the verification of the honeycomb crystal stability by its phonon spectrum.

Stability

As for the case of the square lattice, three properties must be checked to determine whether the proposed potential forms a stable honeycomb crystal: is the honeycomb crystal the ground state over a non-vanishing number density range, are the phonon modes stable, and what are the effects of perturbing the potential form? Again, only the first two of these are appraised in this chapter.

Figure 2.16 shows the squared frequency of the different phonon modes as a function of their wave vector. An exhaustive search confirms that there is no mode for which the squared frequency is negative, indicating that the honeycomb crystal is at least a local minimum in the energy landscape for the pair potential function (2.39).

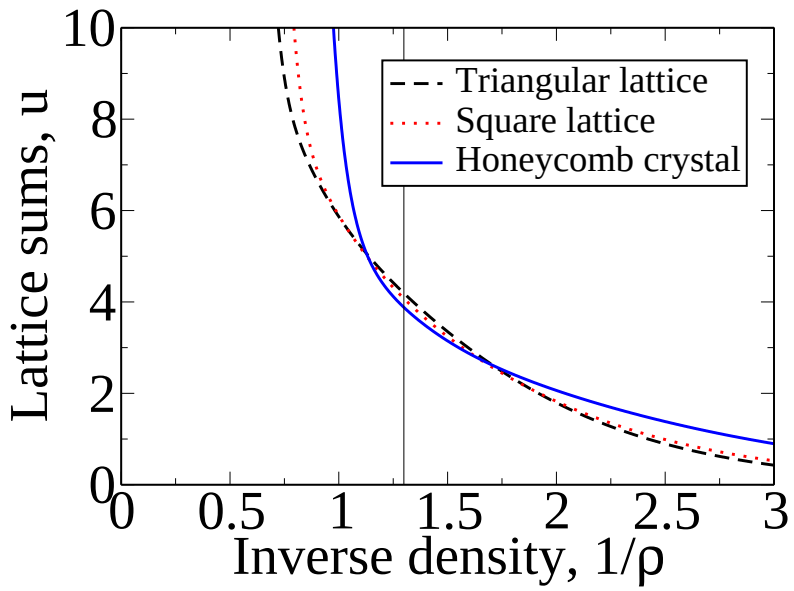

Figure 2.17: (Color online) Lattice sums in term of the inverse number density for potential (2.39). The vertical black line shows the number density ($\rho^{-1} = 3\sqrt{3}/4$) at which the optimization is conducted.

Figure 2.17 compares the lattice sums u at different number densities for the triangular, square, and honeycomb crystals. At $\rho^{-1} = 3\sqrt{3}/4$, the u for the honeycomb, triangular and square crystals are equal to 3.8812, 4.1919, and 4.0755, respectively. For $\rho^{-1} \in [1.15, 1.6]$, the honeycomb crystal has a lower energy than both the square and the triangular lattices. This range is further refined to $\rho^{-1} \in [1.2, 1.4]$, where simulated annealing calculations produce configurations recognizable as the honeycomb crystal as the ground state. However, many of these configurations are not actually the honeycomb crystal, but rather deformed versions of it. By calculating the phonon spectrum of the honeycomb crystal over this range, we determine that the honeycomb crystal is only stable over $\rho^{-1} \in [1.25, 1.35]$. At larger densities ($\rho^{-1} < 1.2$), the potential favors a configuration consisting of pentagonal rings (compared to the hexagonal rings of the honeycomb crystal), while at lower densities ($\rho^{-1} > 1.4$), the potential favors particles in evenly spaced chains, effectively reducing the number of nearest neighbors to only two.

Similar to the square lattice, we can explore the effect of shearing on the honeycomb crystal to understand how potential (2.39) stabilizes it against local deformations. Unlike the square lattice, which has two independent shear modes, both of the honeycomb crystal modes have equal energy up to a constant, so we only need to verify one of them. Looking at the crystal obtained by stretching the honeycomb crystal by $(1+\varepsilon)$ in the x-direction and $(1+\varepsilon)^{-1}$ in the y-direction, we obtain

$$\begin{aligned} u_{stretched}(\varepsilon) &= u_{hc} + \left[\begin{array}{l} \frac{9}{2}v'(1) + 9\sqrt{3}v'(\sqrt{3}) + 9v'(2) + 9\sqrt{7}v'(\sqrt{7}) \\ +\frac{3}{2}v''(1) + 9v''(\sqrt{3}) + 6v''(2) + 21v''(\sqrt{3}) \end{array} \right] \varepsilon^2 + O(\varepsilon^3), \\ &= u_{hc} + \left[\begin{array}{l} \frac{9}{2}(-1.561) + 9\sqrt{3}(-0.564) + 9(-0.189) + 9\sqrt{7}(-0.003) \\ +\frac{3}{2}(8.882) + 9(1.971) + 6(0.873) + 21(0.0280) \end{array} \right] \varepsilon^2 + O(\varepsilon^3), \\ &= u_{hc} + 19.303\varepsilon^2 + O(\varepsilon^3). \end{aligned} \tag{2.45}$$

Again, as in the square lattice case, large second-derivative values are necessary to stabilize the honeycomb crystal with a monotonic potential.

Point defects

As for the potential with a square lattice ground state, it is also relevant to study the behavior of point defects for the potential with a honeycomb ground state. Figure 2.18 shows the monovacancy defect, which has an energy of 0.28414, while Fig. 2.19 shows the interstitial defect, which has an energy of 0.44761. Similar to the square lattice, there is no fundamental reason for why the vacancy is less energetic than the interstitial defect.

2.4 Conclusions and discussion

The possibility of designing pair potentials that result in the self-assembly of unusual targeted many-particle configurations is not surprising if one allows for one or a few

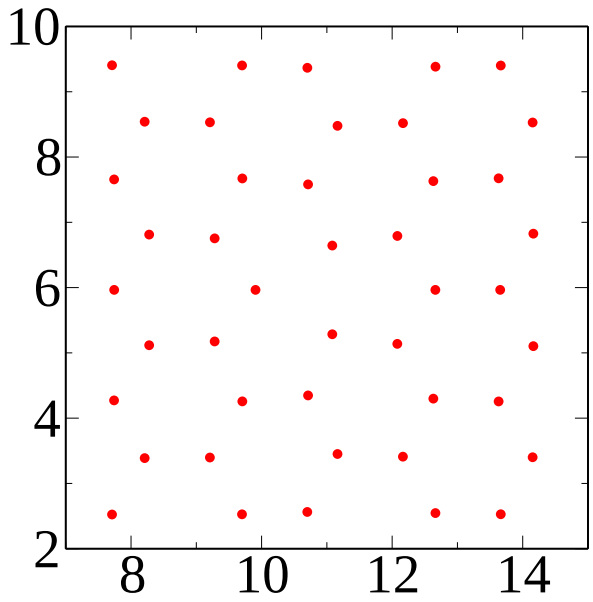

Figure 2.18: (Color online) Sample monovacancy defect on a 415 particles system (only part of which is shown) with $\rho = 4/3\sqrt{3}$ for the potential function (2.39).

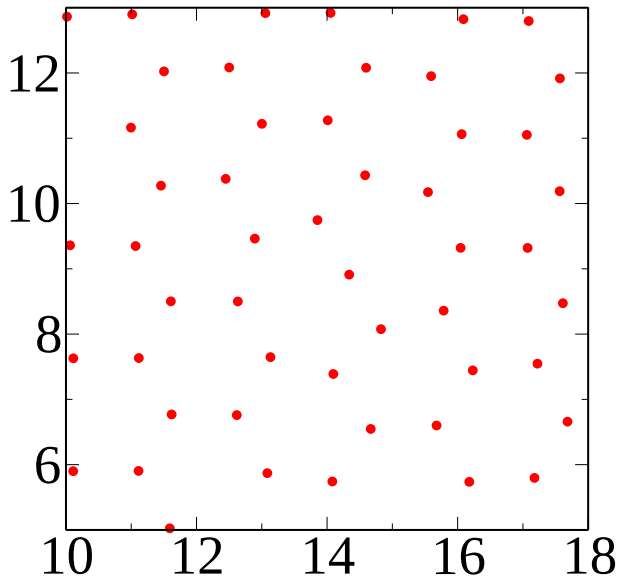

Figure 2.19: (Color online) Sample interstitial defect on a 417 particles system (only part of which is shown) with $\rho = 4/3\sqrt{3}$ for the potential function (2.39).

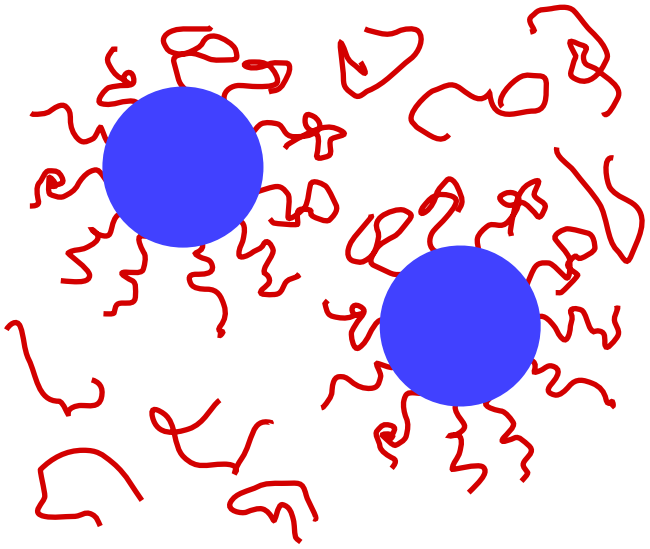

Figure 2.20: Sketch of possible colloids with a pair potential similar to those from Eqs. (2.28) and (2.39). The hard-core colloids are covered with attached repelling polymers, whose average extension is controlled by the dissolved polymers chains.

potential wells at strategic locations [10, 12]. Whether it is possible to find potentials that stabilize novel classical ground states in Euclidean space without any wells is not at all obvious. In this chapter, we have shown that potentials without wells, namely, monotonic convex repulsive pair interactions, can produce low-coordinated ground states in $\mathbb{R}^2$ such as the square lattice and the honeycomb crystal. Indeed, our work demonstrates that there exists a large family of monotonic potentials that stabilize the square and honeycomb crystals.

Lindenblatt *et al.* [18] have fabricated so-called "hairy colloids" (see Fig. 2.20). These colloids are formed by grafting polymer chains onto the surface of nanoscopic microgel spheres in a matrix of polymer chains. The swelling of the grafted chains can be controlled by varying the molecular weight of the matrix chains, going from "wet brushes," with a lot of swelling for short matrix chains, to "dry brushes," with little swelling for long matrix chains. The coronas of the grafted polymers avoid each other, giving rise to a short-range repulsive effective pair potential between the resulting colloids. Together with a hard-core repulsion when the microgel spheres

touch, these colloid interactions offer promise of being similar to Eqs. (2.28) and (2.39), although experimental realization remains an unfulfilled endeavor.

However, there is no evidence that the pair potentials of these "hairy colloids" have a strong dip in their second derivative, a feature is crucial for the self-assembly of both the square lattice and the honeycomb crystal. Instead of trying to synthesize colloids with potentials identical to those presented in this chapter, another approach would be to determine what monotonic repulsive potentials are possible using grafted polymers of variable length. If the resulting potentials can be written in the form of $v(r) = \int_s dsc(s)f(r,s)$, then the generalized coordination function formalism from Sec. 2.2.3 could be used to explore which length distribution of grafted polymers should be used for the colloids to self-assemble in targeted configurations.

We reiterate that we have shown there are monotonic convex potentials with low-coordinated ground states in two-dimensional Euclidean spaces. While it has been suggested that such potentials exist in three dimensions [3, 9, 24]. phonon spectra were not computed in these studies. An interesting area for further research would be to verify whether the generalized-coordination-function techniques introduced in this chapter can be extended to optimize monotonic convex potentials to stabilize low-coordianted three-dimensional crystal ground states, such as the simple cubic and diamond crystals. Another topic that warrants further research is whether purely repulsive interactions that can be achieved in the laboratory to yield low-coordinated ground-state configurations.

Bibliography

[1] G. M. Whitesides, J. P. Mathias, and C. T. Seto, *Molecular self-assembly and nanochemistry: a chemical strategy for the synthesis of nanostructures*, Science **254**, 1312 (1991).

[2] S. A. Jenekhe and X. L. Chen, *Self-Assembly of Ordered Microporous Materials from Rod-Coil Block Copolymers*, Science **283**, 372 (1999).

[3] M. Watzlawek, C. N. Likos, and H. Löwen, *Phase Diagram of Star Polymer Solutions*, Phys. Rev. Lett. **82**, 5289 (1999).

[4] D. Gottwald, C. N. Likos, G. Kahl, and H. Löwen, *Phase Behavior of Ionic Microgels*, Phys. Rev. Lett. **92** 68301 (2004).

[5] A. M. Jackson, J. W. Myerson, and F. Stellacci, *Spontaneous assembly of subnanometre-ordered domains in the ligand shell of monolayer-protected nanoparticles*, Nat. Mater. **3**, 330 (2004).

[6] M.-P. Valignat, O. Theodoly, J. C. Crocker, W. B. Russel, and P. M. Chaikin, *Reversible self-assembly and directed assembly of DNA-linked micrometer-sized colloids*, Proc. Natl. Acad. Sci. U.S.A. **102**, 4225 (2005).

[7] A.-P. Hynninen, C. G. Christova, R. Van Roij, A. Van Blaaderen, and M. Dijkstra, *Prediction and Observation of Crystal Structures of Oppositely Charged Colloids*, Phys. Rev. Lett. **96**, 138308 (2006).

[8] C. N. Likos, B. M. Mladek, A. J. Moreno, D. Gottwald, and G. Kahl, *Cluster-forming systems of ultrasoft repulsive particles: statics and dynamics*, Comp. Phys. Comm. **179**, 71 (2008).

[9] S. Prestipino, F. Saija, and G. Malescio, *The zero-temperature phase diagram of soft-repulsive particle fluids*, Soft Matter **5**, 2795 (2009).

[10] M. C. Rechtsman, F. H. Stillinger, and S. Torquato, *Designed interaction potentials via inverse methods for self-assembly*, Phys. Rev. E **73**, 011406 (2006).

[11] M. C. Rechtsman, F. H. Stillinger, and S. Torquato, *Self-assembly of the simple cubic lattice with an isotropic potential*, Phys. Rev. E **74**, 021404 (2006).

[12] M. C. Rechtsman, F. H. Stillinger, and S. Torquato, *Synthetic diamond and wurtzite structures self-assemble with isotropic pair interactions*, Phys. Rev. E **75**, 031403 (2007).

[13] M. C. Rechtsman, F. H. Stillinger, and S. Torquato, *Negative Thermal Expansion in Single-Component Systems with Isotropic Interactions*, J. Phys. Chem. A **111**, 12816 (2007).

[14] M. C. Rechtsman, F. H. Stillinger, and S. Torquato, *Negative Poisson's Ratio Materials via Isotropic Interactions*, Phys. Rev. Lett. **101**, 085501 (2008).

[15] O. U. Uche, S. Torquato and F. H. Stillinger, *Collective coordinate control of density distributions*, Phys. Rev. E **74**, 031104 (2006).

[16] R. D. Batten, F. H. Stillinger, and S. Torquato, *Classical disordered ground states: Super-ideal gases and stealth and equi-luminous materials*, J. Appl. Phys. **104**, 033504 (2008).

[17] M. Florescu, S. Torquato and P. J. Steinhardt, *Designer disordered materials with large, complete photonic band gaps*, Proc. Nat. Acad. Sci. U.S.A **106**, 20658 (2009).

[18] G. Lindenblatt, W. Schärtl, T. Pakula, and M. Schmidt, *Structure and Dynamics of Hairy Spherical Colloids in a Matrix of Nonentangled Linear Chains*, Macromolecules **34**, 1730 (2001).

[19] V. N. Manoharan, M. T. Elsesser and D. J. Pine, *Dense Packing and Symmetry in Small Clusters of Microspheres*, Science **301**, 483 (2003).

[20] S. Torquato, *Inverse optimization techniques for targeted self-assembly* , Soft Matter **5**, 1157 (2009).

[21] H. Cohn and A. Kumar, *Algorithmic design of self-assembling structures*, Proc. Natl. Acad. Sci. USA **106**, 9570 (2009).

[22] É. Marcotte, F. H. Stillinger and S. Torquato, *Optimized monotonic convex pair potentials stabilize low-coordinated crystals*, Soft Matter **7**, 2332 (2011).

[23] Of course, rigorously proving that a given configuration is a true ground state is highly nontrivial, so we must accept the results from carefully designed numerical methods.

[24] Unlike Ref. 2 that attempts to find minimum free-energy configurations at positive temperatures, Ref. 9 bases their claims only on lattice sums for a limited number of possible crystal configurations.

Chapter 3

Designed Diamond Ground State via Optimized Isotropic Monotonic Pair Potentials

Advances in the field of self-assembly, devising building blocks (*e.g.*, nanoparticles and polymer chains) with specific interactions to form larger functioning materials, are proceeding rapidly and hold great promise to produce unique colloidal and polymer systems [1, 2, 3, 4]. In the past several years, inverse statistical-mechanical methods have been formulated that yield optimized interactions that robustly and spontaneously lead to a *targeted* many-particle configuration with desirable or novel bulk properties [5]. This inverse approach provides a powerful and systematic means of directing self assembly with exquisite control. Recent studies have used inverse methods to find optimized isotropic (non-directional) interactions, subject to certain constraints, that yield novel targeted ground states, such as low-coordinated crystal structures [5]. This includes the three-fold coordinated honeycomb (or graphene) structure in two dimensions [6] and the tetrahedrally-coordinated diamond crystal in

three dimensions [7], initial studies of which involved isotropic pair potentials with multiple wells.

Are multiple wells required to achieve low-coordinated crystal ground states with isotropic pair interactions? We have recently shown that inverse statistical-mechanical techniques allow one to produce unequivocally both the square lattice and honeycomb crystal in two dimensions via monotonic convex pair potentials [8, 9]. Here, we use inverse techniques to obtain a simple family of optimized isotropic, monotonic pair potentials (that may be experimentally realizable by colloids [5]) whose ground states for a wide range of pressures is the diamond crystal. This possibility is counterintuitive since the diamond crystal is commonly thought to require directional (covalent) interactions.

Using the *forward* approach [10], it was established over a decade ago that the diamond crystal can be stabilized for a range of densities by an isotropic, monotonic pair potential devised to model star polymers [11]. These authors used free-energy calculations to find the phase diagram and validate their conclusions. Moreover, the potential possessed stable phonon spectra over the predicted ground-state parameter regime [12]. A forward approach was used in another study [13] to examine only lattice energy sums at zero temperature for a relatively small set of Bravais and non-Bravais lattices for an isotropic, monotonic pair potential. It was found that the diamond crystal was stable for a certain pressure range. These authors recognized the limitations of this restricted investigation, which excluded both phonon spectra calculations and annealings to zero temperature from liquid-like initial conditions in order to validate that the diamond was indeed the ground state.

Here we use a simpler functional form for a monotonic radial (isotropic) pair potential function $v(r)$ that obeys certain important conditions on its second derivative with respect to the radial pair distance r established in Refs. [8] and [9]. Specifically, we propose a potential function of the form

$$v(r) = \varepsilon \left(1 + a_1 \frac{r}{\sigma} + a_2 \left(\frac{r}{\sigma}\right)^2\right) e^{-(r/\sigma)^2}, \tag{3.1}$$

where ε and σ, respectively, define the energy and length units, and a_1 and a_2 are dimensionless parameters. Equation (3.1) is chosen for its simplicity and because it allows for the desirable features of the second derivative described below. The potential function (3.1) is strictly convex for all r beyond a small cutoff distance for a large range of parameters. In this study, we restrict ourselves to such potentials that are convex for $r > 0.1\sigma$ [14].

We introduce here an iterative two-step inverse procedure to determine the optimized parameters of the potential function (3.1) under certain constraints that yields the diamond ground state for a range of pressures. Let $p^* = p\sigma^3/\varepsilon$ and $\rho^* = \sigma^3\rho$ be a dimensionless pressure and dimensionless density, respectively. The first step of the optimization procedure involves choosing an initial set of "competitor" configurations. Then we find the parameters a_1 and a_2 that maximize the ratio p_{max}/p_{min} (maximum to minimum pressure) for which the diamond has a lower enthalpy than any competitor configuration. This use of the pressure range as an optimization variable is new to our knowledge. The second step involves a rapid cooling procedure within a simulation box under periodic conditions in the isobaric ensemble, implying that the box is deforming and changing volume. We start this step by choosing initial lattice vectors that define the box within which are N particles initially Poisson distributed in space interacting via the potential (3.1) with parameters from the first step. Cooling is achieved using a quasi-Newton method, which has similar basins of attraction as obtained from steepest-descent methods or Metropolis schemes at zero temperature. The basis number N for the periodic cell is varied from 1 to 16 (*i.e.*, we sample over variable-basis crystals) over the entire pressure range defined by p_{min} and p_{max}. If we find a lower enthalpy configuration than that for the diamond crystal, we add that configuration to the competitor list and the two-step procedure is

iterated. If we find no other states with lower enthalpy, we terminate the procedure. Knowledge of the final set of competitors allows us to choose a potential (without a full-blown optimization) that has other useful qualities at the cost of only a small decrease in the pressure range over which diamond is the ground state, e.g., for the system to be relatively stiff mechanically as measured by the phonon spectrum.

After optimization under the aforementioned constraints (*e.g.*, relative stiffness and convexity for $r > 0.1\sigma$), we obtain the following optimized parameters for the potential (3.1) [15]:

$$a_1 = -1.42324, \qquad a_2 = 0.713012. \tag{3.2}$$

Henceforth, we will refer to the potential function (3.1) with parameters defined by (3.2) as the diamond-1 or D1 potential [16]; see Fig. 3.1(a). The diamond crystal is the ground state of the D1 potential from $p^* = 0.0554$ to $p^* = 0.1010$. At these pressures, the corresponding densities and nearest-neighbor (NN) distances are, respectively, $\rho^* = 0.235$ and $\rho^* = 0.303$, and $r_{NN} = 1.403\sigma$ and $r_{NN} = 1.290\sigma$. The second derivative d^2v/dr^2 is designed to meet two simultaneous objectives: (a) to stabilize the low-coordinated target structure, and (b) to discriminate against all competitors. Specifically, using the generalized coordination function formalism [9], we determined that to obtain low-coordinated ground states with monotonic convex potentials, $|d^2v/dr^2|$ must be large both below and close to the NN distance. It also must be small up to to the NN distance of the close-packed crystals and large up to the next NN distance of the targeted low-coordinated ground state, after which it goes to zero.

We also tried to find a monotonic potential of the form (3.1) that has the closely related tetrahedrally-coordinated wurtzite crystal as its ground state, but concluded that such a potential does not exist. Wurtzite and diamond crystals have the same first and second coordination shells, and so the only way a potential (3.1) can dis-

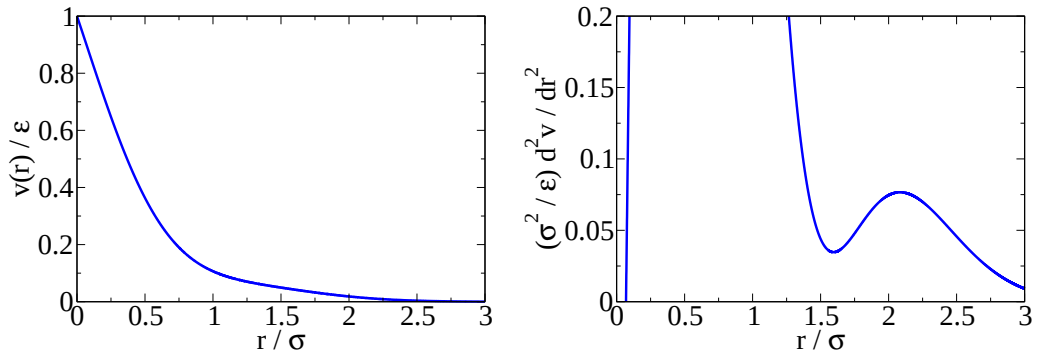

(a) (b)

Figure 3.1: (a) Optimized monotonic pair potential $v(r)$ from Eq. (3.1) using the parameters from (3.2): the D1 potential. (b) Second derivative d^2v/dr^2 of the pair potential versus the radial distance r.

tinguish between the two is from its longer-range behavior. However, such potentials decrease very rapidly at these larger distances due to the dominant Gaussian factor. Thus, wurtzite for potential (3.1) has higher energy than that of diamond, since its third nearest neighbors are slightly closer.

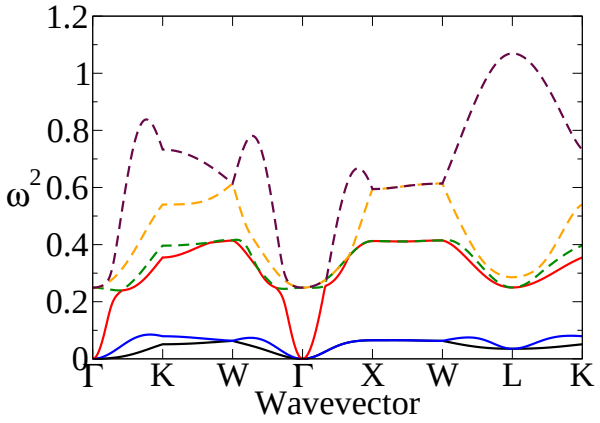

Figure 3.2: Phonon spectrum in reduced units of the D1 potential for the diamond at dimensionless pressure $p^* = 0.078$ and density $\rho^* = 0.271$. Only a representative subset of wave vectors that lie on paths connecting high-symmetry points (Γ, K, W, X, and L) of the Brillouin zone [7] is shown. The D1 potential is chosen such that the lowest phonon frequency relative to the highest one at the X point is maximized.

The mechanical stability of the diamond crystal for the D1 potential is confirmed by phonon calculations, as done in Ref. [7], over the entire Brillouin zone [17]. Figure 3.2 shows the phonon spectrum (reflecting strengths of the restoring forces for defor-

mations for given wave vectors) at a pressure in the middle of its stability range. The optimized D1 potential is selected among those potentials that yield nearly optimal pressure range for the diamond ground state such that the ratio between the highest and lowest phonon frequencies at the X point is maximized. But it is also optimal for other wave vectors that we studied.

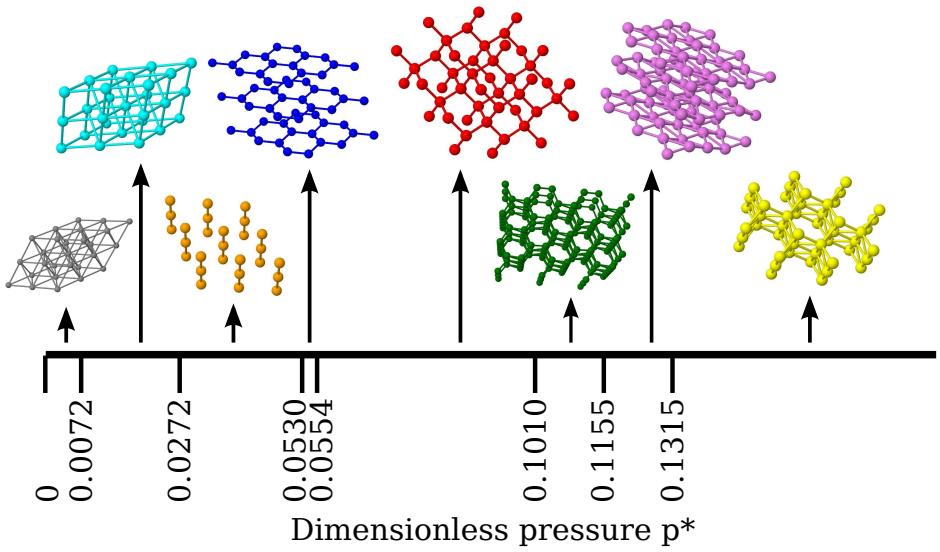

Figure 3.3: Ground states of the D1 potential for a range of pressures obtained from steepest descent for a basis up to $N = 16$. The crystal phases indicated from zero pressure to higher pressures are the 12-coordinated face-centered cubic (gray), the 8-coordinated body-centered cubic (cyan), a 2-coordinated hexagonal (orange), a 3-coordinated buckled rhombohedral graphite (blue), the 4-coordinated diamond (red), a 5/6-coordinated deformed diamond (green), a 6-coordinated buckled hexagonal (violet), and a 8-coordinated flattened-hexagonal closed-packed (yellow). "Bonds" are indicated between nearest-neighbor particles for visualization purposes.

The stable phases for the D1 potential at various pressures outside those for the diamond stability range are shown in Fig. 3.3. The phases are determined by repeatedly cooling disordered configurations at constant pressure using the aforementioned the variable-box energy minimization techniques and retaining the lowest-enthalpy configurations. We find that the diamond is stable for $0.0554 \leq p^* \leq 0.1010$. Four neighboring phases are particularly interesting. At low pressures, $0.0272 < p^* < 0.0530$, a hexagonal crystal phase, where the distance between hexagonal planes is shorter

than the distance between particles in the same plane, is stable. This crystal has an effective coordination number of two. Between this phase and the diamond phase ($0.0530 < p^* < 0.0554$), a low-coordinated rhombohedral graphite phase is stable. It is composed of stacked honeycomb layers where each successive layer is shifted in the same direction relative to the layer immediately below it (unlike standard graphite where the shift direction alternates between layers). The distance between the planes is about 1.5 times larger than the NN distance within a layer, which is much less than that for actual graphite. At high pressures in the range $0.1155 < p^* < 0.1315$, the opposite happens, since the stable phase is a *buckled* simple hexagonal crystalline, where the NN distance within a hexagonal plane is shorter than that between planes, resulting in a coordination number of six. Unlike the low-pressure hexagonal phase, this phase shows buckling: particles in the same layers are not perfectly aligned, but the distance between nearest neighbors stays constant. The transition between the high-pressure buckled hexagonal phase and the diamond phase ($0.1010 < p^* < 0.1155$) consists of a highly deformed diamond crystal, for which particles have variable coordination numbers of either 5 or 6. The highest-pressure phase reported is a flattened hexagonal closed-packed crystal in which the NN distances within a layer are larger than that between layers. This is not the stable phase for all $p^* > 0.1315$; other phases arise at higher pressures.

We employed the same rapid cooling method used to obtain the phase diagram to quantify how easy it is for the system to reach the ground state. Table 3.1 compares the frequency with which the diamond is obtained using the D1 and the star-polymer [11] potentials for various numbers of particles, demonstrating an advantage of the D1 potential. The high frequency with which the D1 potential results in the diamond is evidence that its energy landscape is smooth and possesses a broad global minimum; see Fig. 3.4(c). The fact this frequency decreases as N increases is a consequence of the relative crudeness of our rapid cooling method, which is ineffective at resolving

N	D1 potential	Star-polymer potential
2	96.89%	91.41%
4	89.71%	77.38%
8	62.13%	54.28%
16	46.32%	26.55%
32	24.57%	8.93%
64	5.27%	0.30%

Table 3.1: Frequency with which the ground-state diamond crystal is obtained from a steepest descent starting from a random configurations of N particles. For each N, the frequency is calculated using 10000 trials, which results in standard deviations smaller than 0.5%. The D1 potential trials are carried out at $p^* = 0.078$, while the star-polymer potential trials used $p/(\frac{5}{18}k_BTf^{3/2}) = 3.332$ (for which the ground state has a "packing fraction" $\eta = 1.2$) and an arm number $f = 64$ (see Ref. [11] for the definition of these parameters).

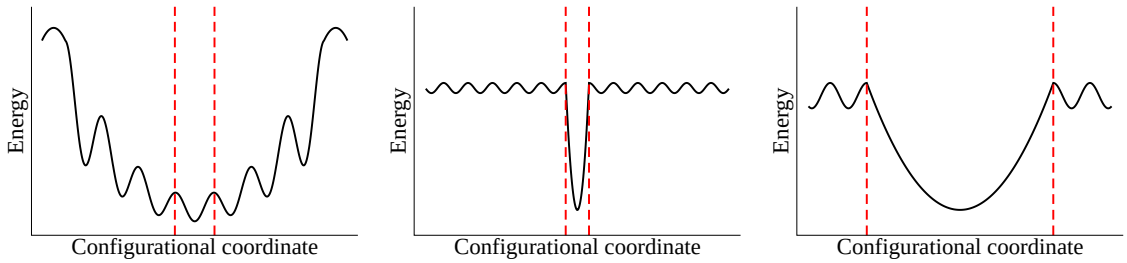

(a) (b) (c)

Figure 3.4: Schematics of three different types of energy landscapes as a function of the configurational coordinate. Boundaries of the basin of attraction associated with the global minima are indicated by dashed vertical lines. (a) Relatively rough energy landscape. (b) Energy landscape with a deep and narrow global minimum. (c) Energy landscape with a broad and smooth global minimum.

large-scale defects. However, it is all the more remarkable that this method is capable of reaching the ground state with reasonable frequency despite using large bases, as opposed to, for example, a carefully-tuned simulated annealing procedure. Nevertheless, we have verified using simulated annealing on a 256-particle system that the diamond crystal emerges as the ground state for the D1 potential.

Our work provides yet another example of the "inverse" statistical mechanical method to identify an appropriate interaction potential whose non-degenerate classical ground state is a pre-selected crystal structure. In general, it is not guaranteed

that such a targeted requirement has a solution. But in the present case of the fourfold-coordinated diamond crystal, previous studies have indeed indicated that this can be accomplished with pairwise additive isotropic potentials [7, 11, 13]. The existence of these examples establish that an infinite family of such interactions will produce the diamond structure as its ground state, each member within some pressure (*i.e.*, density) range.

However, merely stabilizing a given target structure is typically only part of the technical objective. There may be other properties that one wishes simultaneously to satisfy or optimize. Here, these have included maximizing the pressure range of ground-state stability for the diamond crystal, constraining the potential to monotonicity and convexity, maximizing the ratio of the the highest and lowest phonon frequencies, and optimizing capture probability in the desired crystal basin from random initial configurations. The choice of such constraints and/or optimizations is not unique, but is driven by overall scientific objectives. Distinct choices obviously will identify distinct optimizing potential functions.

The success at constructing diamond potentials naturally raises the question of whether the structure of that other macroscopic crystalline form of elemental carbon, graphite, might analogously be the classical ground state of an isotropic pair potential. This might seem easy, given the existence of potentials that generate the two dimensional analog, the honeycomb crystal [6, 8, 9]. However, the layered structure of this three-dimensional graphite allotrope, the stable form of elemental carbon at ambient conditions, with rather large interlayer separation and interlayer relative shift, realistically appears to present a formidable challenge. Ideally, it is desirable to find a potential whose ground state includes both the graphite structure (at low pressure) and the diamond structure (at elevated pressure), thus emulating reality. This ambitious joint requirement might require at least a combination of two-body and three-body interactions, suggesting a direction for future research.

At present there is no known constraint on the complexity (basis of the unit cell) of a single-species target crystal structure that might be stabilized by an isotropic pair potential. But as the unit cell of a target crystal structure increases in size and geometric detail, it is reasonable to suppose that stabilizing isotropic pair potentials, if they exist, will necessarily also have to increase in range and complexity. Establishing such a connection constitutes another direction in which future studies should be focused.

Bibliography

[1] M. Grzelczak, J. Vermant, E. M. Furst and L. M. Liz-Marzan, *Directed Self-Assembly of Nanoparticles*, ACS Nano **4**, 3591 (2010).

[2] D. J. Kraft, R. Ni, F. Smallenburg, M. Hermes, K. Yoon, D. A. Weitz, A. van Blaaderen, J. Groenewold, M. Dijkstra and W. K. Kegel, *Surface roughness directed self-assembly of patchy particles into colloidal micelles*, Proc. Nat. Acad. Sci. **109**, 10787 (2011).

[3] D. Frenkel and D. J. Wales, *Colloidal self-assembly: Designed to yield*, Nature Mater. **10**, 410 (2011).

[4] J. Shengxiang, U. Nagpal, W. Liao, C-C. Liu, J. J. de Pablo and P. F. Nealey, *Three-dimensional Directed Assembly of Block Copolymers together with Two-dimensional Square and Rectangular Nanolithography*, Adv. Mater. **23**, 3692 (2011).

[5] S. Torquato, *Inverse optimization techniques for targeted self-assembly*, Soft Matter **5**, 1157 (2009).

[6] M. Rechtsman, F. H. Stillinger and S. Torquato, *Optimized Interactions for Targeted Self-Assembly: Application to a Honeycomb Lattice*, Phys. Rev. Lett. **95**, 228301 (2005).

[7] M. Rechtsman, F. H. Stillinger and S. Torquato, *Synthetic diamond and wurtzite structures self-assemble with isotropic pair interactions*, Phys. Rev. E **75**, 031403 (2007).

[8] É. Marcotte, F. H. Stillinger, and S. Torquato, *Optimized monotonic convex pair potentials stabilize low-coordinated crystals* , Soft Matter **7**, 2332 (2011).

[9] É. Marcotte, F. H. Stillinger, and S. Torquato, *Unusual ground states via monotonic convex pair potentials*, J. Chem. Phys. **134**, 164105 (2011).

[10] The forward approach specifies interparticle interactions for a many-particle system and then studies structural, thermodynamic and kinetic features of the system.

[11] M. Watzlawek, C. N. Likos, and H. Lowen, *Phase Diagram of Star Polymer Solutions*, Phys. Rev. Lett. **82**, 5289 (1999).

[12] C. N. Likos, private communication (2006). Phonon spectra were not provided in Ref. [11].

[13] S. Prestipino, F. Saija, and G. Malescio, *The zero-temperature phase diagram of soft-repulsive particle fluids* , Soft Matter **5**, 2795 (2009).

[14] Since the nonconvexity of the potential is restricted to very small distances, one can add a short-range hard-core repulsion to Eq. (3.1) to obtain a convex potential, which will behave exactly like the original potential, provided that the pressure or temperature is not extremely large.

[15] This diamond potential function is robust with respect to perturbations of its parameters.

[16] For example, we denote by D2 the potential that has the largest ratio of maximum to minimum stable pressures for the diamond ground state. Its parameters are

$a_1 = -1.21189$, and $a_2 = 0.788955$. This potential possesses softer transverse phonon modes compared to the D1 potential.

[17] N. W. Ashcroft and N. D. Mermin, *Solid State Physics* (Holt, New York, 1976).

Chapter 4

Designer Spin Systems via Inverse Statistical Mechanics: Ground State Enumeration and Classification

4.1 Introduction

Interactions between the atomic or molecular particles contained in condensed phases produce an enormous diversity of geometric structures and resulting material properties. This diversity is of incalculable value to technology, while presenting fascinating scientific challenges to the research community for interpretation. This chapter reports analytical and computational results extending an initial investigation that focused on geometric pattern production in classical spin system ground states [1]. Because the present work and its predecessor basically involve starting with a given *target* pattern, then searching for an optimal radial interaction function to attain that

pattern as a classical ground state, the central strategy utilized has been classified as belonging to "inverse statistical mechanics" [2, 3, 4, 5, 6, 7].

As in a preceding paper [1] attention here focuses on static polarization patterns that can be exhibited by arrays of interacting Ising spins $\sigma_i = \pm 1$ $(1 \leq i \leq N)$ on a d-dimensional lattice, in the absence of external fields. The N spins constitute a finite unit cell that is periodically replicated over the infinite lattice; that is, this cluster of N spins is subject to periodic boundary conditions. In the cases to be examined here the lattices are Bravais lattices, and therefore all spin locations are geometrically identical.

Ising models have a venerable history, introduced originally to explain the phenomenon of ferromagnetism [8, 9]. Although the early versions of the Ising model considered only interactions between nearest neighbors on the lattice of interest [8, 10, 11, 12], subsequent investigations have extended the analysis to incorporate longer-ranged interactions [13, 14, 15, 16, 17, 18, 19]. Assuming that the interactions among the Ising spins are pairwise-additive and radial (*i.e.*, isotropic), the total interaction energy E for the unit cell can be represented as follows:

$$E(\sigma_1, \ldots, \sigma_N) = -\sum_{i<j} J(R_{ij})\sigma_i\sigma_j, \tag{4.1}$$

where the sum covers all of the interactions of the N spins in the unit cell [20], and R_{ij} stands for the scalar distance between the i, j spin pair. Because the spins and their periodic images reside on a lattice, all possible distances R_{ij} form a discrete set. The summation in Eq. (4.1) includes all distances in that set up to a cutoff value R_C beyond which $J(R_{ij})$ becomes identically zero.

A basic descriptor for any single spin pattern on a lattice is the following spin-spin correlation function defined for the discrete set of inter-spin distances occurring on

the lattice:

$$S_2(R) \equiv \frac{1}{N} \sum_{i<j} \sigma_i \sigma_j \delta_{R,R_{ij}}, \tag{4.2}$$

in which $\delta_{R,R_{ij}}$ is a generalized Kronecker delta [21]. This definition permits the energy per spin ϵ, for any spin pattern, to be simply written as

$$\epsilon \equiv \frac{E}{N} = -\sum_{R>0}^{R_C} J(R) S_2(R). \tag{4.3}$$

The fact that the spin-spin interaction potentials to be considered herein only depend on scalar distances implies that the energy per spin ϵ can experience pattern degeneracies. Some of these are trivial, arising from various pattern symmetries (boundary conditions permitting), such as translations, rotations, spatial and spin inversions, and combinations thereof. In addition there can arise pairs (or larger numbers) of distinct spin patterns not related by symmetry that happen to possess identical $S_2(R)$ correlation functions for all R, specific examples of which have been previously identified [1]. If that is the case, then ϵ will be identical for these distinct patterns regardless of the spin-spin interaction potential $J(R)$. We will call the set of all Ising spin configurations on a given underlying lattice which possess the same $S_2(R)$ function an "iso-S_2 set". The elements of an iso-S_2 set that are related by combinations of symmetry operations will simply be regarded as trivial degeneracies. By contrast, the largest subset of spin patterns (configurations) in an iso-S_2 set that are not related to one another by the aforementioned symmetry operations will be identified as "non-trivial degeneracies". Throughout the remainder of this chapter any allusion to degenerate spin configurations will in fact refer to non-trivial degeneracies, the number of which is denoted by Ω for any given iso-S_2 set.

With respect to Ising model energy degeneracies, an historical note may be of passing interest. Specifically, the two-dimensional Ising models with nearest-neighbor antiferromagic interactions ($J(1) < 0$) on both the triangular Bravais lattice [22] and

on the non-Bravais Kagomé lattice [23] have ground states with high-order degeneracies. In fact these degeneracies confer positive residual entropies on the ground states in the infinite-system size limit. However, these antiferromagnetic situations do not conform to the type of pattern analysis implemented in this chapter, where finite Ising spin patterns are periodically replicated, and where spin-spin interaction potentials $J(R)$ are sought to produce non-degenerate ground states when possible.

In Ref. [1] we classified target spin configurations according to three solution class designations. In terms of the iso-S_2 formalism just introduced, these solutions classes can be equivalently restated as follows:

- **CLASS I:** An iso-S_2 set with no (non-trivial) degeneracies for which a spin-spin interaction potential $J(R)$ can be constructed for which the iso-S_2 set is a corresponding unique ground state.

- **CLASS II:** An iso-S_2 set exhibiting 2 or more (non-trivial) degeneracies for which a spin-spin interaction potential $J(R)$ can be constructed such that the energy per spin ϵ for each member of the iso-S_2 set is lower than that of all configurations outside the set.

- **CLASS III:** Any iso-S_2 set that belongs to neither Class I nor Class II. This is equivalent to stating that any iso-S_2 set for which any assigned interaction $J(R)$ produces a higher energy per spin, or an equal energy per spin, compared to spin configurations from at least one other set, belongs to Class III.

The principal objective of this chapter is to separate all possible iso-S_2 sets of spin configurations of a given unit cell size into those that can be unique classical ground states with an energy of the form Eq. (4.1), from those that cannot. The total number of possible spin patterns for a system containing N spins is 2^N (many of which are trivial degeneracies), thereby limiting the exhaustive searches considered in this work to modest system sizes. For the $d = 1$ integer lattice, we considered systems as large

as $N = 21$, while for the $d = 2$ square lattice, we have considered both square and rectangular unit cells, the largest of which contains $N = 25$ spins in a 5×5 unit cell. In spite of the modest sizes of the unit cells examined herein, it is worth noting that population trends for the three distinct solution classes can still be identified as N increases.

In this investigation, we have obtained lower bounds on Ω for the iso-S_2 sets, which are sharp for all of the 1D integer and for most of the 2D square lattice sets, and have uncovered the relationship between Ω and system size for spin configurations on the 1D integer lattice. Using these enumeration results, we have employed inverse statistical-mechanical techniques to assign solution class designations (Class I, II, or III) corresponding to each of the iso-S_2 sets and have found their relative occurrences for different system sizes. In doing so, we also determined the minimal radial extent of the spin-spin interaction potentials required to stabilize iso-S_2 sets belonging to Class I and II. In this chapter, we show that inverse statistical-mechanical techniques can successfully create radial spin-spin interactions for which spin configurations with minimal symmetry are the unique classical ground states. The existence of these unique ground states opens the field of inverse methods toward much more unusual targets than have previously been studied in both spin [1] and many-particle systems [2, 3, 4, 5, 6, 7], which could aid in the design of materials with desired properties. By contrast, we demonstrate that many candidate targets cannot be the unique classical ground states of any radial spin-spin interactions, either due to S_2-type degeneracies (Class II), or from guaranteed non-S_2-type degeneracies (Class III).

The subsequent sections in this chapter are arranged as follows. Section 4.2 presents a detailed description of the methods used to search for energy-minimizing isotropic interactions, and to identify spin patterns and their corresponding interaction potentials according to the Class I, II, and III criteria stated above. Section 4.3 describes in detail the extensive results generated by our method for the modest-size

systems examined on the integer and square lattices with periodic boundary conditions. The final Section 4.4 contains the discussion and conclusions, specifically including our estimates of the most productive directions in which future research regarding these pattern-controlling phenomena might proceed.

4.2 Methods

This section is dedicated to the descriptions of the various technical aspects of this research. In Section 4.2.1, we define both of the underlying lattices considered in this work: the one-dimensional (1D) integer and two-dimensional (2D) square lattices. In Section 4.2.2, we describe the protocol we have utilized to consider every spin configuration discretized on a given underlying lattice with a given periodicity. Finally, Section 4.2.3 describes the inverse statistical-mechanical techniques that we employed to classify the different iso-S_2 sets and create spin-spin interaction potentials that correspond to ground states comprising the Class I and II sets. These techniques have previously been employed in Ref. [1].

4.2.1 The Integer ($\mathbb{Z}$) and Square ($\mathbb{Z}^2$) Lattices

A generalized Ising model with an energy defined according to Eq. (4.1) can be discretized on any given underlying lattice as long as the distance between any two spins is well-defined. Traditionally speaking, the Ising model has most often been studied on either the square or triangular lattices [24, 25], but investigations on more exotic networks, such as the Bethe lattice and hyperbolic planes have also appeared in the literature [26, 27, 28]. In this chapter, we restrict our investigation to the 1D integer lattice ($\mathbb{Z}$) and the 2D square lattice ($\mathbb{Z}^2$), with nearest-neighbor distances set to unity in both cases. On the integer lattice, the distance R_{ij} between spins σ_i and

σ_j is simply

$$R_{ij} = |i - j|\,, \tag{4.4}$$

where i and j can take on any integer value. On the square lattice, the distance between spins is

$$R_{ij} = \sqrt{(x_i - x_j)^2 + (y_i - y_j)^2}, \tag{4.5}$$

in which the spin coordinates, $\{x_i, y_i\}$ and $\{x_j, y_j\}$, are also integers. Since both the integer and square lattices are periodic, this allows us to use periodic boundary conditions to approximate the infinite system limit.

Throughout this work, the size of the unit cell for a spin system discretized on the integer lattice will be denoted by n. For this case, the total number of spins, N, is therefore $N = n$ and the only allowed lattice vector is (n). In the same vein, the unit cell size for the square lattice will be denoted by $m \times n$, with $N = mn$ and corresponding lattice vectors taken as $(m, 0)$ and $(0, n)$. Although unit cells characterized by lattice vectors that are not aligned with the $(1, 0)$ and $(0, 1)$ directions can also exist on the square lattice, this set of unit cells was not included in the present study. We note in passing that any spin configuration with such a unit cell can be equivalently represented by a larger unit cell with lattice vectors aligned with the aforementioned canonical directions.

4.2.2 Enumeration Protocol

Unlike continuous point-particle systems, for which there exists an uncountably infinite number of configurations, the spin systems considered herein have discrete degrees of freedom (where each spin can only be $+1$ or -1) which allows for a finite number of spin configurations. We take advantage of this property and explicitly enumerate all spin configurations discretized on the 1D integer and 2D square lattices with specific unit cells. The total number of spin configurations that can be represented on a pe-

riodic underlying lattice with N spins contained within the unit cell is 2^N, since each spin can take on one of two distinct values. In order to obtain an accurate count of the number of iso-S_2 sets belonging to each solution class, it is necessary to enumerate all of the configurations belonging to each of these sets. To do so, we first compute the spin-spin correlation function, $S_2(R)$, given in Eq. (4.2), for all of the 2^{N-1} spin configurations (using spin-inversion symmetry to fix one of the spins reduces the total number of spin configurations by a factor of 2), and store the list of possible $S_2(R)$ functions. Throughout this work, $S_2(R)$ is computed up to the first 100 coordination shells for both of the underlying lattices; however, we have found that the first differing value of $S_2(R)$ (for non-S_2-degenerate spin configurations) always occurs at an R smaller than, or of the order of, the periodicity of the spin configurations in question.

This enumeration method was also adapted to compute the number of non-trivial degeneracies Ω in each iso-S_2 set. In this case, instead of only storing the $S_2(R)$ function for a given iso-S_2 set, we also store a running list of the non-trivial degeneracies contained in this set. Whenever a new spin configuration that is characterized by a previously stored spin-spin correlation function is encountered during the enumeration process, we are left with the task of determining whether or not this configuration is a trivial or non-trivial degeneracy with respect to the members of the corresponding iso-S_2 set. Such a determination can be achieved by comparing the spin configuration to *each* member of the given iso-S_2 set and performing a spin-by-spin check for symmetrical equivalence up to translations, rotations, reflections, and spin inversion. By updating the list with all of the non-trivial degeneracies found, the number of configurations in the list at the end of the enumeration process yields Ω for each iso-S_2 set. However, one apparent weakness of this method is that it fails to identify any of the S_2-degeneracies corresponding to spin configurations that cannot be represented on the unit cell considered during the enumeration; hence, the values of Ω computed

utilizing this protocol are strictly lower bounds (see Figs. 4.6 and 4.7 for illustrative examples).

4.2.3 Generation and Verification of Spin-Spin Interaction Potentials

Throughout this work, we follow the method first employed in Ref. [1] to generate spin-spin interaction potentials, $J(R)$, which yield ground states that are contained within unique iso-S_2 sets (*i.e.*, Class I and II solutions), or to disprove the existence of any such potential (*i.e.*, Class III solutions). Given a spin configuration $\mathscr{T}$ from a targeted iso-S_2 set and a competitor spin configuration C from another iso-S_2 set, the difference in energy per spin between these configurations can be written as

$$\Delta\epsilon^C \equiv \epsilon^C - \epsilon^{\mathscr{T}} = -\sum_R J(R)\left[S_2^C(R) - S_2^{\mathscr{T}}(R)\right], \tag{4.6}$$

which is clearly a linear function of the interaction potential $J(R)$ for each of the interspin separations allowed by the underlying lattice. In order for $\mathscr{T}$ to be the unique ground state corresponding to $J(R)$, $\Delta\epsilon^C$ must be positive for *all* possible competitors C. Since such a calculation is intractable, we instead select the potential which maximizes $\Delta\epsilon^C$ between the target and the competitor(s) that are closest in energy via:

$$z \equiv \max_{J(R)}\left(\min_C \Delta\epsilon^C\right), \tag{4.7}$$

in which z is the objective function. Here the maximization is performed over all allowed potentials, and the minimization is performed over the set of known competitors.

Equations (4.6) and (4.7) can both be expressed as inequalities that are linear in z and $J(R)$. Therefore, standard linear programming techniques, such as the simplex

algorithm, can be used to efficiently find the global optimum value of the objective function. However, the problem as defined above is not bounded, since multiplying all of the $J(R)$ and z by a positive constant has no effect on the inequalities. Therefore, if we already have a valid solution with a positive z value, we could generate solutions with arbitrarily large z values. To solve this issue, we bound all of the $J(R)$ to be in the range: $[-1, +1]$. Such bounded $J(R)$ functions can reproduce any possible interaction potential, up to the aforementioned positive constant.

The potential $J(R)$ is also set to zero for all R larger than some radial cutoff distance R_C, initially set at $R_C = 1$. If the objective function z is identically zero, then this is indicative of the fact that it is impossible for $\mathscr{T}$ to be the unique ground state for any potential $J(R)$ under the given restrictions, since at least one $\Delta\epsilon^C$ will be non-positive for any potential. In this situation, we relax the restrictions by incrementing R_C to the next smallest distance allowed by the underlying lattice and recalculate z. This ensures that our optimization algorithm will find the shortest possible potential for the given target spin configuration. If z remains zero even when allowing for potentials much longer than the periodic cell size, this signifies that $\mathscr{T}$ cannot be a unique ground state, and therefore belongs to Class III. If z is positive, we have obtained a putative potential $J(R)$ for which we must confirm that $\mathscr{T}$ is indeed its ground state. To do so, we repeatedly use a simulated annealing (SA) procedure using the Metropolis algorithm to relax disordered spin configurations with variable periodic unit cells ($1 \leq n \leq 100$ for the integer lattice, and $1 \leq m \leq n \leq 30$ for the square lattice). If a spin configuration is found that has an energy per spin that is lower than or equal to $\epsilon^{\mathscr{T}}$, but with a different $S_2(R)$ spin-spin correlation function, then this disproves the putative potential $J(R)$. This spin configuration is then added to the list of known competitors, and the optimization is restarted. If we do not find any such competitors before the SA procedure yields the desired target ground state

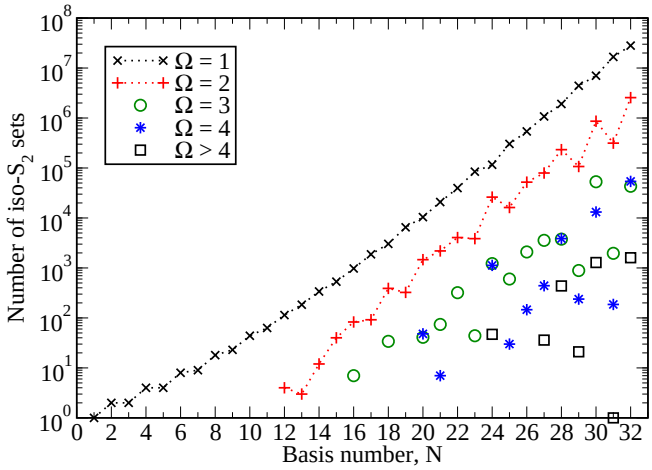

Figure 4.1: The number of iso-S_2 sets which contains a certain number Ω of degenerate spin configurations for spin configurations discretized on the 1D integer lattice with a N spin basis (omitted symbols indicate that no sets have such values of Ω for the given N). For a given N, all sets which contain at least one configuration that can be represented using N periodic spins are included in the enumeration of Ω. A consequence of this is that the Class I ferromagnetic set (with all spins aligned) is included in $\Omega = 1$ for all N.

100 times, then we have amassed sufficiently strong evidence that we have obtained a valid potential.

4.3 Results

4.3.1 The 1D Integer ($\mathbb{Z}$) Lattice

The 1D integer lattice is a very simple yet consequence-rich model to study how the number of degeneracies or the ratio of iso-S_2 sets in the different solution classes vary with the system size. This simplicity is a direct result of the lattice having a single parameter (n) which describes the period of the spin configurations. Figure 4.1 shows how the number of iso-S_2 sets of a given degeneracy, Ω, increases with the basis number $N = n$, regardless of the solution class to which the set belongs. A first observation is that the number of iso-S_2 sets grows exponentially with N, which is relatively unsurprising considering the fact that the total number of spin configurations

also grows exponentially as 2^N. The growth in the number of iso-S_2 sets is actually somewhat slower (approximatively proportional to 1.85^N), a consequence of the fact that the number of trivial degeneracies also increases with N. A second observation is that the number of iso-S_2 sets with different degeneracies Ω apparently have the same rate of exponential growth. This indicates that, even in the infinite size limit, the vast majority of the sets remain non-degenerate ($\Omega = 1$).

This property is a peculiarity of the underlying integer lattice, for which the radially-averaged $S_2(R)$ function contains exactly the same information as the directional spin-spin correlation function $\widehat{S}_2(\mathbf{R})$, since $\widehat{S}_2(\mathbf{R}) = S_2(R = |\mathbf{R}|)$ for any vector and spin configuration discretized on the 1D integer lattice. In general, we can also define a directional spin-spin correlation function $\widehat{S}_2(\mathbf{R})$ which is more appropriate for anisotropic pairwise interactions:

$$\widehat{S}_2(\mathbf{R}) = \frac{1}{N} \sum_{ij} \sigma_i \sigma_j \delta_{\mathbf{R},\mathbf{R}_{ij}}, \tag{4.8}$$

where $\mathbf{R}_{ij}$ is the d-dimensional vector from spin i to spin j. The radial $S_2(R)$ can then be readily obtained from $\widehat{S}_2(\mathbf{R})$ by summing over all equal-length vectors:

$$S_2(R) = \frac{1}{2} \sum_{|\mathbf{R}|=R} \widehat{S}_2(\mathbf{R}), \tag{4.9}$$

where the $1/2$ factor corrects for the double counting in the definition of $\widehat{S}_2(\mathbf{R})$, since $\widehat{S}_2(-\mathbf{R}) = \widehat{S}_2(\mathbf{R})$.

A third observation (see Fig. 4.1) concerns those basis numbers at which the number of doubly-degenerate sets ($\Omega = 2$) is either decreasing or barely increasing: 13, 17, 19, 23, 25, 29, 31. These basis numbers are all of the prime numbers between 12 and 32 (25 being the only exception, although it is a squared prime number). We have

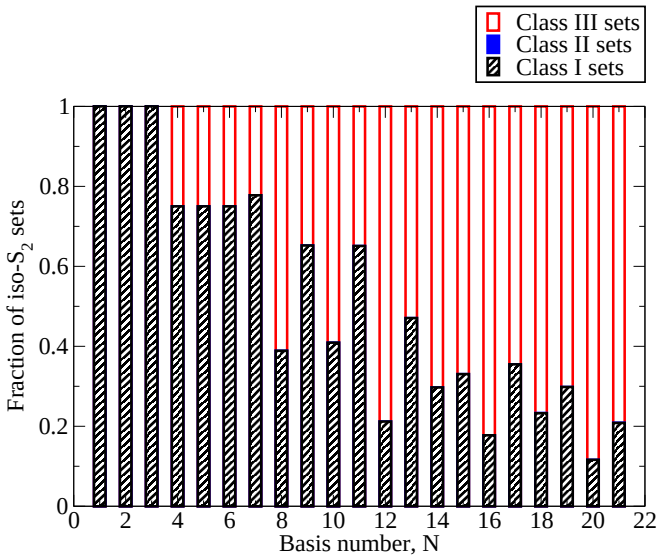

Figure 4.2: The relative amount of iso-S_2 sets that are in Classes I, II, or III, for spin configurations discretized on the 1D integer lattice with an N spin basis. Although it is essentially imperceptible in this figure, we found 2 Class II sets for $N = 18$ (out of a total of 3456 sets). These two sets are depicted in Fig. 4.3. Even though the first Class II sets were found at $N = 18$, this does not mean that there are no S_2 degeneracies for smaller systems. As seen in Fig. 4.1, there are doubly-degenerate sets ($\Omega = 2$) starting at $N = 12$. However, for $12 \leq N \leq 17$, all of these sets belong to Class III. We have also found 18 Class II iso-S_2 sets for $N = 21$ (out of a total of 23 121).

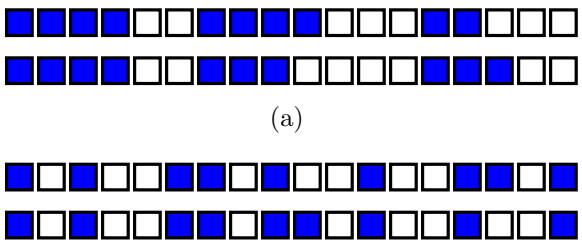

(a)

(b)

Figure 4.3: The two Class II iso-S_2 sets found among 18-spin configurations discretized on the 1D integer lattice, each with a degeneracy $\Omega = 2$.

not studied the cause of this pattern, but it is plausible that the increased occurrence rate of symmetry for non-prime number bases is responsible for the observed trend.

Using the approach described in Sec. 4.2.3, we classified all iso-S_2 sets for the underlying 1D integer lattice with $N \leq 21$, either by generating a potential $J(R)$ for which the ground state is the specified set, or by proving that no such potential exists.

Table 4.1: The spin-spin interaction potentials $J(R)$ corresponding to the two Class II iso-S_2 sets shown in Fig. 4.3. All configurations from both sets have a $N = 18$ spin bases and a potential cutoff of $R_C = 15$. The corresponding spin-spin correlation functions $S_2(R)$ and the energies per spin ϵ are also shown for comparison. Both sets are related through a gauge transformation since the spin configurations from Fig. 4.3(a) can be transformed to the spin configurations from Fig. 4.3(b) by inverting every other spin ($\sigma_i \rightarrow (-1)^i \sigma_i$). This same transformation leads to a S_2 and potential function which have opposite sign for every odd R ($S_2(R) \rightarrow (-1)^R S_2(R)$ and $J(R) \rightarrow (-1)^R J(R)$).

	Figure 4.3(a)		Figure 4.3(b)	
R	$J(R)$	$S_2(R)$	$J(R)$	$S_2(R)$
1	1	1/3	-1	-1/3
2	-1	-1/3	-1	-1/3
3	0.857	-5/9	-0.857	5/9
4	-0.806	-1/3	-0.806	-1/3
5	1	1/3	-1	-1/3
6	-0.714	5/9	-0.714	5/9
7	1	1/3	-1	-1/3
8	-1	-1/3	-1	-1/3
9	0.429	-7/9	-0.429	7/9
10	-0.516	-1/3	-0.516	-1/3
11	0.608	1/3	-0.608	-1/3
12	-0.286	5/9	-0.286	5/9
13	0.887	1/3	-0.887	-1/3
14	-0.427	-1/3	-0.427	-1/3
15	0.143	-5/9	-0.143	5/9
ϵ	-1.303		-1.303	

Figure 4.2 shows the fraction of sets in each solution class for each basis number. The fact that this fraction for class I decreases overall with increased system size is also unsurprising considering the growing complexity that configurations with more spins can achieve. However, it is interesting to note that spin configurations with odd N usually have a higher fraction of Class I sets than spin configurations with neighboring even N. Configurations with odd N being easier to stabilize is likely due to a broken symmetry, although its precise mechanism still need to be understood.

In all of our calculations on the underlying 1D integer lattice, we have only discovered 20 Class II iso-S_2 sets, 2 for $N = 18$ and 18 for $N = 21$. The $N = 18$ Class II

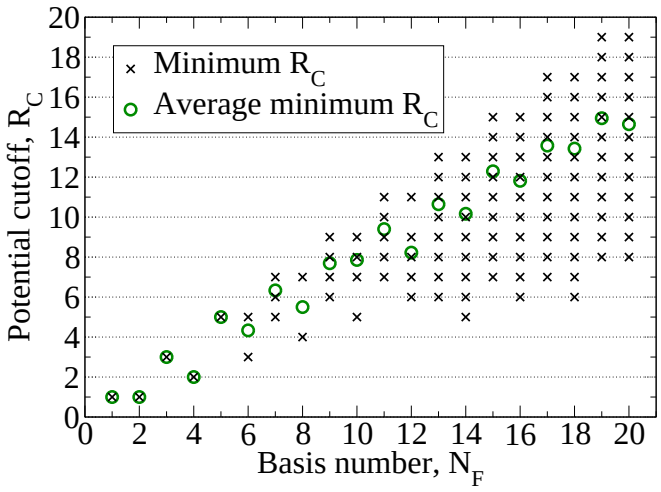

Figure 4.4: The minimal range R_C of the spin-spin interaction potential required to stabilize spin configurations discretized on the 1D interger lattice in term of N_F, the number of spins in the respective fundamental cells. The circles indicate the average R_C for all configurations with the same fundamental cell size.

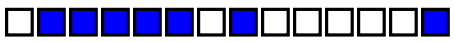

Figure 4.5: The unique spin configuration on the 1D integer lattice with $N_F = 14$ spins in its fundamental cell which can be stabilized using a potential with cutoff $R_C = 5$. Table 4.2 presents one such spin-spin interaction potential.

iso-S_2 sets are shown in Fig. 4.3. The spin-spin interaction potentials corresponding to these degenerate configurations as ground states are presented in Table 4.1.

As mentioned in Sec. 4.2.3, the method utilized to generate spin-spin interaction potentials for a given iso-S_2 set only tries to obtain potentials with a given cutoff R_C after it has already been proved that all shorter potentials are unable to stabilize the set. Therefore, any interaction potential $J(R)$ that the method returns is always going to have the shortest possible cutoff for the targeted set. This property allows us

Table 4.2: The spin-spin interaction potential $J(R)$ corresponding to a ground state (in Fig. 4.5) which has $N_F = 14$ spins even though the potential has a relatively short cutoff at $R_C = 5$. The corresponding spin-spin correlation function $S_2(R)$ and energy per spin ϵ of the potential ground state are also shown.

R	1	2	3	4	5	ϵ
$J(R)$	$-2/9$	1	$2/3$	$-1/3$	$-4/9$	$-46/63$
$S_2(R)$	$1/7$	$3/7$	$1/7$	$-1/7$	$-3/7$	

to explore the range limitations of generalized Ising spin-spin interactions. Figure 4.4 clearly shows the upper bound on the minimal value of the cutoff: $R_C \leq N_F$ if N_F is odd, and $R_C \leq N_F - 1$ if N_F is even, where N_F denotes the number of spins in the fundamental cell of a given spin configuration and the fundamental cell is the smallest repeat unit in the spin configuration (which can be smaller than the unit cell). The $R_C \leq N_F$ upper bound can readily be proven via the following observation: for any spin configuration on the underlying 1D integer lattice with a periodic unit cell containing N spins, $S_2(R = N) = 1$, the maximum value that $S_2(R)$ can achieve on this lattice. Now, let's consider an interaction potential $J(R)$ such that its value at $R = N$ is much larger than all of its other values: $J(N) \gg |J(R)| \quad \forall R \neq N$. Such an interaction potential will clearly favor spin configurations with $S_2(R = N) = 1$ over all others, so its ground state will be represented using a N spin basis. Since $S_2(R + N) = S_2(R)$ for such configurations, any potential longer than N can be shortened to $R_C = N$, without changing its ground state. Therefore, the minimal cutoff R_C has a upper bound equal to N_F, the number of spins in the fundamental cell. The lower bound on R_C is more complex, since it deviates from $R_C \geq N_F/2$ as early as $N_F = 13$. Figure 4.5 shows one spin configuration which breaks that rule, since it has $N_F = 14$ spins in its fundamental cell yet it is the ground state of an interaction potential with a cutoff at $R_C = 5$ (see Table 4.2).

4.3.2 The 2D Square Lattice

Unlike the spin configurations on the underlying 1D integer lattice studied in Sec. 4.3.1, spin configurations on an underlying 2D square lattice can have a wide variety of unit cell lattice vectors. While it is conceivable to enumerate all spin configurations that can be represented with a unit cell containing a specific number of spins, but with otherwise arbitrary lattice vectors, we elect to restrict our investigation in this work to spin configurations with unit cell lattice vectors that

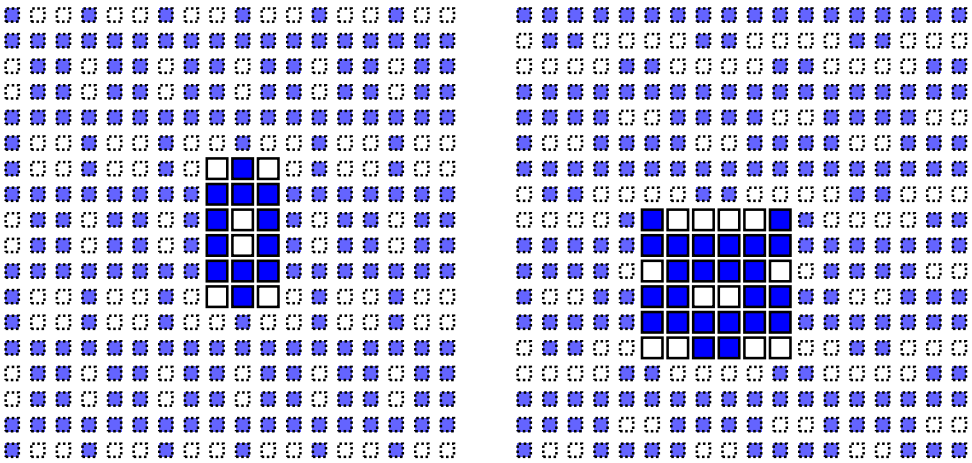

Figure 4.6: An example of two spin configurations that belongs to the same Class II iso-S_2 set, and therefore have identical $S_2(R)$ functions, while having a different number of spins N_F in their fundamental cells. The spins in their fundamental cells are denoted using a solid outline, while other spins are denoted using a dashed outline and smaller squares. The number of spins in their fundamental cells are 18 and 36, respectively.

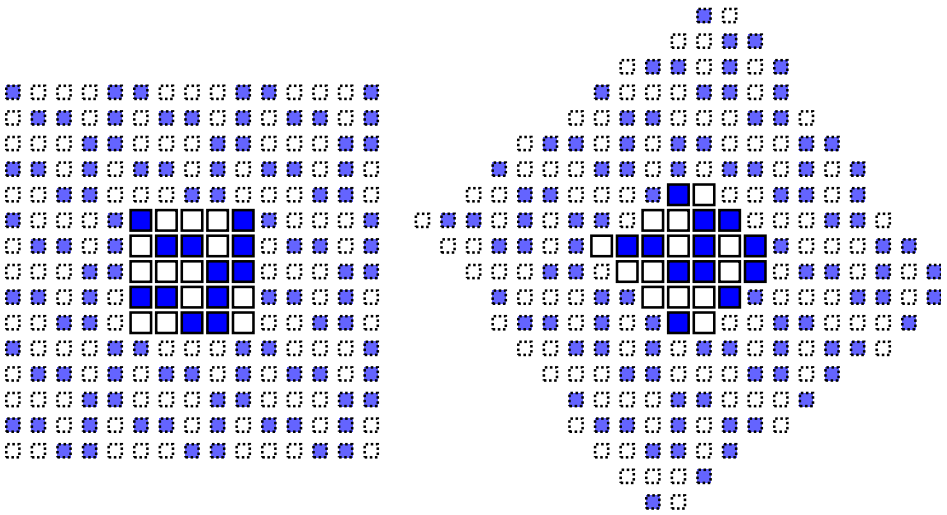

Figure 4.7: An example of two spin configurations that belongs to the same Class II iso-S_2 set, and therefore have identical $S_2(R)$ functions, with differently-aligned fundamental cells. The fundamental cell of the left configuration has $(5, 0)$ and $(0, 5)$ as its basis vectors, while those of the right configuration are $(4, 3)$ and $(3, -4)$. The spins in their fundamental cells are denoted using a solid outline, while other spins are denoted using a dashed outline and smaller squares. Both have $N_F = 25$.

are aligned with the underlying square lattice. Figure 4.6 shows an example of two degenerate spin configurations with not only different fundamental cells, but also different numbers of spins N_F in their fundamental cells. Figure 4.7 shows another example of two degenerate spin configurations with different fundamental cells, which differ only by their orientation instead of by the number of spins. Both of these types of degeneracies will not be identified when computing Ω using brute force enumeration of the spin configurations discretized on a given unit cell. However, when determining whether an iso-S_2 set belongs to Class I or II, we used SA methods to actively look for degenerate configurations with varying unit cells, thereby avoiding such issues.

Spin configurations on the underlying 2D square lattice have many more degeneracies than spin configurations on the underlying 1D integer lattice, as can be seen in Fig. 4.8. This massive increase in the number of degeneracies Ω compared to the 1D enumeration can be attributed to the loss of information when going from an *angular-dependent* spin-spin correlation function $\widehat{S}_2(\mathbf{R})$ to an *angle-averaged* spin-spin correlation function $S_2(R)$, *i.e.*, for which $\widehat{S}_2(\mathbf{R}) = S_2(|\mathbf{R}|)$ is seldom observed. This isotropy prevents $S_2(R)$ from being able to distinguish spin configurations that only differ through the angle dependence of their spin-spin correlations. Since this property is also shared by other 2D lattices as well as higher-dimensional lattices, it makes the square lattice much more representative of what to expect for such lattices.

The classification for all iso-S_2 sets on the underlying 2D square lattice with $1 \leq m \leq n \leq 5$, as well as $1 \leq m \leq 3$ and $n = 6$ is shown in Table 4.3. Just as the 1D iso-S_2 sets are more likely to be in Class III when they have a large basis (see Fig. 4.2), the proportion of 2D iso-S_2 sets in Class III increases when either m or n is increased. The number of Class II iso-S_2 sets also shows the same behavior, since only two of the largest bases for which we have enumerated (3×6 and 5×5) allows for more than 2 Class II iso-S_2 sets. However, a peculiar phenomenon that we have

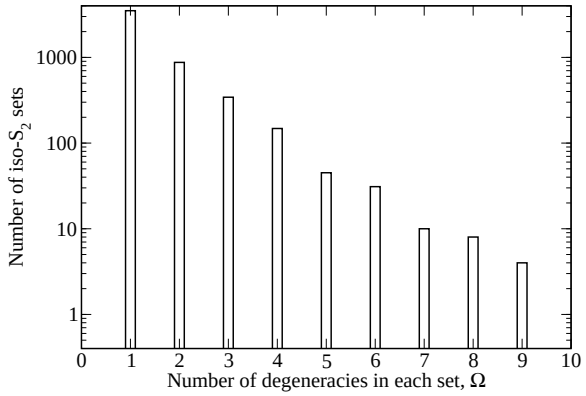

(a)

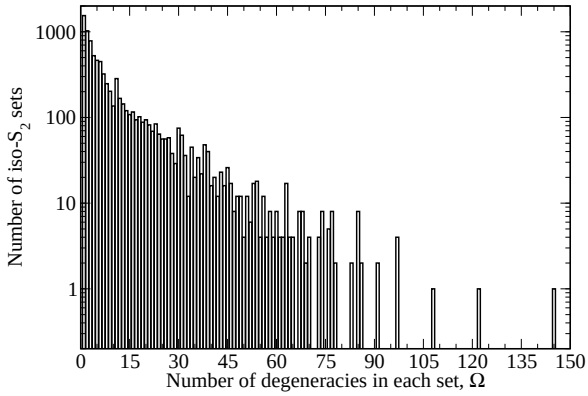

(b)

Figure 4.8: The number of iso-S_2 sets which contains a certain number Ω of degeneracies for spin configurations discretized on the 2D square lattice with (a) a 4×5 basis and (b) a 5×5 basis. Only the degenerate spin configurations which can be represented using the exact same basis have been counted, thereby Ω is only guaranteed to be a lower bound in these cases.

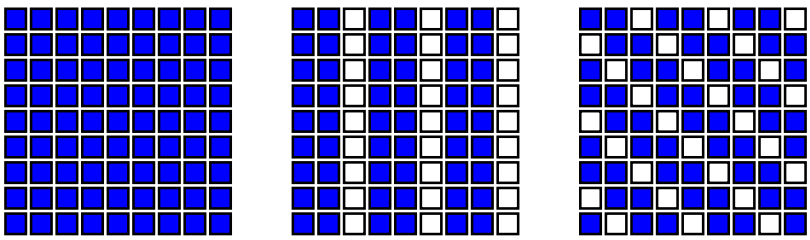

Figure 4.9: All Class I spin configurations which can be represented using a 3×3 basis on the 2D square lattice. The middle spin configuration was previously reported in Ref. [1] as $\mathbf{SP}[1, 2]$.

Table 4.3: The number of iso-S_2 sets of spin configurations with a $m \times n$ basis in each solution class for the underlying 2D square lattice. For each m and n, the data is represented in the following manner: number of Class I sets / number of Class II sets / number of Class III sets. It should be mentioned that all spin configurations which can be represented with the given basis are counted, even if they could also be represented using a smaller unit cell. For example, all 5 of the 4×4 Class I configurations are also 2×4 configurations (see Fig. 4.12). We have also enumerated the sets with 4×6, 5×6, and 6×6 bases. There are respectively 48 914, 1 594 858, and 4 868 629 such sets.

	n					
m	1	2	3	4	5	6
1	1 / 0 / 0	2 / 0 / 0	2 / 0 / 0	3 / 0 / 1	3 / 0 / 1	6 / 0 / 2
2		3 / 0 / 1	6 / 0 / 2	5 / 0 / 15	18 / 0 / 26	23 / 0 / 104
3			3 / 2 / 6	15 / 1 / 65	37 / 2 / 221	31 / 19 / 1030
4				5 / 1 / 266	301 / 2 / 4666	
5					74 / 29 / 8209	

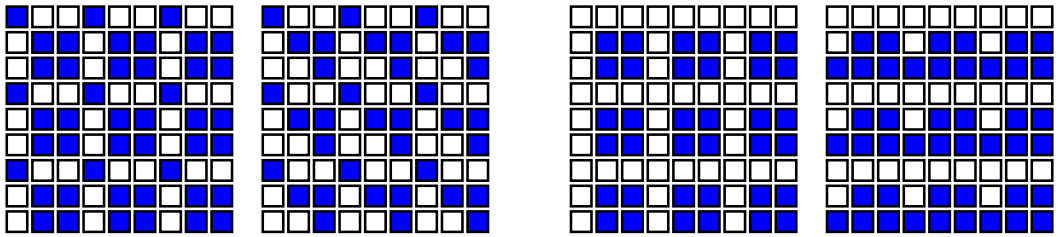

(a) (b)

Figure 4.10: The two Class II iso-S_2 sets containing spin configurations which can be represented using a 3×3 basis on the 2D square lattice. The spin configuration on the left of (a) was previously reported in Ref. [1] as $\mathbf{CB}[1, 2]$.

observed is that the number of Class I iso-S_2 sets in some system sizes is actually lower than the number of Class I iso-S_2 sets in strictly smaller systems, even though the total number of iso-S_2 sets is greater in the former case. For example, there are two times as many Class I iso-S_2 sets among 2×3 spin configurations than among 3×3 spin configurations, three times as many Class I iso-S_2 sets among 3×4 spin configurations than among 4×4 spin configurations, and four times as many Class I iso-S_2 sets among 4×5 spin configurations than among 5×5 spin configurations. In all of these cases, the system size with the lower number of Class I iso-S_2 sets is

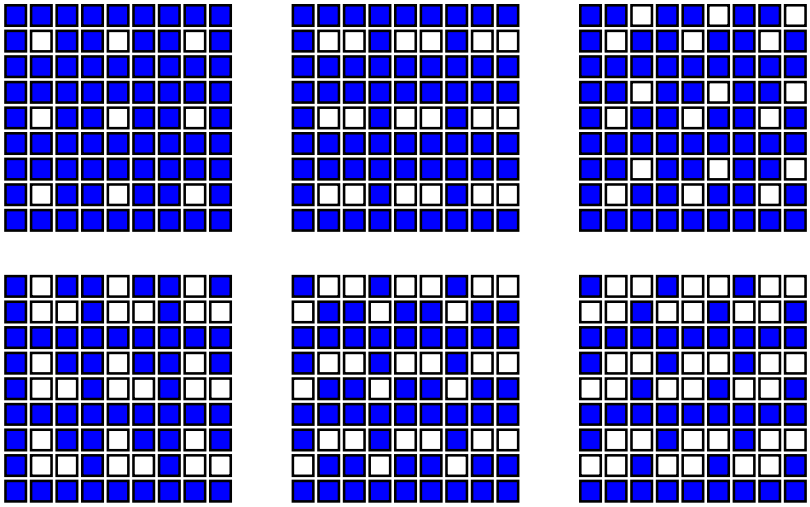

Figure 4.11: All Class III spin configurations which can be represented using a 3×3 basis on the 2D square lattice.

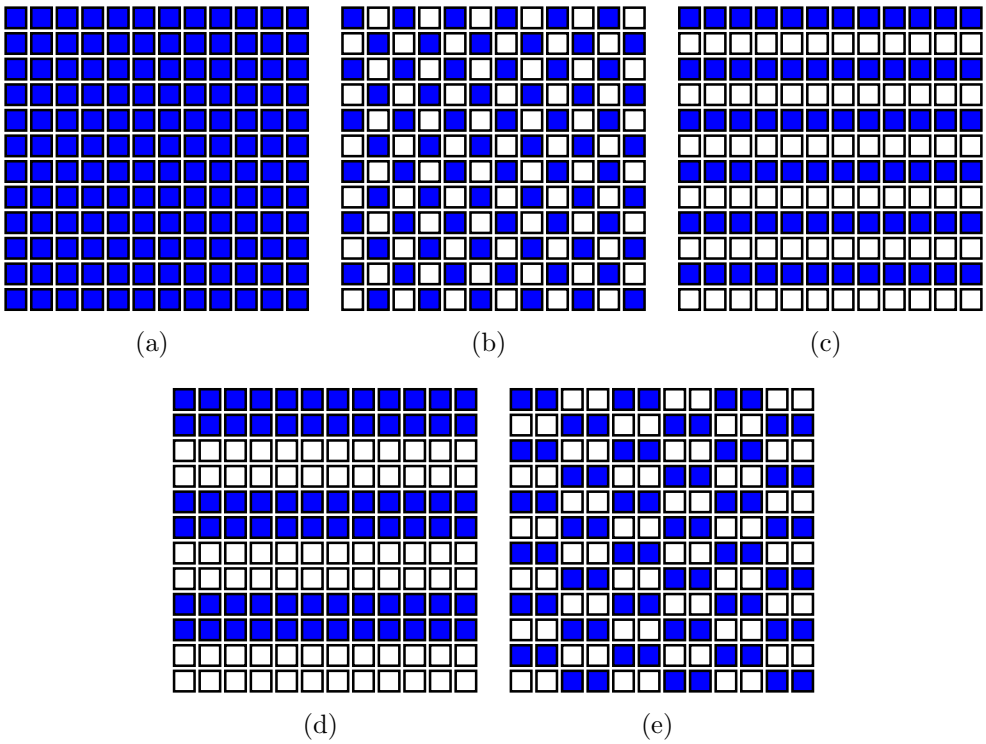

Figure 4.12: All Class I spin configurations which can be represented using a 4×4 basis on the 2D square lattice. All of these spin configurations have been previously reported in Ref. [1] as (a) **FM**, (b) **CB**$[1, 1]$ (the classic anti-ferromagnetic ground state), (c) **SP**$[1, 1]$, (d) **SP**$[2, 2]$, and (e) **SC**$[2, 2]$.

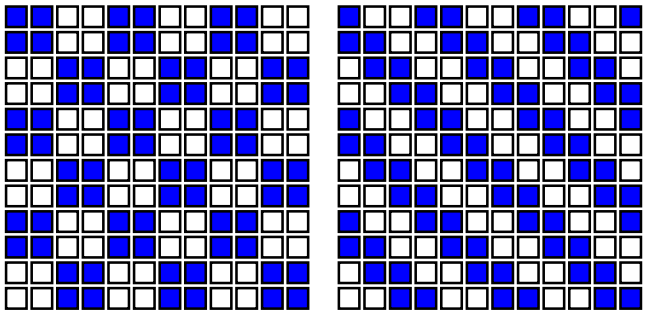

Figure 4.13: The single Class II iso-S_2 set which contains spin configurations which can be represented using a 4×4 basis on the 2D square lattice. This set was previously reported in Ref. [1] as the $\mathbf{CB}_{00}[2,2]$ and $\mathbf{CB}_{11}[2,2]$ block checkerboard spin configurations.

Table 4.4: The spin-spin interaction potential $J(R)$ corresponding to the spin configuration shown in Fig. 4.18. The spin-spin correlation function $S_2(R)$, its maximum value on $\mathbb{Z}^2$, $S_2^{\max}(R)$, and the energy per spin ϵ of the ground states are also shown for comparison. Even though the fundamental cell lattice vectors are of length $\sqrt{5}$ and $\sqrt{8}$, $S_2(R)$ is not maximal for either of these distances.

R	$J(R)$	$S_2(R)$	$S_2^{\max}(R)$
1	0.204	-2/3	2
$\sqrt{2}$	-0.105	0	2
2	-1	-2/3	2
$\sqrt{5}$	1	2/3	4
$\sqrt{8}$	0.645	2/3	2
3	1	4/3	2
$\sqrt{10}$	-0.813	-4/3	4
$\sqrt{13}$	0.523	-4/3	4
4	-1	-2/3	2
$\sqrt{17}$	-0.395	2/3	4
$\sqrt{18}$	-1	2/3	2
ϵ	-3.084		

square (*i.e.*, $m = n$), which indicates that the increased symmetry associated with these system sizes actually disfavors the occurrence of Class I iso-S_2 sets. A subset of the classified sets is also presented in Figures 4.9, 4.10, 4.11, 4.12, 4.13, 4.14, and 4.15.

Unlike the 1D integer lattice case, in which the linear size of the fundamental cell (equal to the number of spins N_F inside of it) is a natural quantity to represent the extent of the smallest periodically-replicated unit of a spin configuration, the 2D

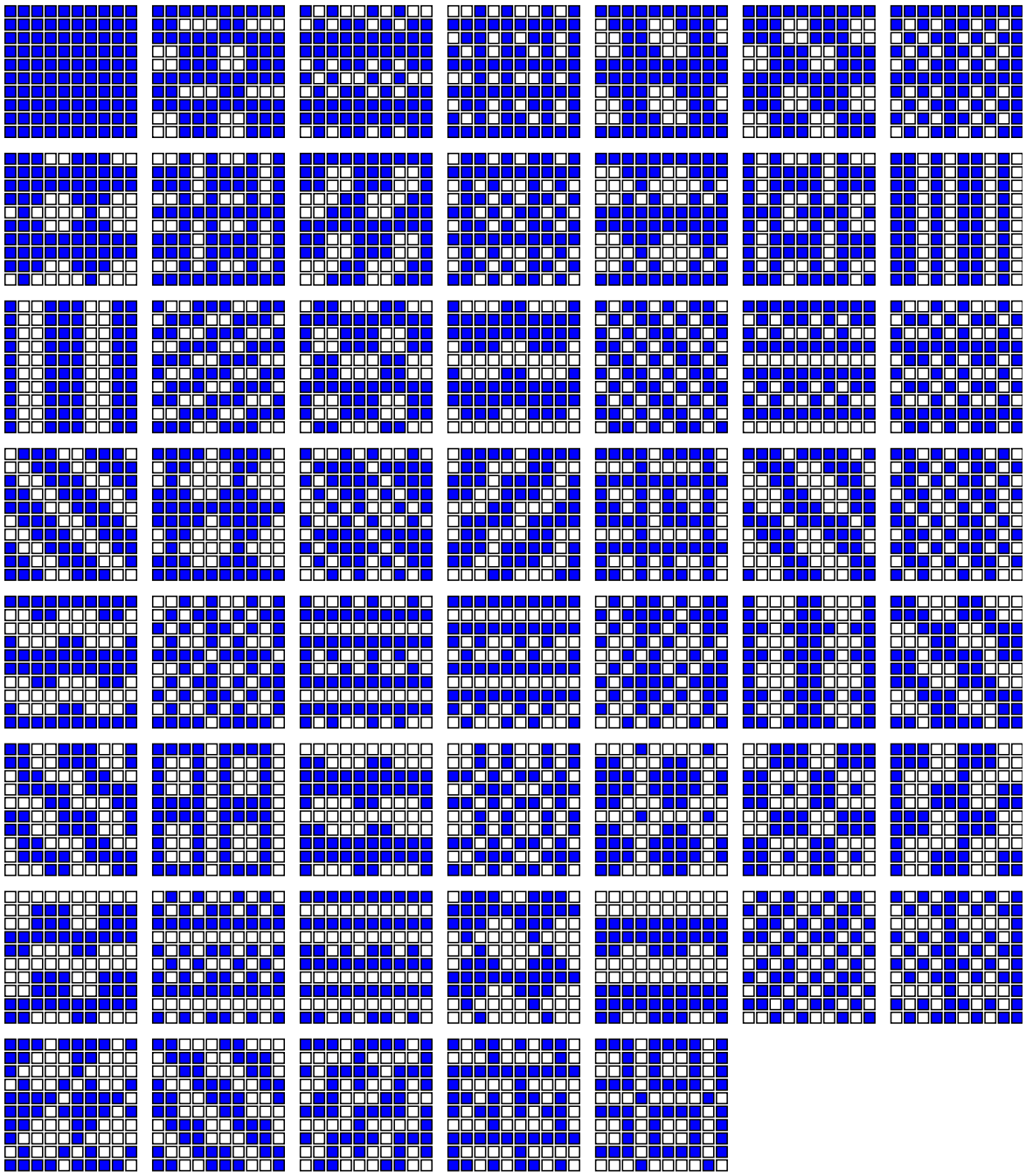

Figure 4.14: All Class I spin configurations which can be represented using a 5×5 basis on the 2D square lattice and are left invariant under some combination of symmetry operations (translations, rotations, reflections, and spin-inversion) besides that which is guaranteed by the underlying 5×5 periodic boundary conditions, displayed left-to-right, top-to-bottom, in order of decreasing absolute magnetization $|\langle\sigma\rangle|$. There are 54 such configurations.

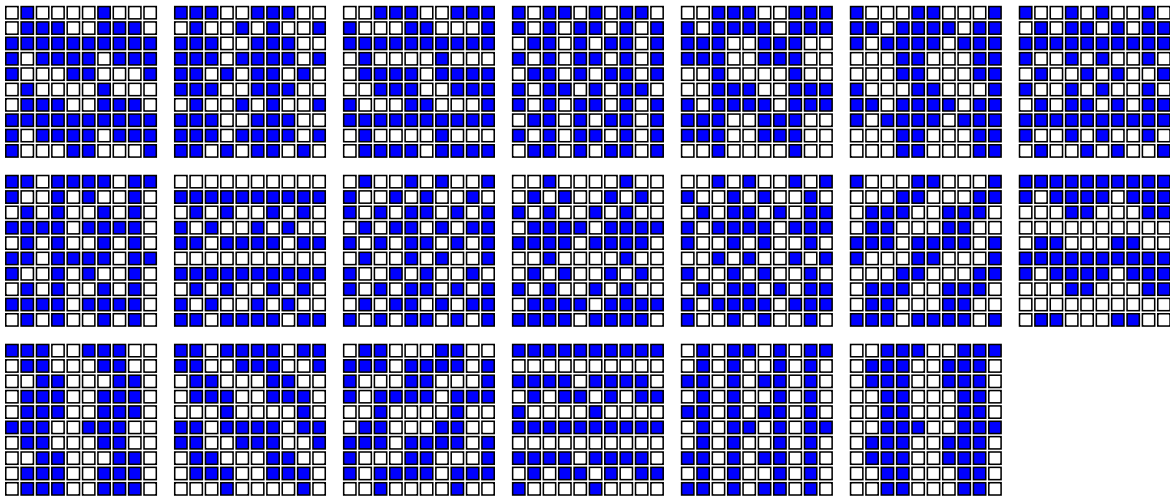

Figure 4.15: All Class I spin configurations which can be represented using a 5×5 basis on the 2D square lattice and are *not* left invariant under any combination of symmetry operations besides that which is guaranteed by the underlying 5×5 periodic boundary conditions, displayed left-to-right, top-to-bottom, in order of decreasing absolute magnetization $|\langle\sigma\rangle|$. There are 20 such configurations.

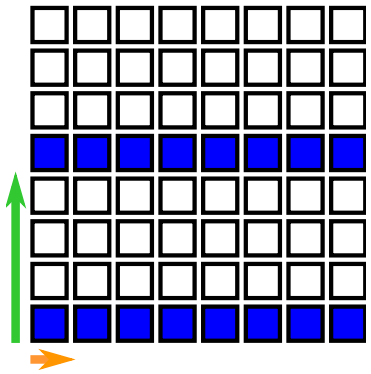

Figure 4.16: An example demonstrating how λ_2 is calculated for a periodic spin configuration. The arrows denote the two shortest non-collinear lattice vectors of the fundamental cell. Since the lengths of these two vectors are 1 and 4, $\lambda_2 = 4$ (the larger of the two lengths).

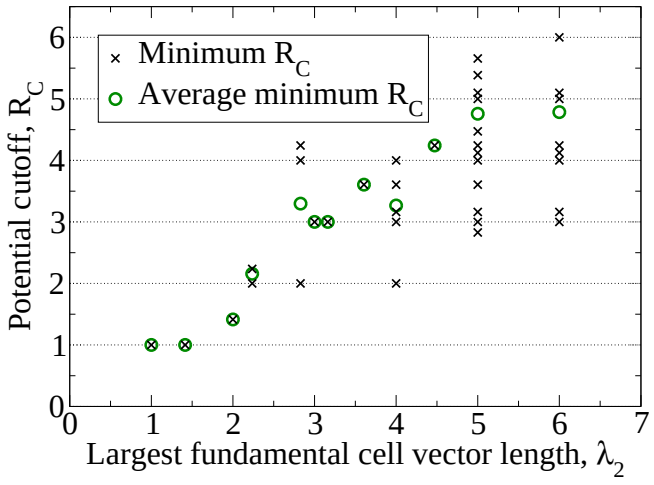

Figure 4.17: The minimal range R_C of the spin-spin interaction potential required to stabilizes spin configurations on the 2D square lattice in term of the length of the longer lattice vector λ_2 of their fundamental cells. The circles indicate the average R_C for all spin configurations with the same λ_2. It should be mentioned that not all configurations with $\lambda_2 \leq 6$ have been considered in this work. Therefore this figure should only be taken as a rough indicator of the range of R_C versus λ_2.

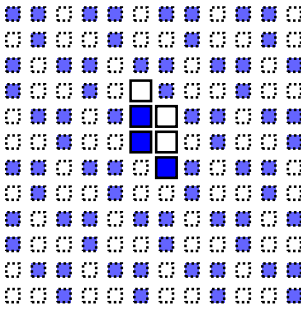

Figure 4.18: One of the two spin configurations with $\lambda_2 = \sqrt{8}$ which can be stabilized using a spin-spin interaction potential with a minimal cutoff $R_C = \sqrt{18}$. While this configuration is in Class I, the other configuration with $\lambda_2 = \sqrt{8}$ and $R_C = \sqrt{18}$ is in Class II due to being S_2-degenerate with two other spin configurations with larger fundamental cells. The spins in the fundamental cell are denoted using a solid outline, while other spins are denoted using a dashed outline and smaller squares. The fundamental cell lattice vectors are $(1, 2)$ and $(-2, 2)$.

square lattice has no such quantity. While $\sqrt{N_F}$ could be used, it cannot distinguishes elongated fundamental cells and square fundamental cells. Instead, we find the two shortest possible lattice vectors (with the second restricted to be non-collinear with the first), and use the length λ_2 of the larger of the two lattice vectors as a representative length of the fundamental cell. An example of how λ_2 is calculated is shown in Fig. 4.16. Figure 4.17 compares the λ_2 value of spin configurations with the minimal potential cutoff R_C required to stabilize these configurations on an underlying 2D square lattice. A major difference with the underlying 1D integer lattice is that there is no upper bound at $R_C = \lambda_2$. This is because the reasoning behind the upper bound of R_C for the 1D integer lattice case depended on $S_2(R)$ being equal to its maximal value when R is equal to the configuration period, which is not true in general for the 2D square lattice. There are even some spin configurations for which $S_2(R)$ never reaches its maximum (or minimum) value, such as most of those with a 5×5 basis. An example of a spin configuration with an unusually large R_C for its λ_2 value is shown in Fig. 4.18, and its corresponding spin-spin interaction potential is presented in Table 4.4. Despite these differences, both the 1D and 2D spin configurations show an increased required potential range as their fundamental cells grow larger, as expected.

Again, one benefit of enumerating all of the spin configurations (up to some size limit) that are ground states of some spin-spin interaction potential is that such an investigation allows us to discover the limits of what these radial interaction potentials can or cannot stabilize. One question is whether or not you can stabilize spin configurations in which the vast majority of the spins have a given orientation (but not all of them as in the case of the ferromagnetic spin configuration). This is equivalent to asking how close the magnetization per spin of a given spin configuration can be to 1, without actually being 1 (with the magnetization $\langle\sigma\rangle$ of a configuration defined as the averaged value of all the spin values σ_i). The only spin configuration with

Table 4.5: The number of (a) 4×5 and (b) 5×5 iso-S_2 sets in each class in term of the absolute magnetization $|\langle\sigma\rangle|$ of the set. It should be noted that all configurations in a given iso-S_2 set have the same magnetization up to a sign.

(a)

$\lvert\langle\sigma\rangle\rvert$	I	II	III
0.0	98	2	879
0.1	52	0	1321
0.2	82	0	1036
0.3	40	0	703
0.4	24	0	415
0.5	2	0	193
0.6	2	0	87
0.7	0	0	23
0.8	0	0	8
0.9	0	0	1
1.0	1	0	0

(b)

$\lvert\langle\sigma\rangle\rvert$	I	II	III
0.04	28	25	1737
0.12	16	4	1690
0.20	17	0	1415
0.28	4	0	1226
0.36	4	0	903
0.44	4	0	623
0.52	0	0	357
0.60	0	0	169
0.68	0	0	64
0.76	0	0	19
0.84	0	0	5
0.92	0	0	1
1.00	1	0	0

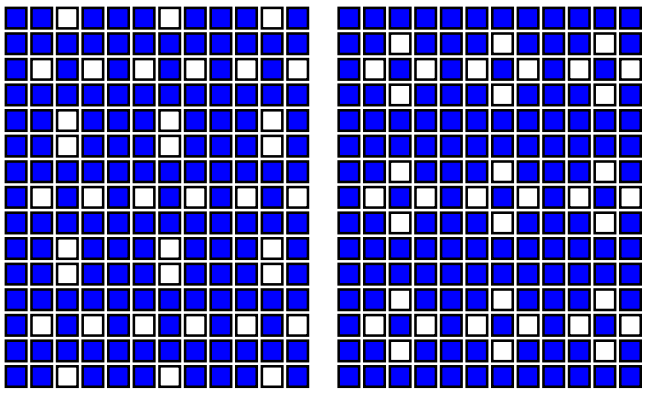

Figure 4.19: Spin configurations from the two Class I iso-S_2 sets with the highest absolute magnetization, $\langle\sigma\rangle = 0.6$, found by our exhaustive search (not considering the ferromagnetic state with $\langle\sigma\rangle = 1$). Both of these spin configurations can be realized using a 4×5 unit cell.

Table 4.6: The spin-spin interaction potentials $J(R)$ corresponding to the spin configurations shown in Fig. 4.19. The spin-spin correlation function $S_2(R)$, its maximum value on $\mathbb{Z}^2$, $S_2^{\max}(R)$, and the energy per spin ϵ of the ground states are also shown for comparison.

R	$J(R)$	$S_2(R)$	$J(R)$	$S_2(R)$	$S_2^{\max}(R)$
1	-0.108	3/5	-0.318	2/5	2
$\sqrt{2}$	-1	2/5	1	6/5	2
2	-0.201	4/5	-0.486	1	2
$\sqrt{5}$	-0.408	8/5	0.131	4/5	4
$\sqrt{8}$	-0.116	2/5	-0.556	2/5	2
3	-0.620	2/5	0.063	3/5	2
$\sqrt{10}$	0.540	8/5	0.369	8/5	4
$\sqrt{13}$	0.243	8/5	-0.126	4/5	4
4	0.705	7/5	0	6/5	2
$\sqrt{17}$	-0.075	6/5	0.122	8/5	4
$\sqrt{18}$	-0.060	6/5	-0.129	2/5	2
$\sqrt{20}$	-0.022	4/5	—	—	4
5	0.310	2	—	—	6
$\sqrt{26}$	0.204	4/5	—	—	4
$\sqrt{29}$	0.173	12/5	—	—	4
ϵ	-1.687		-1.140		

a magnetization of 1 is the Class I ferromagnetic spin configuration, where all spins have identical orientation. It should be mentioned that while some Class I striped phase and some Class II block checkerboard spin configurations previously studied in Ref. [1] can have a magnetization arbitrarily close to 1, such spin configurations would require very large unit cells. From Table 4.5, we observe that Class II sets are highly concentrated at low magnetization. This is a direct consequence of lower magnetization sets having higher degeneracies than higher magnetization sets. Figure 4.19 shows both $|\langle\sigma\rangle| = 0.6$ Class I sets, which are the two Class I sets with highest magnetization that we have found during the enumeration process. Table 4.6 contains the spin-spin interaction potentials which stabilize these high magnetizations sets.

4.4 Discussion and Conclusions

The primary goal of the research presented herein was to utilize recently developed inverse statistical-mechanical techniques to (i) enumerate the ground state spin configurations of the radial pairwise spin-spin interaction potential given in Eq. (4.1) and (ii) classify these spin configurations according to the solution class designations introduced in Ref. [1]. Governed only by computational feasibility, this study focused on spin configurations discretized on the underlying 1D integer and 2D square lattices. In particular, we have found that, with the exception of the smallest system sizes, the majority of target spin configurations can only be ground states with non-S_2-type degeneracies, *i.e.*, they belong to Class III iso-S_2 sets. This is in stark contrast to previous papers using inverse methods for point particles interacting according to pairwise radial interactions, which have reported successful uses of the methods to stabilize a wide variety of configurations such as the square, honeycomb, and Kagomé crystals in two dimensions [2, 7, 29], and the simple cubic, diamond, wurtzite, and calcium fluoride crystals in three dimensions [4, 30, 31, 32, 33], but have not reported any configurations which cannot be stabilized using the class of potentials under consideration. While stabilizing such structures is no easy feat, our results open questions about whether the reason why these configurations could be stabilized is simply a consequence of them being relatively simple structures (having only up to 4-particle bases) with a high degree of symmetry or order. Therefore, it would be of considerable interest to explore whether or not more complex point-particle configurations can be stabilized by a pairwise radial potential, *i.e.*, whether they would belong to Class I or III for such interactions. Additionally, it would be fascinating to see if Class II point-particle configurations exist. While the existence of degenerate point-particle configurations is already known (and any degenerate spin configurations can be converted into degenerate point-particle configurations), it is

likely that such configurations can be stable ground states of some pairwise radial potential, however they have yet to be discovered.

One interpretation as to why some spin configurations are in Class III instead of being in either Class I or II is that the Class III configurations are more "complex" or less "ordered" according to some metric. While we have not attempted to define any such metric, our results do not show any indication that would point toward the existence of such a metric beyond the number of spins in the fundamental cell. Configurations with smaller unit cells are indeed more likely to be in Class I or II than configurations with larger unit cells, a result that is consistent with our conjecture in Ref. [1] that the fraction of class I configurations goes to zero in the infinite-system limit. Furthermore, for a given system size, configurations with near-zero magnetization are more likely to be in Class I or II than configurations with higher magnetization (see Table 4.5). Besides these two observed trends, it does not seem that there is any other link between the complexity of a given spin configuration and its solution class. Indeed, there are many Class I configurations that are devoid of symmetry (besides the symmetry resulting from their periodic boundary conditions, see Fig. 4.15), while there are also many Class III configurations that are more symmetrical. Since Class I and II configurations can be mapped to the vertices of a k-dimensional polytope of all allowed values of $S_2(R)$ (c.f. Fig. 11 of Ref. [1]), where k is the number of coordination shells for the underlying lattice within the cutoff radius R_C, studying this polytope could lead to an understanding of why certain configurations can be stabilized while others cannot. Additionally, such a study could result in the discovery of a "complexity" or "order" metric which would be a better predictor of the solution class for a given spin configuration. Even if we have no such metric, it is remarkable that we have been able to discover sets of spin configurations which can be unique ground states with some degree of non-trivial degeneracies (i.e., they

belong to Class II), that are much simpler and more ordered than other well-known disordered degenerate spin configurations [34, 35, 36].

Taking advantage of the underlying lattice structure, we were able to determine the shortest range of possible potentials that still correspond to specific target spin configurations as corresponding ground states. For periodic solutions on the 1D integer lattice, the shortest potential cutoff R_C was shown to have an upper bound that is linear in terms of the fundamental cell size. On the other hand, our results are insufficient to conclude whether a lower bound on R_C depends linearly or logarithmically on the fundamental cell size. While periodic solutions on the 2D square lattice also show an increase in lower and upper bounds on R_C with increased λ_2, our data is still too sparse to make any conclusive predictions for larger systems.

The generalized Ising model has several interesting ties to two-phase reconstruction problems, which consist of attempting to recover a two-phase configuration (black and white pixels or voxels) with limited statistical information, such as the standard two-point correlation function [37, 38, 39, 40]. It was shown that even if one obtains a configuration with an identical two-point correlation function (analogous to the Class II solutions considered in this work), that configuration can be very different from the targeted configuration, as measured by other correlation functions. Additionally, using a correlation function that is analogous to $S_2(R)$, Gommes *et al.* [41] demonstrated that a target configuration can possess an enormous number of degeneracies (*e.g.*, $\sim 10^7$ degeneracies for a disordered 8×8 pattern), which likely grows exponentially with system size. While this number includes both trivial and non-trivial degeneracies, it still indicates that there is a huge number of non-trivial degeneracies. While that study did not distinguish between Class I, II, and III solutions, it would not be surprising if this increased number of degeneracies is also the case for Class I and II sets.

Given the limitations of achieving unique ground-state spin configurations with radial interactions of finite range, a natural extension of the present application of inverse statistical mechanical techniques is to examine more general spin interactions that would enable one to increase the relative size of the set of Class I solutions. One such possible generalization includes directional pairwise spin-spin interactions of finite range, which we expect will dramatically increase the number of possible Class I solutions due to the fact that the directional spin-spin correlation function in Eq. (4.8) more uniquely specifies a target configuration than a radial one [40]. Another way to achieve this goal would be to allow not only spin-spin interactions but intrinsic n-spin interactions ($n \geq 3$). It would be interesting to investigate the improvement provided by the simplest extension of this type, i.e., directional pairwise and triplet spin interactions.

In addition, it would be equally interesting to investigate spin configurations discretized on other underlying lattices, such as the 2D triangular and 3D cubic lattices. In particular, the 2D triangular lattice is known to have degenerate ground states for the nearest-neighbor antiferromagnetic potential [22]; therefore, we expect that this choice of underlying lattice could lead to qualitatively different results than those found in this work with the 2D square lattice.

Bibliography

[1] R. A. DiStasio Jr., É. Marcotte, R. Car, F. H. Stillinger, and S. Torquato, *Designer Spin Systems via Inverse Statistical Mechanics*, Phys. Rev. B (accepted).

[2] M. C. Rechtsman, F. H. Stillinger, and S. Torquato, *Optimized Interactions for Targeted Self-Assembly: Application to Honeycomb Lattice*, Phys. Rev. Lett. **95**, 228301 (2005); erratum: Phys. Rev. Lett. **97**, 239901 (2006).

[3] M. C. Rechtsman, F. H. Stillinger and S. Torquato, *Designed Interaction Potentials via Inverse Methods for Self-Assembly*, Phys. Rev. E **73**, 011406 (2006).

[4] M. C. Rechtsman, F. H. Stillinger, and S. Torquato, *Synthetic Diamond and Wurtzite Structures Self-Assemble with Isotropic Pair Interactions*, Phys. Rev. E **75**, 031403 (2007).

[5] S. Torquato, *Inverse Optimization Techniques for Targeted Self-Assembly*, Soft Matter **5**, 1157 (2009).

[6] H. Cohn and A. Kumar, *Algorithmic design of self-assembling structures*, Proc. Natl. Acad. Sci. USA **106**, 9570 (2009).

[7] É. Marcotte, F. H. Stillinger, and S. Torquato, *Optimized Monotonic Convex Pair Potentials Stabilize Low-Coordinated Crystals*, Soft Matter **7**, 2332 (2011).

[8] E. Ising, *A contribution to the theory of ferromagnetism*, Z. Phys. **31**, 253 (1925).

[9] B. M. McCoy and T. T. Wu, *The Two-Dimensional Ising Model* (Harvard University Press, Cambridge, 1973).

[10] L. Onsager, *Crystal Statistics. I. A Two-Dimensional Model with an Order-Disorder Transition*, Phys. Rev. **65**, 117 (1944).

[11] C. N. Yang, *The Spontaneous Magnetization of a Two-Dimensional Ising Model*, Phys. Rev. **85**, 808 (1952).

[12] K. Barros, P. L. Krapivsky, and S. Redner, *Freezing into stripe states in two-dimensional ferromagnets and crossing probabilities in critical percolation*, Phys. Rev. E **80**, 040101 (2009).

[13] A. J. F. Siegert and David J. Vezzetti, *On the Ising Model with LongRange Interaction*, J. Math. Phys. **9**, 2173 (1968).

[14] R. J. Elliott, *Phenomenological Discussion of Magnetic Ordering in the Heavy Rare-Earth Metals*, Phys. Rev. **124**, 346 (1961).

[15] M. E. Fisher and W. Selke, *Infinitely Many Commensurate Phases in a Simple Ising Model*, Phys. Rev. Lett. **44**, 1502 (1980).

[16] R. J. Baxter, *Exactly Solved Models in Statistical Mechanics* (Academic Press, London, 1982).

[17] A. Giuliani, J. L. Lebowitz, and E. H. Lieb, *Ising models with long-range antiferromagnetic and short-range ferromagnetic interactions*, Phys. Rev. B **74**, 064420 (2006)

[18] A. Giuliani, J. L. Lebowitz, and E. H. Lieb, *Striped phases in two-dimensional dipole systems*, Phys. Rev. B **76**, 184426 (2007)

[19] A. Giuliani, J. L. Lebowitz, and E. H. Lieb, *Checkerboards, stripes, and corner energies in spin models with competing interactions*, Phys. Rev. B **84**, 064205 (2011).

[20] In the summation in Eq. (4.1), the index i runs over the N spins contained in the unit cell, while the index j runs over spins contained in the unit cell as well as its periodic images.

[21] A generalized Kronecker delta is defined as

$$\delta_{\alpha,\beta} \equiv \begin{cases} 1, & \text{if } \alpha = \beta, \\ 0, & \text{if } \alpha \neq \beta, \end{cases} \tag{4.10}$$

where α and β are either distances or vectors.

[22] G. H. Wannier, *Antiferromagnetism. The Triangular Ising Net*, Phys. Rev. **79**, 357 (1950).

[23] K. Kano, and S. Naya, *Antiferromagnetism. The Kagomé Ising Net*, Prog. Theor. Phys. **10**, 158 (1953).

[24] J. Oitmaa, *The square-lattice Ising model with first and second neighbour interactions*, J. Phys. A: Math. Gen. **14**, 1159 (1981).

[25] J. Oitmaa, *The triangular lattice Ising model with first and second neighbour interactions*, J. Phys. A: Math. Gen. **15**, 573 (1982).

[26] R. Rietman, B. Nienhuis, and J. Oitmaa, *The Ising model on hyperlattices*, J. Phys. A: Math. Gen. **25**, 6577 (1992).

[27] C. C. Wu, *Ising models on hyperbolic graphs*, J. Stat. Phys. **85**, 251 (1996).

[28] C.-K. Hu and N. S. Izmailian, *Exact correlation functions of Bethe lattice spin models in external magnetic fields*, Phys. Rev. E **58**, 1644 (1998).

[29] E. Edlund, O. Lindgren, and M. N. Jacobi, *Designing Isotropic Interactions for Self-Assembly of Complex Lattices*, Phys. Rev. Lett. **107**, 085503 (2011).

[30] M. C. Rechtsman, F. H. Stillinger and S. Torquato, *Self-Assembly of the Simple Cubic Lattice via an Isotropic Potential*, Phys. Rev. E **74**, 021404 (2006).

[31] É. Marcotte, F. H. Stillinger, and S. Torquato, *Designed Diamond Ground State via Optimized Isotropic Monotonic Pair Potentials*, J. Chem. Phys. **138**, 061101 (2013).

[32] A. Jain, J. R. Errington, and T. M. Truskett, *Inverse design of simple pairwise interactions with low-coordinated 3D lattice ground states*, Soft Matter **9**, 3866 (2013).

[33] G. Zhang, F. H. Stillinger, and S. Torquato, *Inverse Statistical Mechanics: Probing the Limitations of Isotropic Pair Potentials to Produce Ground-State Structural Extremes*, in preparation.

[34] J. Snyder, J. S. Slusky, R. J. Cava, and P. Schiffer, *How 'spin ice' freezes*, Nature **413**, 48 (2001).

[35] S. V. Isakov, R. Moessner, and S. L. Sondhi, *Why Spin Ice Obeys the Ice Rules*, Phys. Rev. Lett. **95**, 217201 (2005).

[36] C. L. Henley, *The "Coulomb Phase" in Frustrated Systems*, Annu. Rev. Condens. Matter Phys. **1**, 179 (2010).

[37] C. L. Y. Yeong and S. Torquato, *Reconstructing Random Media*, Phys. Rev. E **57**, 495 (1998).

[38] M. S. Talukdar, O. Torsaeter, and M. A. Ioannidis, *Stochastic Reconstruction of Particulate Media from Two-Dimensional Images*, J. Colloid Interface Sci. **248**, 419 (2002).

[39] M. E. Kainourgiakis, E. S. Kikkinides, A. Galani, G. C. Charalambopoulou, and A. K. Stubos, *Digitally Reconstructed Porous Media: Transport and Sorption Properties*, Transport Porous Med. **58**, 43 (2005).

[40] Y. Jiao, F. H. Stillinger, and S. Torquato, *Geometrical Ambiguity of Pair Statistics. II. Heterogeneous Media*, Physical Review E **82**, 011106 (2010).

[41] C. J. Gommes, Y. Jiao, and S. Torquato, *Microstructural Degeneracy Associated with a Two-Point Correlation Function and its Information Content*, Physical Review E **85**, 051140 (2012).

Chapter 5

Efficient Linear Programming Algorithm to Generate the Densest Lattice Sphere Packings

5.1 Introduction

There has been great interest in understanding the packings of hard (*i.e.* nonoverlapping) particles because they serve as useful models for a variety of many-particle systems arising in the physical and biological systems, such as liquids [1, 2], glasses [3, 4, 5], crystals [6, 7, 8], granular media [9, 10, 11, 12], and living cells [13]. One outstanding problem is to find the densest packing of identical spheres in d-dimensional Euclidean space $\mathbb{R}^d$. This seemingly simple problem has proved to be a challenge for all but the most simple systems; it was not until 2005 that a proof was successfully presented to confirm the centuries-old Kepler conjecture [14], which states that the densest packing of spheres in three dimensions is the face-centered cubic lattice. For $d \geq 4$, there are no proofs for the densest sphere packings, although for $d = 8$ and $d = 24$ they are almost surely the E_8 and Leech lattices, respectively [15]. Inter-

estingly, these two lattices have also been used to construct 10- and 26-dimensional string theories, respectively [16, 17].

In recent years, high-dimensional dense sphere packings have attracted the attention of physicists because of the insights they offer about condensed-phase systems in lower dimensions [5, 12, 18, 19, 20]. It is noteworthy that the general problem of finding the densest sphere packings in $\mathbb{R}^d$ (and other spaces) is directly relevant to making data transmission over communication channels resistant to noise [21, 22] and of intense interest in discrete geometry and number theory [22, 23]. The densest sphere packing problem is also deeply linked to the covering, quantizer, number variance, and kissing number problems, with which it shares the best known solutions in a variety of dimensions [22, 24, 25]. Clever analytical methods have been used to discover dense packings in high dimensions (*i.e.*, $d \geq 4$) but this approach becomes less efficient as d increases, especially because lessons learned in lower dimensions cannot be used to construct packings in higher dimensions [22, 26].

Numerical methods have only recently emerged to discover the densest packings in high-dimensional spaces. One such method devised by Kallus, Elser, and Gravel [19], is based on the "divide and concur" framework in which a dense arrangement of overlapping spheres is gradually relaxed until none of the spheres overlap. Another method formulated by Andreanov and Scardicchio [20] takes advantage of the fact that all densest lattice packings are also *perfect lattices* (defined precisely in Sec. 5.4), which are finite in number [22]. The densest lattice packings can therefore be obtained by randomly exploring the space of perfect lattices. The efficiency of both algorithms plummets as d grows larger, preventing them from being effectively used in very high dimensions [27].

In the past twenty years, the Lubachevsky-Stillinger (LS) algorithm [28] has served as a standard for generating dense packing of various shaped hard particles in two and three dimensions [29, 30, 31]. However, since the LS algorithm is based on a

particle-growth molecular dynamics simulation, it is extremely computationally costly to use it to generate jammed dense packings with high numerical accuracy, especially as d grows beyond three dimensions. A recent improvement on the LS algorithm is the Torquato-Jiao (TJ) algorithm [32], which replaces the molecular dynamics with an optimization problem that is solved using sequential linear programming. In particular, the density ϕ of a sphere packing (fraction of space covered by the spheres) within an adaptive fundamental cell subject to periodic boundary conditions is maximized. The design variables are the sphere positions (subject to nonoverlap), and the shape and size of the fundamental cell. The linear programming solution of this optimization problem becomes exact as the packing approaches the *jamming point* [12]. The TJ algorithm has been found to be a very powerful packing protocol to generate both maximally-dense packings (global maxima) and disordered jammed packings (local maxima) with a large number of identical spheres (per fundamental cell) across space dimensions [12] as well as maximally dense binary sphere packings [33, 34].

In this chapter, we specialize the TJ algorithm to the restricted problem of finding the densest *lattice* sphere packings in high dimensions. In a lattice packing, there is only one sphere per fundamental cell [35]. Even this limited problem for $d \geq 4$ brings considerable challenges; its solution has been proven only for $d \leq 8$ [49] and $d = 24$ [15], and it is closely related to the shortest-vector problem, which is of NP-hard complexity [36]. Additionally, most of the densest known sphere packings for $d \leq 48$ are lattice packings [22, 26]. Tackling the lattice problem is thus a necessary first step prior to attempting to solve the much more complicated general problem of finding the densest periodic packings. A *periodic* packing of congruent particles is obtained by placing a fixed configuration of N particles where $N > 1$ with in one fundamental cell of a lattice, which is then periodically replicated without overlaps.

The outline of the rest of the chapter is as follows: Sec. 5.2 describes the implementation of the TJ algorithm for the special case of lattice sphere packings. In Sec. 5.3 we motivate the choices that we make for the initial conditions and relevant parameters in order the various problems across dimensions. In Sec. 5.4, we apply the TJ algorithm for $2 \leq d \leq 19$, and show that it is able to rapidly and reliably discover the densest known lattice packings without *a priori* knowledge of their existence. The TJ algorithm is found to be appreciably faster than previously published algorithms [19, 20]. We also demonstrate that the suboptimal-lattice solutions (i.e., the local maxima "inherent structures") are particularly interesting because they reveal features of the "density" landscape. In Sec. 5.5, we close with some concluding remarks and a discussion about possible improvements and other applications of the TJ algorithm.

5.2 Application of the TJ algorithm to finding the densest lattice sphere packings

The basic principle behind the TJ algorithm [32] resides in the fact that finding the densest sphere packing can be posed as an optimization problem with a large number of nonlinear constraints (such as nonoverlap conditions between pairs of particles) which can be solved by solving a series of linear approximations of the original problem. Its solution eventually converges toward a local or global optimum. While global optimality cannot be guaranteed, it has been shown that the TJ algorithm frequently reaches the globally densest packings [32]. The TJ algorithm was formulated for the general problem of finding dense periodic sphere packings. Here we describe its implementation for the special case of determining the densest lattice sphere packings, which reduces the problem to optimizing the shape and size of the fundamental cell, since no sphere translations are involved. It is interesting to note that the TJ algo-

rithm can be viewed as a hard-core analog of a gradient descent in the space of lattices for energy minimizations for systems of particles interacting with soft potentials as described by Cohn, Kumar, and Schürmann [38].

Before explaining the numerical details of the TJ algorithm, we need to define some mathematical quantities. A d-dimensional lattice Λ is composed of all vectors that are integer linear combinations of a set of d basis vectors $\mathbf{m}_1$, ..., $\mathbf{m}_d$,

$$\mathbf{P} = n_1\mathbf{m}_1 + n_2\mathbf{m}_2 + \cdots + n_d\mathbf{m}_d, \tag{5.1}$$

where n_j are the integers ($j = 1, 2, \ldots, d$) and we denote by $\mathbf{n}$ the corresponding column vector with such components. Using the generator matrix $\mathbf{M}_\Lambda$, whose columns are the basis vectors, allows us to explicitly write the lattice set:

$$\Lambda = \left\{\mathbf{M}_\Lambda \mathbf{n} : \mathbf{n} \in \mathbb{Z}^d\right\}. \tag{5.2}$$

One useful property of $\mathbf{M}_\Lambda$ is that its determinant is equal (up to a sign) to the volume of the lattice fundamental cell. We can then write the lattice packing density ϕ as the ratio of the volume occupied by spheres of diameter D to the volume of the fundamental cell:

$$\phi(\Lambda) = \frac{v(D/2)}{|\det \mathbf{M}_\Lambda|}, \tag{5.3}$$

where

$$v(R) = \frac{\pi^{d/2} R^d}{\Gamma(1 + d/2)} \tag{5.4}$$

is the d-dimensional volume of a sphere of radius R and $\Gamma(n)$ is the Euler gamma function.

The problem of finding the densest lattice packing of spheres in d dimensions can be expressed as: *Find the $d \times d$ generator matrix $\mathbf{M}_\Lambda$ with minimal determinant*

$|\det \mathbf{M}_\Lambda|$, *under the constraint that all non-zero lattice vectors* $\mathbf{M}_\Lambda \mathbf{n}$, $\mathbf{n} \in \mathbb{Z}^d \setminus \{\mathbf{0}\}$, *are at least as long as* D.

For this problem, the Torquato-Jiao algorithm consists of the following four steps:

1. Randomly create a generator matrix $\mathbf{M}_\Lambda$ according to some stochastic process.
2. For a given *influence sphere radius* $R_I > D$, find all of the non-zero lattice vectors it contains, *i.e.*, compute $\left\{\mathbf{v} = \mathbf{M}_\Lambda \mathbf{n} : \mathbf{n} \in \mathbb{Z}^d \setminus \{\mathbf{0}\} \wedge |\mathbf{v}| \leq R_I\right\}$.
3. Solve a linearized version of a problem, for which the objective is to maximize ϕ (equivalent to minimizing $|\det \mathbf{M}_\Lambda|$) and the constraints are that none of the vectors calculated in step 2 become shorter than D.
4. Consider whether the algorithm has converged to a lattice that is a stable maximum in ϕ (either the densest lattice packing or a local maximum *inherent structure* [37]). If it is the former, repeat the procedure starting from step 2. If it is the latter, the solution has converged to a local or global optimum and the procedure is terminated.

In what follows, we provide a more detailed explanation of these four steps.

5.2.1 Initialization

There are many possible methods to initialize the generator matrix $\mathbf{M}_\Lambda$. Any candidate procedure must both satisfy the minimal length constraint and adequately sample the space of all lattices. The former is trivially satisfied by rescaling the matrix if the minimal length constraint is violated. In order to satisfy the latter condition, we mainly use Gaussian initial lattices, in which each coefficient of their generator matrix $\mathbf{M}_\Lambda$ is an independent normal variable $N(0, \sigma^2)$ with a variance σ^2. These matrices have the property that each of their lattice vectors (columns of $\mathbf{M}_\Lambda$) have independent orientations with no given preference for any particular direction. To compare this against a different initialization method, we also consider initial lattices for which $\mathbf{M}_\Lambda$ is the sum of the generator matrix of a specific lattice packing

(such as the d-dimensional checkerboard lattice D_d or the hypercubic lattice Z_d, see Appendix 5.A for the definitions of these lattices) and one of a Gaussian initial lattice.

5.2.2 Finding short vectors

Finding all of the vectors for an arbitrary lattice that are within a small given radius R_I from the origin is a complex problem in high dimensions. Indeed, the problem of finding the *shortest lattice vector* for a given lattice Λ grows superexponentially with d and is in the class of NP-hard (nondeterministic polynomial-time hard) problems [36]. One efficient method to solve this problem can be found in Ref. [39]. The influence sphere radius R_I can be any value larger than the sphere diameter D, and may vary from one iteration to the next. It is found that the algorithm is largely insensitive to the value chosen for R_I, which is to be contrasted to the results for periodic packings, where larger R_I values favor the densest packings over inherent structures [32]. Since the computational cost of this and the following steps quickly increases with R_I, we opt to use the nearly minimal value $R_I = 1.1D$.

5.2.3 Solving the linearized problem

The only linearized problem variables in the case of the implementation of the TJ algorithm in the case of a lattice packing are the coefficients of the $d \times d$ symmetric strain tensor $\boldsymbol{\varepsilon}$ [40]. The modified generator matrix is then

$$\mathbf{M}_\Lambda \rightarrow \mathbf{M}_\Lambda + \boldsymbol{\varepsilon}\mathbf{M}_\Lambda. \tag{5.5}$$

The constraint that a vector originally at position $\mathbf{v} = \mathbf{M}_\Lambda \mathbf{n}$ remains at least as large as D can then be written as

$$\begin{aligned} \mathbf{n}^\top \mathbf{M}_\Lambda^\top \mathbf{M}_\Lambda \mathbf{n} + 2\mathbf{n}^\top \mathbf{M}_\Lambda^\top \boldsymbol{\varepsilon} \mathbf{M}_\Lambda \mathbf{n} + \mathbf{n}^\top \mathbf{M}_\Lambda^\top \boldsymbol{\varepsilon}^\top \boldsymbol{\varepsilon} \mathbf{M}_\Lambda \mathbf{n} &\geq D^2, \\ \mathbf{v}^\top \mathbf{v} + 2\mathbf{v}^\top \boldsymbol{\varepsilon} \mathbf{v} + \mathbf{v}^\top \boldsymbol{\varepsilon}^\top \boldsymbol{\varepsilon} \mathbf{v} &\geq D^2. \end{aligned} \tag{5.6}$$

This constraint is linearized by dropping the term that is quadratic in $\boldsymbol{\varepsilon}$:

$$2\mathbf{v}^\top \boldsymbol{\varepsilon} \mathbf{v} \geq D^2 - \mathbf{v}^\top \mathbf{v}. \tag{5.7}$$

It should be noted that the term $(\mathbf{v}^\top \boldsymbol{\varepsilon}^\top \boldsymbol{\varepsilon} \mathbf{v})$ that has been dropped is non-negative, which means that every set of variables that satisfies inequality (5.7) also satisfies inequality (5.6). This is different from the equivalent constraints for periodic packings, for which the quadratic term may be negative due to the interaction between the lattice deformation and the particle displacements. This avoids the necessity of either adding a constant term to the constraint or rescaling the system if spheres are found to overlap, which is the case for the general periodic packing problem [32].

Additionally, extra constraints must be added to prevent vectors that could be outside the influence sphere from becoming shorter than D:

$$\begin{aligned} 2\mathbf{v}^\top \boldsymbol{\varepsilon} \mathbf{v} &\geq D^2 - R_I^2 \\ \frac{\mathbf{v}^\top \boldsymbol{\varepsilon} \mathbf{v}}{\mathbf{v}^\top \mathbf{v}} &\geq \frac{D^2/R_I^2 - 1}{2} \equiv -\lambda, \end{aligned} \tag{5.8}$$

where the length of the vector has been chosen as its smallest possible value (R_I). A simple yet robust method to ensure that inequality (5.8) is satisfied for all vectors outside of the influence sphere is to bound the lowest eigenvalue of $\boldsymbol{\varepsilon}$ from below by $-\lambda$. There are multiple ways to write linear constraints on $\boldsymbol{\varepsilon}$ such that its eigenvalues

are all larger than $-\lambda$. One such way is given by

$$-\frac{\lambda}{2} \leq \text{Diagonal element of } \boldsymbol{\varepsilon} < \infty, \tag{5.9}$$

$$-\frac{\lambda}{2(d-1)} \leq \text{Off-diagonal element of } \boldsymbol{\varepsilon} \leq \frac{\lambda}{2(d-1)}. \tag{5.10}$$

Finally, the determinant of the modified generator matrix (assuming that $\det \mathbf{M}_\Lambda > 0$) is

$$\det \mathbf{M}_\Lambda \det (\mathbf{I} + \boldsymbol{\varepsilon}) = \det \mathbf{M}_\Lambda \left(1 + \operatorname{tr} \boldsymbol{\varepsilon} + O(\boldsymbol{\varepsilon}^2)\right), \tag{5.11}$$

where $\mathbf{I}$ is the d-dimensional identity matrix. The linearized density ϕ is thus

$$\phi \simeq \phi_0 \left[1 - \operatorname{tr} \boldsymbol{\varepsilon}\right], \tag{5.12}$$

where ϕ_0 is the density for the initial generator matrix $\mathbf{M}_\Lambda$ and we used the fact that the density is inversely proportional to the fundamental cell volume. We can see from the above relation that maximizing the lattice density is equivalent to minimizing the trace of the strain tensor $\boldsymbol{\varepsilon}$. Unlike the linearized constraints (5.7), (5.9) and (5.10), which are conservative in that as long as they are satisfied the nonlinearized constraints will always be satisfied, the objective function (5.12) may have the wrong sign due to the nonlinear term having an unknown sign. In the situation where the updated lattice has a larger determinant than the original matrix, we halve $\boldsymbol{\varepsilon}$ (multiple times if necessary) to ensure a lower updated determinant. This prevents the algorithm from oscillating between multiple lattices and forces it to eventually converge.

5.2.4 Convergence criterion

The algorithm is considered to have converged if the sum of the squared coefficients of $\boldsymbol{\varepsilon}$ is below a small threshold value (10^{-12} for this chapter). This is numerically

equivalent to saying that all lattices in the neighborhood of the current lattice are less dense. This resulting lattice is therefore a local density maximum ("inherent structure" or "extreme" lattice, as elaborated in Sec. 5.4.2). Such a lattice is also *strictly jammed*, since any possible deformation requires an increase in the volume of its fundamental cell [11, 41, 42].

5.3 Study of parameters and initial conditions

The ability of TJ algorithm to discover the densest lattice packings can potentially be affected by the influence sphere radius R_I, the lowest eigenvalue of the strain matrix λ, and by the choice of the initial lattice. This section is dedicated to the study of their impact on the algorithm and to explain our choices for them in the following sections.

The TJ algorithm is deterministic [43], and therefore the initial lattice fully controls the resulting final lattice for given parameters R_I and λ. For example, employing initial lattices that are very close to the known densest lattice, not surprisingly, results in a very high success rate in obtaining that lattice. On the flip side, it would almost certainly never be able to discover a hypothetical denser lattice. It would therefore be misguided to use configurations that are near the known densest lattice as the initial conditions. However, allowing initial lattices that are very bad packers could result in a low success rate or a large convergence time for success. Thus, good choices for initial lattices involve a delicate balance between their diversity and an ability to relax quickly to dense lattices.

Table 5.1 shows numerical results in 13 dimensions. The initial lattices are taken from four different distributions, using six different influence sphere radii. The TJ algorithm typically succeeds at generating the densest known lattice packing with a high probability. However, it has a relatively lower success rates for the cases

Table 5.1: Frequency at which the densest known lattice packing in 13 dimensions, the K_{13} lattice [22, 26], is obtained for various parameters using the TJ algorithm. For all sets of influence sphere radii and initial conditions, 10000 lattice packings have been generated, excepted for $R_I = 2.0$ where only 3000 packings were generated. The calculations were performed on a single thread on a 2.40 GHz processor using the Gurobi linear programming library [44]. Since the run time strongly depends on the computer running the program and how well the code is optimized, it should only be used as a rough indication of the program efficiency.

Sphere of influence radius	Initial conditions	Success rate (%)	Average time per trial (sec)
$R_I = 1.1D$	Gaussian	8.61	5.0
$R_I = 1.1D$	D_{13} + noise	8.21	5.5
$R_I = 1.1D$	$\mathbb{Z}^{13}$ + noise	8.58	5.2
$R_I = 1.1D$	Invariant distribution	8.08	29.2
$R_I = 1.02D$	Gaussian	8.53	12.0
$R_I = 1.5D$	Gaussian	7.61	69.9
$R_I = 2.0D$	Gaussian	6.87	1938.5
variable R_I, ~ 200 constraints	Gaussian	7.97	6.3
variable R_I, ~ 2000 constraints	Gaussian	7.95	17.6
variable R_I, ~ 2000 constraints, reduced λ	Gaussian	8.58	108.7

$d = 13$ and $d \geq 17$. We thus purposely choose the 13-dimensional case to probe the best choices for the initial conditions and algorithmic parameters because of its abnormally low success rate in comparison to cases $d \leq 16$. Its low success rate results in better sensitivity to algorithm parameters compared with dimensions that have naturally higher success rates. Similar parameter dependence has been observed for other dimensions.

The *Gaussian* initial condition, as previously explained in Sec. 5.2.1, selects each coefficient of $\mathbf{M}_\Lambda$ from independent normal distributions with variances $\sigma^2 = D^2$. The initial conditions referred to as D_d + noise and $\mathbb{Z}^d$ + noise starts with the generator matrices for the checkerboard D_d and hypercubic $\mathbb{Z}^d$ lattices (these lattices are defined in Appendix 5.A), respectively, with nearest-neighbor distance equal to D plus some noise. Specifically, we add normal noise to each coefficient of $\mathbf{M}_\Lambda$ with a variance $\sigma^2 = D^2/100$. The final initial condition type that we attempt to employ, which we call an

invariant distribution, generates the lattice from an approximation of the invariant lattice distribution, using the algorithm described in Ref. [45] with $p = 10007$. For all of these initial conditions, the nearest neighbor distance is calculated and the lattice is rescaled to avoid any sphere overlap.

As can be seen in Table 5.1, the different initial conditions that we have used result in similar success rates. We therefore use the Gaussian initial condition to generate the initial lattices for all subsequent calculations, since it lacks both the potential bias that the D_d + noise and $\mathbb{Z}^d$ + noise initial conditions share, and it does converge much faster than the invariant distribution.

The main parameter influencing the efficiency of the TJ algorithm is the influence sphere radius R_I, which can either be fixed or vary from one iteration to the next. A radius that is too large leads to a large number of extra constraints for the linear program, greatly increasing its complexity. By contrast, if R_I is too close to D, then the constraints on the shear matrix $\boldsymbol{\varepsilon}$ will be too restrictive [see Eqs. (5.8), (5.9) and (5.10)]. This, in turn, only allows the lattice to deform very slowly, thereby requiring many iterations before convergence. A compromise between both is to use a variable R_I, such that the number of vectors inside the sphere of influence stays relatively constant, thus initially allowing a fast convergence when ϕ is small, without needing numerous constraints when ϕ gets close to its maximum. We use the following rough approximation to select R_I:

$$\text{Number of constraints} \sim \frac{1}{2}\frac{v(R_I)}{|\det \mathbf{M}_\Lambda|}, \tag{5.13}$$

where the factor of one-half comes from the observation that for every vector $\mathbf{v}$ in a lattice, there is another one of identical length $-\mathbf{v}$ which does not need to be explicitly constrained. A final parameter that can be modified is how much the lattice is allowed to deform at every iteration. As a test case, we divide the value of λ by 10 to check

whether an increased value of R_I provides benefits other than allowing larger strain matrices.

From Table 5.1, we can see that increasing R_I does not increase the success rate (it actually negatively affects it), while it significantly increases the run time. Therefore, the following calculations will be done using a small influence sphere radius of $R_I = 1.1D$. We attempted to adjust R_I as a function of dimension d to improve success rates for large d, but this proved to be fruitless. The radius R_I only weakly impacts the success rate, but its value has a dramatic influence on the time per trial, which gets multiplied by 400 when R_I is increased from $1.1D$ to $2.0D$. Therefore, one should decide on a choice of R_I so as to prioritize a faster execution speed over an increased probability of reaching the densest lattice packing.

5.4 Results

Here we describe the results we obtain by applying the TJ algorithm to find the densest lattice packings in dimensions 2 through 19. We compare our results with those obtained in previous investigations [19, 20]. We also provide the frequency of time that the TJ algorithm finds local versus the densest known global maxima.

5.4.1 Finding the densest lattice packings

We have applied the TJ algorithm for dimensions $d = 2$ through $d = 19$, and found the densest currently known lattice packing for each of them. The algorithm is robust in that it converges rapidly to the optimal solutions in most dimensions. Not surprisingly, except for the trivial $d = 2$ and $d = 3$ cases, it does not reach the optimal solution for all initial conditions. Therefore, even though the probabilities of finding the densest packing on the first attempt was high (greater than 19% for $d \leq 12$ and $14 \leq d \leq 16$), we typically needed multiple trials (i.e., different random initial condi-

Table 5.2: Frequency at which the densest known lattice packing is obtained using the TJ algorithm for $d = 2$ through $d = 19$ together with the lattices packing fraction ϕ and kissing number Z. The number of lattice packings generated is 10000 for $d \leq 18$ and 100000 for $d = 19$. The influence sphere radius $R_I = 1.1D$ and the initial lattices are generated using the Gaussian initial condition. See Appendix 5.A for the definitions of the various lattices. The comments in Table 5.1 concerning computational times also apply here.

d	Densest lattice packing	ϕ	Z	Success rate (%)	Time per trial (sec)	Time per successful trial (sec)
2	A_2	0.9069	6	100	1.7×10^{-5}	1.7×10^{-5}
3	D_3	0.7405	12	100	8.0×10^{-5}	8.0×10^{-5}
4	D_4	0.6169	24	74.31	5.6×10^{-4}	7.5×10^{-4}
5	D_5	0.4653	40	97.41	8.0×10^{-3}	8.2×10^{-3}
6	E_6	0.3729	72	89.72	0.019	0.022
7	E_7	0.2953	126	91.91	0.046	0.050
8	E_8	0.2537	240	84.16	0.33	0.40
9	Λ_9	0.1458	272	43.82	0.21	0.49
10	Λ_{10}	0.09202	336	22.74	0.49	2.1
11	K_{11}	0.06043	432	19.39	1.1	5.7
12	K_{12}	0.04945	756	33.30	2.7	8.2
13	K_{13}	0.02921	918	8.61	5.0	58
14	Λ_{14}	0.02162	1422	20.69	10	51
15	Λ_{15}	0.01686	2340	23.78	16	65
16	Λ_{16}	0.01471	4320	22.50	51	227
17	Λ_{17}	0.008811	5346	1.65	55	3.4×10^3
18	Λ_{18}	0.005928	7398	0.10	79	7.9×10^4
19	Λ_{19}	0.004121	10668	0.009	162	1.8×10^6

tions) to guarantee that the densest lattice packings were among these. Consequently, the quality of such a global optimization algorithm is preferably measured using the time required per successful trial instead of simply the time per trial or the success rate. Table 5.2 describes the rate at which the TJ algorithm produced the densest known lattice packings for dimensions $d = 2$ through $d = 19$ and the average time required per successful trial. We determine whether we achieved the densest known packings primarily by comparing the packing density ϕ and the kissing number Z (the number of spheres that are in contact with any given sphere) with published data [22, 26]. Additionally, we calculate theta series (the generating functions for the

number of vectors with specific lengths in the lattices [22]) up through the first few coordination shells.

The time required by the TJ algorithm to generate the densest known lattice packings is appreciably smaller than the times reported in Ref. [19]: approximately 4000 and 25000 seconds per successful packing for $d = 13$ and $d = 14$, respectively. The times required by the TJ algorithm of 58 and 51 seconds are orders of magnitude lower, indicating a genuine algorithmic improvement that cannot be attributed to the type of computer employed nor to implementation details.

The authors in Ref. [20] do not state precise run times for all dimensions, but report that, after generating more than 10^5 lattices, their algorithm is unable to discover the densest known lattices for $d = 14$ through $d = 19$. Since generating 10^5 lattices using their algorithm takes at least several hours, the TJ algorithm's ability to successfully generate the densest lattice packings in minutes for $d \leq 16$ is a tremendous speed-up improvement. Using more computing power, the authors in Ref. [20] are able to reliably obtain the densest known lattice for $d \leq 17$ using their algorithm [46]. For example, their calculations took four days ($\sim 3 \times 10^5$ seconds) for $d = 14$, which is three to four orders of magnitude longer than our own calculations (see Table 5.2).

The fact that the TJ algorithm was unable to find any denser lattice packings than the densest known lattice packings reinforces the evidence that these are indeed the densest lattice packings for $d = 2$ through $d = 19$. Although this evidence is not as strong for $d = 18$ and $d = 19$, due to the rare occurrences of the densest lattice packings, the evidence is quite strong for $d \leq 17$.

One particular aspect of the success rates shown in Table 5.2 is that they do not decrease monotonically with increasing dimension. Dimensions that are notably difficult are $d = 4$ and $d = 13$, and neither case can be explained by lattice packings with unusual properties, since $d = 5$ and $d = 12$, respectively, share similar packings,

but not the relatively low success rates. We will attempt to explain this phenomenon, along with the sharp decrease in success rates at $d = 17$, in the following section.

5.4.2 Inherent structures

The TJ algorithm is intrinsically a local density maximization algorithm. As such, it can, and often does, converge locally to the densest lattice packing associated with a given initial configuration, i.e., an *inherent structure* [32], that are not necessarily the global maxima. These local maxima are analogous to the inherent structures of a continuous potential. The study of these inherent structures are of fundamental interest in their own right because they offer insight about the nature of topography of the "density" landscape and understanding the frequency of their occurrence could potentially lead to improvements on the algorithm.

One interesting property of the density landscape associated with the lattice packing problem is that all of its inherent structures are *extreme* lattices, i.e., they are both *perfect* and *eutactic* [47]. Only a finite number of distinct extreme lattices exists for any dimension, which explains how the TJ algorithm is able to always reach the ground state for $d = 2$ and $d = 3$, for each of which only a single extreme lattice exists. However, as d increases, the number of extreme lattices grows quickly, possibly exponentially fast. It is thus remarkable that the TJ algorithm can reliably yield the densest lattice packing from the large set of possible end states. This indicates that the "basin of attraction" of the ground state is much larger than the basins of attraction of the local-maxima inherent structures. The relatively lower success rates for some dimensions ($d = 4$, $d = 11$, $d = 13$, and $d \geq 17$) can then be understood as being due to smaller than usual basins for the corresponding ground states. The cause of this reduction and whether the symmetry of the inherent structure is lower than that of the ground state or some other effect is still unknown and warrants further investigation.

Table 5.3: Second and third highest-density inherent structures (locally densest lattice packings), including their packing density ϕ, kissing number Z, and success rate from the TJ algorithm. See Table 5.2 to compare to the densest lattice packings. The number of lattice packings generated for each dimension is 10000 for $d \leq 18$ and 100000 for $d = 19$. Multiple lattices with equal density are grouped together and written in ascending kissing number order. See Ref. [26] for the definitions of the following lattices: A_5^{+3}, E_6^*, $P7.3$, $P7.5$, K_9^2, Dim11 (named dim11kis422 in the reference), K_{14}^1, K_{14}^2, Λ_{15}^2, K_{15}^1, Λ_{16}^2, and K_{16}^1. Lattices that were not identified in Ref. [26] and found here are denoted as U_d^n, where n is used to distinguish different lattices at some fixed dimension d.

	Second densest				Third densest			
d	Lattice	ϕ	Z	Rate (%)	Lattice	ϕ	Z	Rate (%)
2	—	—	—	—	—	—	—	—
3	—	—	—	—	—	—	—	—
4	A_4	0.5517	20	25.69	—	—	—	—
5	A_5^{+3}	0.4136	30	1.51	A_5	0.3799	30	1.08
6	E_6^*	0.3315	54	1.53	D_6	0.3230	60	7.70
7	$P7.3$	0.2143	72	0.88	$P7.5/D_7$	0.2088	72/84	1.92/0.11
8	U_8^1	0.1691	142	0.41	U_8^2	0.1530	116	3.75
9	U_9^1	0.1383	258	2.60	K_9^2	0.1190	198	14.09
10	U_{10}^1	0.08282	294	0.42	U_{10}^2	0.08231	308	0.05
11	Dim11/$\Lambda_{11}^{\min}$/$\Lambda_{11}^{\max}$	0.05888	422/432/438	5.32/7.80/0.30	U_{11}^1	0.05551	408	0.81
12	$\Lambda_{12}^{\min}$/$\Lambda_{12}^{\text{mid}}$/$\Lambda_{12}^{\max}$	0.04173	624/632/648	9.24/2.96/0.03	$U_{12}^1/U_{12}^2/U_{12}^3$	0.03732	550/560/566	1.38/0.18/0.05
13	$\Lambda_{13}^{\min}$/$\Lambda_{13}^{\text{mid}}$/$\Lambda_{13}^{\max}$	0.02846	888/890/906	12.17/1.50/0.29	U_{13}^1	0.02683	828	2.97
14	U_{14}^1	0.01934	1260	0.69	K_{14}^2/K_{14}^1	0.01922	1242/1248	2.26/0.38
15	Λ_{15}^2/U_{15}^1	0.01376	1872/1890	1.57/0.02	K_{15}^1	0.01298	1746	0.92
16	Λ_{16}^2	0.01040	2982	0.69	K_{16}^1/U_{16}^1	0.009805	2772/2820	0.67/0.03
17	U_{17}^1	0.007194	4266	0.63	U_{17}^2	0.006661	3942	0.09
18	U_{18}^1	0.005134	6336	0.03	U_{18}^2	0.004743	5820	0.02
19	U_{19}^1	0.003686	9480	0.012	U_{19}^2	0.003475	8910	0.002

As seen in Table 5.3, some inherent structures are degenerate in the sense that multiple lattices share the same packing density. A peculiar property that these degeneracies share is that their appearance rate is far from constant. For example, it goes from 9.24% for the $\Lambda_{12}^{\min}$ to a mere 0.03% for the $\Lambda_{12}^{\max}$. Since both of these are laminated lattices, why does one occurs more frequently than the other? One possible reason is that for all these degeneracies but one, the lattices with smaller kissing number are more likely to be generated. In the case of $\Lambda_{12}^{\min}$ and $\Lambda_{12}^{\max}$, their kissing numbers are respectively 624 and 648. This is consistent with previous work which has shown that for packings with many particles per fundamental cell, the TJ algorithm has a propensity to generate isostatic packings from random initial

conditions, where the number of interparticle contacts is equal to the number of degrees of freedom of the problem [32].

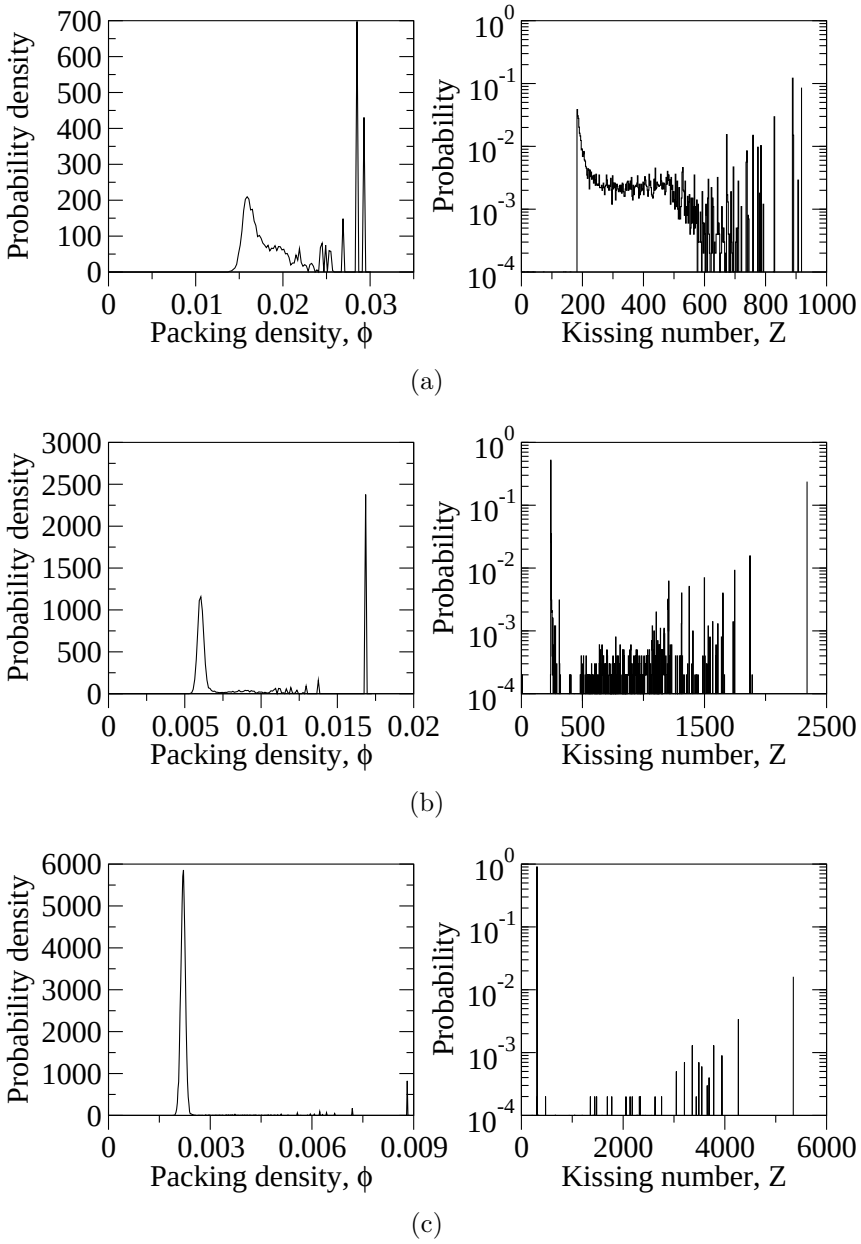

Figure 5.1: Probability density functions for the packing density ϕ (left) and probabilities for the kissing number z (right) of the lattice resulting from the TJ algorithm for (a) $d = 13$, (b) $d = 15$, and (c) $d = 17$. The minimal value of the kissing number $Z_{min} = d(d + 1)$ is 182 for $d = 13$, 240 for $d = 15$, and 106 for $d = 17$.

Figure 5.1 shows that as the dimensionality increases, the inherent-structure densities tend to become concentrated around a specific value instead of being spread

over a range of possible densities. This concentration tendency is caused by the rapid increase in the number of such low-density inherent structures for large d, which eventually overwhelms the algorithmic bias toward high-density lattices. This explains the dramatic reduction in success rates in Table 5.2 for $d \geq 17$. The kissing number has a similar behavior to the packing density, resulting in the fact that most of the generated lattices for $d \geq 17$ have an identical low kissing number. Since these are locally-optimal solutions, a local deformation of the lattice would either decrease its packing fraction or makes the central sphere and its neighboring spheres overlap. Therefore, we can define a lower bound on the kissing number by exploiting the fact that, for a linear program to have a unique feasible solution, it requires at least one more active inequality constraint than the number of degrees of freedom. Since the problem possesses $d(d+1)/2$ degrees of freedom (the number of independent components of $\boldsymbol{\varepsilon}$), $1 + d(d+1)/2$ active inequality constraints are required for the problem to be fully constrained. One of these constraints comes from the density being at a local maximum, while each pair of kissing spheres adds a single constraint. Consequently, the minimum kissing number of a lattice inherent-structure in d dimensions is $Z_{min} = d(d+1)$. Referring to Fig. 5.1, we observe that as d increases, the proportion of generated configurations with a kissing number equal to Z_{min} increases rapidly relative to all other kissing numbers. Since the best known lattice packings have high kissing numbers (nearly the same or equal to highest known kissing numbers), the tendency of the TJ algorithm tendency to favor lattices with minimal kissing numbers further explains its low success rates for $d \geq 17$.

5.5 Conclusions and Discussion

In this chapter, we have shown that the Torquato-Jiao algorithm is able to quickly find the densest known lattice packings for $d \leq 19$. The TJ algorithm is found

to be orders of magnitude faster than the previous state-of-the-art lattice packing methods [19, 20]. This makes the TJ algorithm the fastest current numerical method to generate the densest lattice packings in high dimensions.

While we limited our present study to $d \leq 19$, the TJ algorithm can be employed to generate dense lattice packings in higher dimensions at greater computational cost. We expect that dimensions $d = 20$ and $d = 21$ would be manageable with more computing resources, but improvements to the algorithm would be required to study $d \geq 22$. One possible approach to increase the likelihood of generating a dense lattice packing for $d \geq 22$ would be to include *ad hoc* methods in between the TJ-algorithm steps that favor denser packings, such as thermal equilibration of the system (e.g., via Monte Carlo methods to solve the "adaptive shrinking cell" optimization problem [51, 52]) or relaxation under pair potentials known to favor high-density configurations. Another possibility would be to combine the strengths of the TJ algorithm with those of other lattice packing methods. The ability of the TJ algorithm to quickly generate extreme lattices (the inherent structures) could be used as a starting point for an algorithm that performs an exhaustive search in the space of perfect lattices [20]. Moreover, its efficiency in finding locally-densest lattice packings from arbitrary initial conditions could be used to rapidly obtain such packings starting from intermediate-density packings generated using other methods [19]. As d increases from one, the first dimension in which the densest known packing that is not a Bravais lattice (periodic packing with a multiple-particle basis) is $d = 10$, which has a basis of 40. Since the TJ algorithm was successfully used to obtain the densest known packings for $d \leq 6$ with a large multiple-particle basis (up to a basis of 729 for $d = 6$) [32], it would be interesting to explore whether the TJ algorithm could be used to discover currently unknown denser non-lattice packings in 10 dimensions or higher.

For $d \geq 17$ dimensions, the TJ algorithm mainly produces lattices that have both a low packing density and a minimal kissing number, while still being locally densest, revealing a richer and more complex density landscape than in most dimensions less than 17. This phenomenon could possibly be exploited to quickly generate low-density extreme lattices in very high dimensions. Since these lattices are strictly jammed and have the minimal kissing number to ensure mechanical stability, they can be considered to be the lattice analogs to the maximally random jammed packings (disordered local-maxima inherent structures) that have been generated using the TJ algorithm with many particles per fundamental cell [32]. Such configurations could be generated in much higher dimensions than those considered in this chapter, since the requirement of reaching the ground state would be removed, and the TJ algorithm is less resource-intensive when generating suboptimal kissing configurations (through the reduced number of constraints).

5.A Lattice definitions

In this appendix, we define some common lattices, following the notation and nomenclature used in Refs. [22] and [26].

The *hypercubic* $\mathbb{Z}^d$ lattice is defined by

$$\mathbb{Z}^d = \{(x_1, \ldots, x_d) : x_i \in \mathbb{Z}\} \quad \text{for } d \geq 1 \tag{5.14}$$

where $\mathbb{Z}$ is the set of integers $(\ldots -3, -2, -1, 0, 1, 2, 3 \ldots)$ and $x_1, \ldots, x_d$ denote the components of a lattice vector. The kissing number of $\mathbb{Z}^d$ is $2d$. A d-dimensional generalization of the face-centered-cubic lattice is the *checkerboard* D_d lattice defined by

$$D_d = \{(x_1, \ldots, x_d) \in \mathbb{Z}^d : x_1 + \cdots + x_d \ \text{ even}\} \quad \text{for } d \geq 2. \tag{5.15}$$

Its kissing number is $2d(d-1)$. Note that D_2 is simply the square lattice $\mathbb{Z}^2$. Another generalization of the face-centered-cubic lattice is the *root* lattice A_d, which is a subset of points in $\mathbb{Z}^{d+1}$, i.e.,

$$A_d = \{(x_0, x_1, \ldots, x_d) \in \mathbb{Z}^{d+1} : x_0 + x_1 + \cdots + x_d = 0\} \quad \text{for } d \geq 1. \tag{5.16}$$

The kissing number of A_d is $d(d+1)$. In three dimensions, D_3 and A_3 are identical, but D_d and A_d are inequivalent for $d \geq 4$. Another set of root lattices is denoted E_d, for $d = 6$, $d = 7$, and $d = 8$. The root lattice E_8 is equal to the union of D_8 and the translation of D_8 by $(\frac{1}{2}, \frac{1}{2}, \frac{1}{2}, \frac{1}{2}, \frac{1}{2}, \frac{1}{2}, \frac{1}{2}, \frac{1}{2})$. The root lattice E_7 is the section of E_8 where the sum of the lattice coefficients is set equal to zero, and the root lattice E_6 is the section of E_7 where the sum of the first and eight coefficients is also set equal to zero. Alternatively, vectors in E_8 perpendicular to any A_2-sublattice in E_8 also form E_6.

The *laminated* lattice Λ_d is constructed by stacking layers of a $(d-1)$-dimensional laminated lattice Λ_{d-1} as densely as possible such that the shortest vector in Λ_d is of equal or longer length than the shortest vector in Λ_{d-1}. This definition does not uniquely define Λ_d for all dimensions. For $d = 11$, $d = 12$, $d = 13$, and $d \geq 25$, there exist multiple laminated lattices of equal densities, which we distinguish using superscripts. Many of the previously defined lattices are also laminated lattices. For example, $\Lambda_1 = \mathbb{Z}^1$, $\Lambda_2 = A_2$, $\Lambda_3 = D_3$, $\Lambda_4 = D_4$, $\Lambda_5 = D_5$, $\Lambda_6 = E_6$, $\Lambda_7 = E_7$, and $\Lambda_8 = E_8$. A particularly interesting laminated lattice is the 24-dimensional Leech lattice Λ_{24}. Finally, the *Coxeter-Todd* lattice K_{12} can be defined for 18 dimensions:

$$K_{12} = \{(x_{11}, \cdots, x_{16}, x_{21}, \cdots, x_{26}, x_{31}, \cdots, x_{36}) : x_{ij} \in \mathbb{Z}\}, \tag{5.17}$$

where x_{ik} denotes the components of a lattice vector, subject to the following conditions

$$x_{i1} + x_{i2} + x_{i3} = 0 \qquad i \in \{1, \cdots, 6\}, \tag{5.18}$$

$$x_{i1} - x_{j1} \equiv x_{i2} - x_{j2} \equiv x_{i3} - x_{j3} \mod 3 \qquad i, j \in \{1, \cdots, 6\}, \text{and} \tag{5.19}$$

$$x_{1k} + x_{2k} + x_{3k} + x_{4k} + x_{5k} + x_{6k} \equiv 0 \mod 3 \qquad k \in \{1, 2, 3\}. \tag{5.20}$$

This lattice can be generalized to other dimensions in the range $6 \leq d \leq 18$ by requiring that K_d is the densest section of K_{d+1} which either contains or is contained in K_{12} and taking $K_{18} = \Lambda_{18}$.

Bibliography

[1] J. P. Hansen and I. R. McDonald, *Theory of Simple Liquids* (Academic, New York, 1986).

[2] P. M. Chaikin and T. C. Lubensky, *Principles of Condensed Matter Physics* (Cambridge University Press, New York, 2000).

[3] R. Zallen, *The Physics of Amorphous Solids* (Wiley, New York, 1983).

[4] S. Torquato, T. M. Truskett, and P. G. Debenedetti, *Is Random Close Packing of Spheres Well Defined?*, Phys. Rev. Lett. 84, 2064 (2000).

[5] G. Parisi and F. Zamponi, *Mean-field theory of hard sphere glasses and jamming*, Rev. Mod. Phys. 82, 789 (2010).

[6] Z. W. Salsburg and W. W. Wood, *Equation of State of Classical Hard Spheres at High Density*, J. Chem. Phys. 37, 798 (1962).

[7] S. Torquato and F. H. Stillinger, *Toward the jamming threshold of sphere packings: Tunneled crystals*, J. Appl. Phys. 102, 093511 (2007); *Erratum: "Toward the jamming threshold of sphere packings: Tunneled crystals"*, 103, 129902 (2008).

[8] T. Aste and D. Weaire, *The Pursuit of Perfect Packing* (Taylor & Francis, New York, 2008).

[9] A. Mehta, *Granular Matter: An Interdisciplinary Approach* (Springer-Verlag, New York, 1994).

[10] S. F. Edwards and D. V. Grinev, *Statistical Mechanics of Stress Transmission in Disordered Granular Arrays*, Phys. Rev. Lett. 82, 5397 (1999); *The tensorial formulation of volume function for packings of particles*, Chem. Eng. Sci. 56, 5451 (2001).

[11] S. Torquato and F. H. Stillinger, *Multiplicity of Generation, Selection, and Classification Procedures for Jammed Hard-Particle Packings*, J. Phys. Chem. B 105, 11849 (2001).

[12] S. Torquato and F. H. Stillinger, *Jammed hard-particle packings: From Kepler to Bernal and beyond*, Rev. Mod. Phys. 82, 2633 (2010).

[13] S. Torquato, *Random Heterogeneous Materials: Microstructure and Macroscopic Properties* (Springer, New York, 2002).

[14] T. C. Hales, Ann. Math., *A proof of the Kepler conjecture*, **162**, 1065 (2005).

[15] H. Cohn and A. Kumar, *Optimality and uniqueness of the Leech lattice among lattices*, Ann. Math., **170**, 1003 (2009).

[16] D. J. Gross, J. A. Harvey, E. Martinec, and R. Rohm, *Heterotic String*, Phys. Rev. Lett. **54**, 502 (1985).

[17] G. Chapline, *Unification of gravity and elementary particle interactions in 26 dimensions?*, Phys. Lett. B **158**, 393 (1985).

[18] S. Torquato and F. Stillinger, *New Conjectural Lower Bounds on the Optimal Density of Sphere Packings*, Exp Math. **15**, 307 (2006); A. Scardicchio, F. H. Stillinger, and S. Torquato, *Estimates of the optimal density of sphere packings in high dimensions*, J. Math. Phys. **49**, 043301 (2008).

[19] Y. Kallus, V. Elser, and S. Gravel, *Method for dense packing discovery*, Phys. Rev. E **82**, 056707 (2010).

[20] A. Andreanov and A. Scardicchio, *Random perfect lattices and the sphere packing problem*, Phys. Rev. E, **86**, 041117 (2012).

[21] C. E. Shannon, *A mathematical theory of communication*, Bell Syst. Tech. J. **27**, 379 (1948); **27**, 623 (1948).

[22] J. H. Conway and N. J. A. Sloane, *Sphere Packings, Lattices, and Groups* (Springer, New York, 1998).

[23] P. Sarnak and A. Strömbergsson, *Minima of Epstein's Zeta function and heights of flat tori*, Invent. Math. **165**, 115 (2006).

[24] S. Torquato, *Reformulation of the covering and quantizer problems as ground states of interacting particles*, Phys. Rev. E **82**, 056109 (2010).

[25] H. Cohn, Y. Jiao, A. Kumar, and S. Torquato, *Rigidity of spherical codes*, Geom. Topology **15**, 2235 (2011).

[26] G. Nebe and N. J. A. Sloane, *Catalogue of Lattices*, `http://www.math.rwth-aachen.de/~Gabriele.Nebe/LATTICES/`.

[27] It should be noted that the algorithm presented in Ref. [20] was designed to explore general suboptimal perfect lattice packings (not necessarily the densest lattice packings) and whether their statistics have implications for bounds on the maximal density.

[28] B. D. Lubachevsky and F. H. Stillinger, *Geometric properties of random disk packings*, J. Stat. Phys. **60**, 561 (1990).

[29] A. Donev, S. Torquato, and F. H. Stillinger, *Neighbor list collision-driven molecular dynamics simulation for nonspherical hard particles. I. Algorithmic details*,

J. Comput. Phys. **202**, 737 (2005); *Neighbor list collision-driven molecular dynamics simulation for nonspherical hard particles.: II. Applications to ellipses and ellipsoids*, J. Comput. Phys. **202**, 765 (2005).

[30] Y. Jiao, F. H. Stillinger, and S. Torquato, *Optimal Packings of Superdisks and the Role of Symmetry*, Phys. Rev. Lett. **100**, 245504 (2008).

[31] Y. Jiao, F. H. Stillinger, and S. Torquato, *Optimal packings of superballs*, Phys. Rev. E **79**, 041309 (2009).

[32] S. Torquato and Y. Jiao, *Robust algorithm to generate a diverse class of dense disordered and ordered sphere packings via linear programming*, Phys. Rev. E, **82**, 061302 (2010).

[33] A. B. Hopkins, Y. Jiao, F. H. Stillinger, and S. Torquato, *Phase Diagram and Structural Diversity of the Densest Binary Sphere Packings*, Phys. Rev. Lett. **107**, 125501 (2011).

[34] A. B. Hopkins, F. H. Stillinger, and S. Torquato, *Densest binary sphere packings*, Phys. Rev. E **85**, 021130 (2012).

[35] In the physical sciences and engineering, a lattice is usually referred as a Bravais lattice.

[36] M. Ajtai, *Generating Hard Instances of Lattice Problems*, Proc. 28th Annual ACM Symp. Theory of Computing, (1996).

[37] Finding the lattice which maximizes ϕ is equivalent to determining the ground states (global minima) in the "energy landscape" in which the "energy" is $-\phi$, where the degrees of freedom are the components of $\mathbf{M}_\Lambda$. Following Torquato and Jiao [32], we call the stable local/global density maxima (or energy minima) *inherent structures*.

[38] H. Cohn, A. Kumar, and A. Schürmann, *Ground states and formal duality relations in the Gaussian core model*, Physical Review E **80**, 061116 (2009).

[39] U. Fincke and M. Pohst, *Improved methods for calculating vectors of short length in a lattice, including a complexity analysis*, Math. Comp., **44**, 463 (1985).

[40] An asymmetric shear tensor $\boldsymbol{\varepsilon}$ could have been used, but the set of inherent-structure solutions would have been unchanged. Under this more general asymmetric form, in all of the linearized Eqs. (5.7), (5.9), (5.10), and (5.12), $\boldsymbol{\varepsilon}$ would be replaced by the symmetrized tensor $(\boldsymbol{\varepsilon} + \boldsymbol{\varepsilon}^{\top})/2$. The only impact from the antisymmetric portion of such an $\boldsymbol{\varepsilon}$ would be to add trivial $d(d-1)/2$ rotational degrees of freedom to Λ, which are irrelevant as far as the packing density is concerned.

[41] S. Torquato, A. Donev, and F. H. Stillinger, *Breakdown of elasticity theory for jammed hard-particle packings: conical nonlinear constitutive theory*, Int. J. Solids Struct. **40**, 7143 (2003).

[42] The strict jamming of the resulting configuration can only be guaranteed as long as the packing is restricted to a lattice, i.e., one sphere per fundamental cell. For any such strictly jammed lattice sphere packing, it is possible that density-preserving or density-increasing deformations exist on a larger torus involving this structure that would lead to unjamming motions. This possibility increases with increasing dimension, since all lattice packings almost surely become "unsaturated" (holes exist that can accommodate extra spheres) in sufficiently high dimensions [22].

[43] It is important to realize that the linear programs that the TJ algorithm solves often do not have unique solutions. Therefore, the TJ algorithm is guaranteed to be deterministic only if the selection of an optimal solution is also guaranteed

to be deterministic. An example of multiple equivalent solutions occurs if all of the lattice non-zero vector lengths are larger than the sphere of influence radius R_I, in which case the only linearized problem constraints will be those on the shear matrix $\boldsymbol{\varepsilon}$. Then, as long as they satisfy inequality (5.10), the non-diagonal elements of $\boldsymbol{\varepsilon}$ can take any value, without any impact on the objective function.

[44] *Gurobi Optimizer*, version 5.0.2, Gurobi Optimization, `www.gurobi.com`.

[45] D. Goldstein and A. Mayor, *On the equidistribution of Hecke points*, Forum Math. **15**, 165 (2003); H. Cohn and G. Minton, private communication, 2013.

[46] A. Andreanov and A. Scardicchio, private communication, 2013.

[47] *Perfect* lattices in d dimensions have the property that any $d \times d$ symmetric matrix S can be written as a linear combination of the lattice shortest vector projectors $\mathbf{v}_i^{min}$, *i.e.*

$$S = \sum_{i=1}^{Z} \alpha_i \mathbf{v}_i^{min} \mathbf{v}_i^{min\top},$$

where Z is the lattice kissing number and α_i are linear combination coefficients. All perfect lattices for $1 \leq d \leq 8$ have been identified. There are 1, 1, 1, 2, 3, 7, 33, and 10916 perfect lattices for $d = 1$ through $d = 8$, respectively [26]. *Eutactic* lattices in d dimensions have the property than each of their shortest vector $\mathbf{v}_i^{min}$ is associated with a positive *eutactic coefficient* $\beta_i > 0$ such that the norm of any vector $\mathbf{x}$ can be written as:

$$|\mathbf{x}|^2 = \sum_{i=1}^{Z} \beta_i \left(\mathbf{v}_i^{min\top} \mathbf{x}\right)^2.$$

A lattice is a local maximum in density (i.e., an inherent structure) if and only if it is an *extreme* lattice, which is both perfect and eutactic [48]. There are 1, 1, 1, 2, 3, 6, 30, and 2408 extreme lattices for $d = 1$ through $d = 8$, respectively [49, 50].

[48] G. Voronoi, *Nouvelles applications des paramètres continus à la théorie des formes quadratiques. Premier mémoire. Sur quelques propriétés des formes quadratiques positives parfaites.*, J. reine angew. Math. **133**, 97 (1908).

[49] J. Martinet, *Perfect lattices in Euclidean Spaces* (Springer, New York, 2003).

[50] C. Riener, *On extreme forms in dimension 8*, J. Th. Nombres Bordeaux **18**, 677 (2006).

[51] S. Torquato and Y. Jiao, *Dense packings of polyhedra: Platonic and Archimedean solids*, Phys. Rev. E **80**, 041104 (2009).

[52] S. Atkinson, Y. Jiao, and S. Torquato, *Maximally dense packings of two-dimensional convex and concave noncircular particles*, Phys. Rev. E **86**, 031302 (2012).

Chapter 6

Nonequilibrium Static Growing Length Scales in Supercooled Liquids on Approaching the Glass Transition

6.1 Introduction

A quantitative understanding of nature of the physics of the glass transition is one of the most fascinating and challenging problems in materials science and condensed-matter physics. A sufficiently rapid quench of a liquid from above its freezing temperature into a supercooled regime can avoid crystal nucleation to produce a glass with a relaxation time that is much larger than experimental time scales, resulting in an amorphous characteristic state (without long-range order) that is simultaneously rigid [1]. A question that has received considerable attention in recent years is whether the growing relaxation times under supercooling have accompanying growing structural length scales. Two distinct schools of thought have emerged to address this ques-

tion. One asserts that static structure of a glass, as measured by pair correlations, is indistinguishable from that of the corresponding liquid. Thus, since there is no signature of increasing static correlation length scales accompanying the glass transition, it identifies growing dynamical length scales [2, 3, 4]. The other camp contends that there is a static growing length scale of *thermodynamic* origin [5, 6] and therefore one need not look for growing length scales associated with the dynamics.

In the present chapter, we employ both theoretical and computational methods to study two different atomic glass-forming liquid models that support an alternative view, namely, the existence of a growing *static* length scale as the temperature of the supercooled liquid is decreased that is intrinsically *nonequilibrium* in nature. This investigation extends recent previous work [7] in which this conclusion was first reached by examining overcompressed hard-sphere liquids up to the maximally random jammed (MRJ) state [8]. (For a hard-sphere system, compression qualitatively plays the same role as decreasing the temperature in an atomic or molecular system; see Ref. [9].) The MRJ state under the strict-jamming constraint is a *prototypical* glass in that it lacks any long-range order but is perfectly rigid such that the elastic moduli are unbounded [9, 10]. This endows such packings with the special *hyperuniformity* attribute. A statistically homogeneous and isotropic single-component point configuration at number density ρ is hyperuniform if its structure factor

$$S(k) = 1 + \rho\widetilde{h}(k) \tag{6.1}$$

tends to zero as the wavenumber $k \to 0$ [11], where $h(r) \equiv g_2(r) - 1$ is the total correlation function, $g_2(r)$ is the pair correlation function, and $\widetilde{h}(k)$ is the Fourier transform of $h(r)$. This condition implies that infinite-wavelength density fluctuations vanish.

It was theoretically established that hyperuniform point distributions are at an "inverted" critical point in that the direct correlation function $c(r)$, rather than the total correlation function $h(r)$, becomes long-ranged, i.e., it decays more slowly than $-1/r^d$ in d-dimensional Euclidean space $\mathbb{R}^d$, where r is the radial distance [11]. The Fourier transform of direct correlation function $\widetilde{c}(k)$ is defined via the Ornstein-Zernike equation [12]:

$$\widetilde{c}(k) = \frac{\widetilde{h}(k)}{1 + \rho\widetilde{h}(k)} = \frac{S(k) - 1}{\rho S(k)}. \tag{6.2}$$

It is immediately clear from this definition that the real-space volume integral of the direct correlation function $c(r)$ diverges to minus infinity for any hyperuniform system, since the denominator of (6.2) tends to zero, i.e.,

$$\lim_{k \to 0} \widetilde{c}(k) = \int_{\mathbb{R}^d} c(r) d\mathbf{r} \to -\infty \tag{6.3}$$

MRJ packings of identical spheres possess a special type of hyperuniformity such that $S(k)$ tends to zero linearly in k as $k \to 0$, implying quasi-long-ranged negative pair correlations (anticorrelations) in which $h(r)$ in three dimensions decays as a power law $-1/r^4$ or, equivalently, a direct correlation function that decays as $c(r) \sim -1/r^2$ for large r, as dictated by Eq. (6.2) [13]. These anticorrelations reflect an unusual spatial patterning of regions of lower and higher local particle densities relative to the system density. This quasi-long-range behavior of $h(r)$ is distinctly different from typical liquids in equilibrium, which tend to exhibit more rapidly decaying pair correlations, including exponential decays.

Reference [7] examined overcompressed hard-sphere configurations that follow Newtonian dynamics for a wide range of densities up to the MRJ state. A central result of that study was to establish that a precursor to the glassy jammed state was evident long before the MRJ density was reached as measured by an associated growing length scale, extracted from the volume integral of the direct correlation

function $c(r)$, which of course diverges at the "critical" hyperuniform MRJ state. It was also shown that the nonequilibrium signature of the aforementioned quasi-long-range anticorrelations, which was quantified via a *nonequilibrium index* X, emerges well before the jammed state was reached.

These results for nonequilibrium amorphous hard-sphere packings suggest that the direct correlation function of supercooled atomic models in which the atoms possess both repulsive and attractive interactions should provide a robust *nonequilibrium* static growing length scale as the temperature is decreased to the glass transition and below. Here we show that this is indeed the case by extracting length scales associated with standard and generalized direct correlation functions. In particular, we study the single-component Z2 Dzugutov potential in three dimensions and the binary-mixture Kob-Andersen potential in two dimensions. The Z2 Dzugutov potential for a single-component many-particle system in three dimensions has the following form [14]:

$$v(r) = \begin{cases} a\frac{e^{\eta r}}{r^3}\cos(2k_f r) + b\left(\frac{\sigma}{r}\right)^n + V_0, & r < r_c, \\ 0, & r \geq r_c. \end{cases} \tag{6.4}$$

The first term in (6.4) models Friedel oscillations for a metal with Fermi wave vectors of magnitude k_F, while the second term adds a strong repulsion for sufficiently small interparticle separations. The parameters a and b control the relative strengths of both contributions and define the energy scale. The cutoff r_c is selected to be at the third minimum of the potential, while the constant V_0 is present to make the potential continuous at the cutoff. The parameters η, σ, and n control the shapes of both functions in (6.4). The Kob-Andersen model for a two-dimensional binary mixture is given by a truncated Lennard-Jones potential [15]:

$$v_{\alpha\beta}(r) = \begin{cases} 4\epsilon_{\alpha\beta}\left[\left(\frac{\sigma_{\alpha\beta}}{r}\right)^{12} - \left(\frac{\sigma_{\alpha\beta}}{r}\right)^{6}\right] + V_{0\alpha\beta}, & r < 2.5\sigma_{\alpha\beta}, \\ 0, & r \geq 2.5\sigma_{\alpha\beta}. \end{cases} \tag{6.5}$$

The parameter $\epsilon_{\alpha\beta}$ controls the strength of the attraction between two particles of species α and β, while $\sigma_{\alpha\beta}$ is equal to $2^{-1/6}$ times the distance between both particles at which the pair potential has a minimum.

It is known that overcompressing a hard-sphere system is analogous to supercooling a thermal liquid, but to what extent does this analogy hold? Roughly speaking, a rapid densification of a monodisperse hard-sphere system leads to the terminal MRJ state (with packing fraction of about 0.64), which we have noted is a prototypical glass [9]. At this singular state, the system is never able to relax and hence the associated relaxation time is infinite [16]. Slower densification rates lead to other jammed states with packing fractions higher than 0.64 [9]. Moreover, it has been shown that below 0.64, metastable hard-sphere systems have bounded characteristic relaxation times [16, 17], including the range of packing fractions of about $0.58 \sim 0.60$ (depending on the densification rate) that has been interpreted to be the onset of a kinetic glass transition [17]. Above a particular hard-sphere glass-transition density, the system is able to support a shear stress on time scales small compared to a characteristic relaxation time. Clearly, increasing the density of a hard-sphere system plays the same role as decreasing temperature of a thermal liquid. In a thermal system, a glass at absolute zero temperature has an infinite relaxation time classically, and hence this state is the analog of the hard-sphere MRJ state. The glass transition temperature T_g, which depends on the quenching rate and possesses a bounded characteristic relaxation time, is analogous to the aforementioned kinetic transition in hard spheres. These strong analogies between glassy hard-sphere states and glassy atomic systems lead one to believe that the results of Ref. [7] for the former extend to the latter. Indeed, here we demonstrate that the aforementioned length scales grow as the temperature is decreased to the glass transition T_g and below. Moreover, we show that the nonequilibrium index X, previously shown [7] to increase as a hard-sphere system

is densified to the MRJ state, also grows for $T < 2.2T_g$. This nonequilibrium index is also shown to be correlated with an early relaxation time τ.

In Sec. 6.2, we introduce two generalizations of the direct correlation function $c(r)$ which apply for two-component systems. In Sec. 6.3 we describe the numerical techniques and parameters used in our simulations, while in Sec. 6.4 we present the results we extract from these simulations. The latter includes the demonstration of the existence of growing nonequilibrium static length scales upon supercooling the two atomic-liquid models that we consider. Moreover, we show that the nonequilibrium index X is positively correlated with an early relaxation time, both of which increase as the temperature is decreased to the glass transition temperature and below. We conclude in Sec. 6.5 with a summary of our results and of their impact.

6.2 Structural Signatures of Large-Wavelength Density Fluctuations in Binary Mixtures

It has been shown that for maximally random jammed binary sphere packings, the standard structure factor $S(k)$, determined from the particle centroids, cannot be used to ascertain whether the system is hyperuniform, unlike the single-component MRJ sphere packing [18, 19]. Instead it was shown that the spectral density $\widetilde{\chi}(k)$, defined below, can be employed to determine whether a binary MRJ packing is hyperuniform, since it vanishes as $k \to 0$. We will show below that one must modify the spectral density for particles interacting with soft (non-hard-core) pair potentials because particle-shape information is required in order to ascertain whether the system is hyperuniform or nearly hyperuniform. For particles interacting with a hard-core repulsion, the particle shapes are obviously the hard cores, but for non-hard-core interactions, such as in the Kob-Andersen model studied in this chapter, one must determine a self-consistent procedure to assign particle shapes to each point particle.

In addition, for such soft binary mixtures, the standard direct correlation function $c(r)$, applicable to monodisperse systems, must be generalized.

In this section, we present two generalizations of $c(\mathbf{r})$ for polydisperse systems: one that is based on the spectral density (Sec. 6.2.1), and another that is based on the matrix version of the structure factor (Sec. 6.2.2).

As indicated in the beginning of the section, we must obtain a modified version of the direct correlation function $c(r)$, defined by Eq. (6.2) for a single-component system, for binary mixtures in which the particles interact with *non-hard-core* pair potentials in order to detect hyperuniformity or near-hyperuniformity. This function must be defined to be as general as possible. In particular, it must be equivalent to the usual direct correlation function in the case of a single-component system. We shall therefore start by determining what this modified function would be in the single-component case in order to provide insight for the more general case of multiple-component systems. This will be done by decorating the underlying point configuration with nonoverlapping spheres. We first describe the single-component case and then the mixture case.

6.2.1 Single-Component Case

Consider a configuration of N points within a large volume V in which the minimum pair separation is the distance R. Now let us decorate this configuration by circumscribing spheres of radius R around each of the points, leading to a configuration of N nonoverlapping spheres of radius R. In this case, the particle phase indicator $\mathcal{I}(\mathbf{x})$ in terms of the positions of the sphere centers $\mathbf{r}_1, \mathbf{r}_2, \ldots, \mathbf{r}_N$ is [20, 21]:

$$\mathcal{I}(\mathbf{x}) = \sum_{i=1}^{N} m(|\mathbf{x} - \mathbf{r}_i|; R), \tag{6.6}$$

where $m(r;R)$ is the single-inclusion indicator function given by

$$m(r;R) \equiv \Theta(R-r) = \begin{cases} 1, & r \leq R, \\ 0, & r > R. \end{cases} \tag{6.7}$$

The two-point correlation function $S_2(r) = \langle I(\mathbf{x})I(\mathbf{x}+\mathbf{r})\rangle$ for such a statistically homogeneous and isotropic distribution of nonoverlapping spheres, equal to the probability of finding two points, separated by the distance $r \equiv |\mathbf{r}|$, anywhere in the region occupied by the spheres, has been shown to be given by the following sum of two terms [20, 21]:

$$S_2(r) = \rho m(r) \otimes m(r) + \rho^2 m(r) \otimes g_2(r) \otimes m(r) \ , \tag{6.8}$$

where $\rho = \lim_{V\to\infty} N/V$ is the number density, angular brackets denote an ensemble average, and $\otimes$ denotes a convolution integral. The quantity $\rho m \otimes m$ is the *self-correlation* term, which is equal to the probability of finding two points inside the same sphere, and $\rho^2 m \otimes g_2 \otimes m$ is the two-body correlation, the probability of finding two points in two different spheres. The autocovariance function $\chi(r)$ is:

$$\begin{aligned} \chi(r) &\equiv S_2(r) - \rho^2 v_1^2 = \rho m(r) \otimes m(r) + \rho^2 m(r) \otimes g_2(r) \otimes m(r) - \rho^2 v_1^2, \\ &= \rho m(r) \otimes m(r) + \rho^2 m(r) \otimes h(r) \otimes m(r), \end{aligned} \tag{6.9}$$

where

$$v_1(R) = \int m(r;R) d\mathbf{r} = \frac{\pi^{\frac{d}{2}} R^d}{\Gamma(1+\frac{d}{2})} \tag{6.10}$$

is the volume of a d-dimensional sphere of radius R [$v_1(R) = 4\pi R^3/3$ for $d = 3$ and $v_1(R) = \pi R^2$ for $d = 2$]. Taking the Fourier transform of Eq. (6.9) yields

$$\widetilde{\chi}(k) = \rho \widetilde{m}^2(k) + \rho^2 \widetilde{m}^2(k) \widetilde{h}(k) = \rho \widetilde{m}^2(k) S(k), \tag{6.11}$$

where $S(k)$ is the structure factor defined in (6.1). One can see from this equation that if the decorated "two-phase" nonoverlapping sphere system is hyperuniform, both $S(k)$ and $\widetilde{\chi}(k)$ go to zero as $k \to 0$ (phase in this context does not refer to a thermodynamical phase, but to either the particle or the void phase).

In order to manage the extension of the standard direct correlation function that corresponds to the autocovariance function $\chi(k)$, we present the following analysis. The self-correlation term in relation (6.9) must be subtracted because in its present form $\chi(r)$ is not analogous to $h(r)$. Thus, we introduce a modified autocovariance $H(r) = S_2(r) - \rho m(r) \otimes m(r)$, given explicitly by

$$H(r) = \rho^2 m(r) \otimes h(r) \otimes m(r). \tag{6.12}$$

Taking the Fourier transform of Eq. (6.12) leads to

$$\widetilde{H}(k) = \rho^2 \widetilde{m}^2(k) \widetilde{h}(k) = \widetilde{\chi}(k) - \rho \widetilde{m}^2(k). \tag{6.13}$$

We can now define a new direct correlation function $C(r)$ using $H(r)$:

$$H(r) = C(r) + Q(r) \otimes C(r) \otimes H(r), \tag{6.14}$$

where $Q(r)$ is a function which is to be chosen such that $\lim_{k\to 0} \widetilde{C}(k)$ diverges for any hyperuniform system, for which $\widetilde{\chi}(k) \to 0$ as $k \to 0$.

$$\widetilde{H}(k) = \widetilde{C}(k) + \widetilde{Q}(k)\widetilde{C}(k)\widetilde{H}(k), \tag{6.15}$$

$$\widetilde{C}(k) = \frac{\widetilde{\chi}(k) - \rho \widetilde{m}^2(k)}{1 + \widetilde{Q}(k)\left(\widetilde{\chi}(k) - \rho \widetilde{m}^2(k)\right)}. \tag{6.16}$$

For $\lim_{k\to 0}\widetilde{C}(k)$ to diverge for hyperuniform systems, we require that the denominator of the right side of Eq. (6.16) to be zero whenever $\widetilde{\chi}(k)=0$, leading to the requirement

$$\widetilde{Q}(k)=\frac{1}{\rho\widetilde{m}^2(k)}. \tag{6.17}$$

Inserting Eq. (6.17) into Eq. (6.15) gives the one-component decorated Ornstein-Zernike (OZ) equation:

$$\widetilde{H}(k) = \widetilde{C}(k)+\frac{\widetilde{C}(k)\widetilde{H}(k)}{\rho\widetilde{m}^2(k)}, \tag{6.18}$$

$$\widetilde{C}(k) = \rho\widetilde{m}^2(k)-\frac{\rho^2\widetilde{m}^4(k)}{\widetilde{\chi}(k)}. \tag{6.19}$$

Relation (6.19) holds for a decorated single-component system. The generalization of Eq. (6.19) for a multiple-component system can be obtained by noting that $\widetilde{Q}^{-1}(k)$ is equal to the self-correlation term. For example, for a two-component system of nonoverlapping spheres, the relations analogous to (6.17)–(6.19) are given by

$$\widetilde{Q}(k) = \frac{1}{\rho_A\widetilde{m}_A^2(k)+\rho_B\widetilde{m}_B^2(k)}, \tag{6.20}$$

$$\widetilde{H}(k) = \widetilde{\chi}(k)-\rho_A\widetilde{m}_A^2(k)-\rho_B\widetilde{m}_B^2(k)=\widetilde{C}(k)+\frac{\widetilde{C}(k)\widetilde{H}(k)}{\rho_A\widetilde{m}_A^2(k)+\rho_B\widetilde{m}_B^2(k)}, \tag{6.21}$$

$$\widetilde{C}(k) = \rho_A\widetilde{m}_A^2(k)+\rho_B\widetilde{m}_B^2(k)-\frac{\left(\rho_A\widetilde{m}_A^2(k)+\rho_B\widetilde{m}_B^2(k)\right)^2}{\widetilde{\chi}(k)}, \tag{6.22}$$

where ρ_A and ρ_B are the number densities of species A and B, respectively, and $m_A(r)$ and $m_B(r)$ are the corresponding sphere indicator functions.

6.2.2 Mixture Case

Consider an M-component system, in which N_α represents the number of particles of species α, where $\alpha = A, B, \ldots$. Following Ref. [22], we write the following OZ equation for the mixture total correlation function $h_{\alpha\beta}(r)$ and the direct correlation

function $c_{\alpha\beta}(r)$:

$$h_{\alpha\beta}(r) = c_{\alpha\beta}(r) + \sum_{\gamma=1}^{M} \rho_\gamma c_{\alpha\gamma} \otimes h_{\gamma\beta}(r), \tag{6.23}$$

where α, β, and γ represent the different components of the system. Note that $c_{\alpha\beta}(r)$ is different from the "decorated" "two-phase" direct correlation function $C(r)$ defined in Sec. 6.2.1. Equation (6.23) can be rewritten in matrix form:

$$\begin{aligned} \sqrt{\rho_\alpha \rho_\beta} h_{\alpha\beta}(r) &= \sqrt{\rho_\alpha \rho_\beta} c_{\alpha\beta}(r) + \sum_{\gamma} \sqrt{\rho_\alpha \rho_\gamma} c_{\alpha\gamma}(r) \otimes \sqrt{\rho_\gamma \rho_\beta} h_{\gamma\beta}(r) \\ \mathbf{H}(r) &= \mathbf{C}(r) + \mathbf{C}(r) \otimes \mathbf{H}(r), \end{aligned} \tag{6.24}$$

where the components of the matrices $\mathbf{H}(r)$ and $\mathbf{C}(r)$ are given by

$$H_{\alpha\beta}(r) = \sqrt{\rho_\alpha \rho_\beta} h_{\alpha\beta}(\mathbf{r}), \tag{6.25}$$

$$C_{\alpha\beta}(r) = \sqrt{\rho_\alpha \rho_\beta} c_{\alpha\beta}(\mathbf{r}). \tag{6.26}$$

Taking the Fourier transform of Eq. (6.24) gives

$$\widetilde{\mathbf{H}}(k) = \widetilde{\mathbf{C}}(k) + \widetilde{\mathbf{C}}(k)\widetilde{\mathbf{H}}(k), \tag{6.27}$$

$$\widetilde{\mathbf{C}}(k) = \widetilde{\mathbf{H}}(k) \left(\mathbf{I} + \widetilde{\mathbf{H}}(k) \right)^{-1}, \tag{6.28}$$

where $\mathbf{I}$ is the identity matrix.

Equation (6.28) can be simplified by introducing the $M \times M$ multiple-component structure factor matrix $\mathbf{S}(k)$, whose components are denoted as $S_{\alpha\beta}(k)$:

$$\begin{aligned} \mathbf{S}(k) &= \begin{pmatrix} S_{AA}(k) & S_{AB}(k) & \cdots \\ S^*_{AB}(k) & S_{BB}(k) & \cdots \\ \vdots & \vdots & \ddots \end{pmatrix} = \begin{pmatrix} 1 + \rho_A \widetilde{h}_{AA}(k) & \sqrt{\rho_A \rho_B} \widetilde{h}_{AB}(k) & \cdots \\ \sqrt{\rho_A \rho_B} \widetilde{h}^*_{AB}(k) & 1 + \rho_B \widetilde{h}_{BB}(k) & \cdots \\ \vdots & \vdots & \ddots \end{pmatrix}, \\ &= \mathbf{I} + \widetilde{\mathbf{H}}(k), \end{aligned} \tag{6.29}$$

where $S^*_{\alpha\beta}(k)$ denotes the complex conjugate of $S_{\alpha\beta}(k)$. Substitution of Eq. (6.29) into Eq. (6.28) yields the following simpler expression for $\widetilde{\mathbf{C}}(k)$:

$$\widetilde{\mathbf{C}}(k) = \mathbf{I} - \mathbf{S}(k)^{-1}. \tag{6.30}$$

This last equation should be used carefully, since the $\mathbf{S}(k)$ matrix is rank-1 for a single realization of a system, and hence it cannot be inverted without first taking an *ensemble average* [23].

Equation (6.22), valid for the "two-phase" decoration, and Eq. (6.28) may not look similar, but their similarities can be made apparent by rewriting $\widetilde{\chi}(\mathbf{k})$ and $S_{\alpha\beta}(\mathbf{k})$ in terms of the collective coordinates $\widetilde{\rho}_\alpha(\mathbf{k})$:

$$\widetilde{\rho}_\alpha(\mathbf{k}) = \sum_{j=1}^{N_\alpha} e^{i\mathbf{k}\cdot\mathbf{r}_j^\alpha}, \tag{6.31}$$

where $\mathbf{k}$ is the wave vector and N_α is the number of particles of species α. For a single configuration of a multiple-component system in a volume V, we get the structure factor matrix components to be given by

$$S_{\alpha\beta}(\mathbf{k}) = \frac{\widetilde{\rho}_\alpha(\mathbf{k})\widetilde{\rho}^*_\beta(\mathbf{k})}{\sqrt{N_\alpha N_\beta}} - V\delta_{\mathbf{k},\mathbf{0}}. \tag{6.32}$$

Since we never compute $S_{\alpha\beta}(k=0)$ directly, instead relying on the $k \to 0$ limit, we can drop the Kronecker delta function in the following steps. For a two-component system, the spectral density for the decorated system is

$$\begin{aligned} \chi(\mathbf{r}) \;=\; & \rho_A m_A(\mathbf{r}) \otimes m_A(\mathbf{r}) + \rho_B m_B(\mathbf{r}) \otimes m_B(\mathbf{r}) + \\ & \rho_A^2 m_A(\mathbf{r}) \otimes h_{AA}(\mathbf{r}) \otimes m_A(\mathbf{r}) + \rho_A\rho_B m_A(\mathbf{r}) \otimes h_{AB}(\mathbf{r}) \otimes m_B(\mathbf{r}) + \\ & \rho_A\rho_B m_B(\mathbf{r}) \otimes h_{BA}(\mathbf{r}) \otimes m_A(\mathbf{r}) + \rho_B^2 m_B(\mathbf{r}) \otimes h_{BB}(\mathbf{r}) \otimes m_B(\mathbf{r}), \end{aligned} \tag{6.33}$$

for which the Fourier transform is given by

$$\begin{aligned}\widetilde{\chi}(\mathbf{k}) &= \rho_A\widetilde{m}_A^2(\mathbf{k}) + \rho_B\widetilde{m}_B^2(\mathbf{k}) + \rho_A^2\widetilde{m}_A^2(\mathbf{k})\widetilde{h}_{AA}(\mathbf{k}) + \rho_A\rho_B\widetilde{m}_A(\mathbf{k})\widetilde{m}_B(\mathbf{k})\widetilde{h}_{AB}(\mathbf{k}) + \\ &\quad \rho_A\rho_B\widetilde{m}_A(\mathbf{k})\widetilde{m}_B(\mathbf{k})\widetilde{h}_{BA}(\mathbf{k}) + \rho_B^2\widetilde{m}_B^2(\mathbf{k})\widetilde{h}_{BB}(\mathbf{k}) \\ &= \frac{\left|\widetilde{\rho}_A(\mathbf{k})\widetilde{m}_A(\mathbf{k}) + \widetilde{\rho}_B(\mathbf{k})\widetilde{m}_B(\mathbf{k})\right|^2}{V}. \end{aligned} \tag{6.34}$$

Using Eq. (6.34) to rewrite Eq. (6.22) leads to

$$\widetilde{C}(\mathbf{k}) = \rho_A\widetilde{m}_A^2(\mathbf{k}) + \rho_B\widetilde{m}_B^2(\mathbf{k})\left(1 - \frac{N_A\widetilde{m}_A^2(\mathbf{k}) + N_B\widetilde{m}_B^2(\mathbf{k})}{\left|\widetilde{\rho}_A(\mathbf{k})\widetilde{m}_A(\mathbf{k}) + \widetilde{\rho}_B(\mathbf{k})\widetilde{m}_B(\mathbf{k})\right|^2}\right). \tag{6.35}$$

Now, assume that the decoration of the two-component system is chosen such that $\psi(\mathbf{k}) = \left(\sqrt{\rho_A}\widetilde{m}_A(\mathbf{k}), \sqrt{\rho_B}\widetilde{m}_B(\mathbf{k})\right)^\top$ is an eigenvector of $\mathbf{S}(\mathbf{k})$. Calculating the associated eigenvalue of $\widetilde{\mathbf{C}}(\mathbf{k})$ (which shares eigenvectors with $\mathbf{S}(\mathbf{k})$) leads to

$$\frac{\psi^{*\top}(\mathbf{k})\widetilde{\mathbf{C}}(\mathbf{k})\psi(\mathbf{k})}{\rho_A\widetilde{m}_A^2(\mathbf{k}) + \rho_B\widetilde{m}_B^2(\mathbf{k})} = 1 - \frac{N_A\widetilde{m}_A^2(\mathbf{k}) + N_B\widetilde{m}_B^2(\mathbf{k})}{\left\langle\left|\widetilde{\rho}_A(\mathbf{k})\widetilde{m}_A(\mathbf{k}) + \widetilde{\rho}_B(\mathbf{k})\widetilde{m}_B(\mathbf{k})\right|^2\right\rangle}, \tag{6.36}$$

The similarities between Eqs. (6.35) and (6.36) are striking, and lend credibility to their use. However, it should not be forgotten that Eq. (6.36) is only valid for a very precise choice of $\widetilde{m}_A(\mathbf{k})$ and $\widetilde{m}_B(\mathbf{k})$, which may or may not be realizable for arbitrary systems. It is therefore more appropriate to use a decoration that uses *a priori* information about the system (e.g. an effective radius of the particles) together with Eq. (6.35). In a situation where such information is missing, calculating the actual eigenvalues of $\mathbf{S}(\mathbf{k})$ and $\widetilde{\mathbf{C}}(\mathbf{k})$ is a good alternative choice, although it requires multiple realizations of the system in order to get the ensemble-average values.

6.3 Simulation Details

We carry out molecular dynamics simulations in the NVT ensemble to study the behavior of two different atomic glass-forming liquid models: a three-dimensional single-component system in which the particles interact with the Z2 Dzugutov potential and a two-dimensional two-component system in which the particles interact with the Kob-Andersen potential. In particular, starting from liquid states, we quench these two model systems and follow their transitions from fluids, to supercooled fluids and glassy states as a function of temperature.

The interacting systems consist of $N = 100000$ particles in a two-dimensional (Kob-Andersen) or three-dimensional (Z2 Dzugutov) periodic box, subject to a Nosé-Hoover thermostat [24] with a mass set to $N/1000 = 100$. This particular choice of mass is selected to avoid the numerical instabilities that occur when a small mass is used, while reducing the time the thermostat takes to equilibrate which increases with larger masses. The initial configurations are generated using the random sequential addition (RSA) algorithm [25], and with an initial temperature that is much larger than the freezing temperature. There are four relevant units in the molecular dynamics simulations: units of energy, length, mass, and time, of which three can chosen independently. The units of energy and length are selected by the numerical values of the potentials' parameters, while the unit of mass is set by letting all particles have unit masses. These choices defined the natural units, including the unit of time. The system is then continuously cooled using an exponential rate

$$T(t) = T_0 \times 10^{-t/\tau_{10}}, \tag{6.37}$$

where $T(t)$ is the temperature when the simulation has been running for a time t, T_0 is the initial temperature, and the time per decade τ_{10} controls the cooling rate. The molecular dynamics integration is done using the velocity Verlet scheme.

For the Z2 Dzugutov potential, shown in Eq. (6.4), we use the following parameter values: $a = 1.04$, $\eta = 0.33$, $k_F = 4.139$, $b = 4.2 \times 10^7$, $\sigma = 0.348$, $n = 14.5$, $r_c = 2.64488$, and $V_0 = 0.13391543$. The values of r_c and V_0 are chosen such that both $v(r_c) = 0$ and $\frac{dv}{dr}\big|_{r=r_c} = 0$. This choice of parameters defines the natural units of both energy and length. Following Ref. [14], the particle density is fixed as $\rho = 0.84$. The time per decade τ_{10} is set to 500, 200, and 50 natural time units. Slower cooling schedules are attempted (such as $\tau_{10} = 2000$), but they lead to some of the samples crystallizing. The time step is $\Delta t = 5 \times 10^{-3}$ in the natural time units and is chosen such that the total energy of the system is conserved when the thermostat is removed.

For the Kob-Andersen potential, shown in Eq. (6.5), we use a composition of particles with number ratio $A : B = 65 : 35$ and the following parameters: $\sigma_{AA} = 1.0$, $\epsilon_{AA} = 1.0$, $\sigma_{AB} = \sigma_{BA} = 0.8$, $\epsilon_{AB} = \epsilon_{BA} = 1.5$, $\sigma_{BB} = 0.88$, and $\epsilon_{BB} = 0.5$. The values for the $V_{0\alpha\beta}$ are chosen such that the potentials are continuous at $r = 2.5\sigma_{\alpha\beta}$ cutoffs. These choices of parameters define the natural units of energy (ϵ_{AA}) and length (σ_{AA}). Both particle species are assumed to have masses equal to unity. Following Ref. [2], we set $\rho = 1.161662$. The time per decade of temperature decay τ_{10} is set to 2000, 400, 100, and 20. The time step is $\Delta t = 1 \times 10^{-3}$.

6.4 Results

6.4.1 Z2 Dzugutov Single-Component Glass

To estimate the glass transition temperature T_g of the Z2 Dzugutov model, we use the temperature at which the total energy per particle as a function of temperature changes slope most rapidly [26]. Since the harmonic contribution $3k_BT$ to the average total energy per particle u has a constant slope, we subtract it from u to detect any change of slope. As seen in Fig. 6.1, we obtain $k_BT_g \sim 0.88$ for the Z2 Dzugutov model. Comparatively, by observing the highest temperature at which the

supercooled systems crystallized and the temperature at which such crystals melt, we roughly estimate the melting temperature to be $T_m/T_g \sim 2.5 \pm 0.5$. We used a method based on a static quantity, namely the energy, to determine T_g. This is distinctly different from commonly used approaches relying on dynamical properties, such as the diffusion constant, a disadvantage of which is that the system is relaxing during the measurement of those properties.

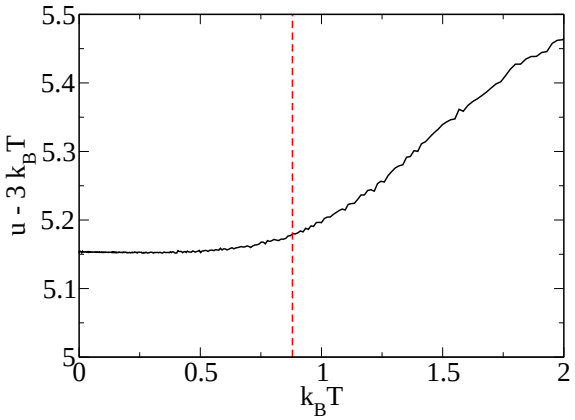

Figure 6.1: (Color online) Strictly anharmonic portion of the total average energy (kinetic and potential) per particle $u - 3k_BT$ of the system in term of the thermostat temperature T. This is obtained by averaging over 10 cooling simulations of supercooled Z2 Dzugutov systems using $\tau_{10} = 400$. $3k_BT$ has been subtracted from the energy to help identify the glass transition. The glass transition temperature $k_BT_g \sim 0.88$ is estimated by finding the temperature at which the function slope changes most rapidly. The vertical dashed line is located at $T = T_g$. The energy scale is normalized through our choice of potential parameters (see Sec. 6.3).

To calculate the volume integral of the direct correlation function $c(r)$, we need to find the limit of $S(k)$ for $k \to 0$, and then substitute it in Eq. (6.2). Since $S(k = 0)$ cannot be calculated directly in a finite simulation box of side length L because the smallest possible wavenumber accessible is $2\pi/L$, an extrapolation from the available data to zero wavenumber must be used. Figure 6.2(a) shows the small-wavelength behavior of $S(k)$ for Z2 Dzugutov model at different temperatures. It is clear that $S(k)$ is nearly linear in k for $k \lesssim 1$, leading to a very good fit to a linear function. This linear behavior of $S(k)$ for small $k > 0$ implies that the real-space total correlation

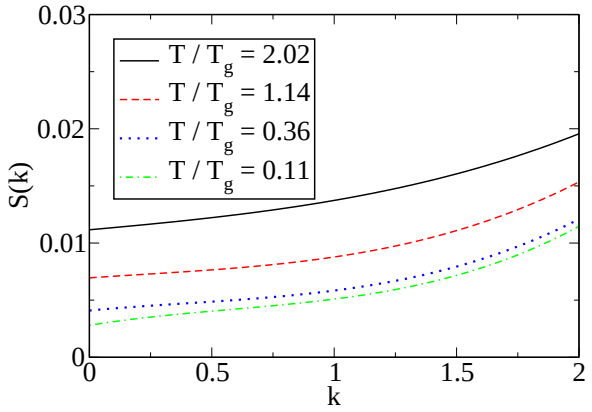

(a)

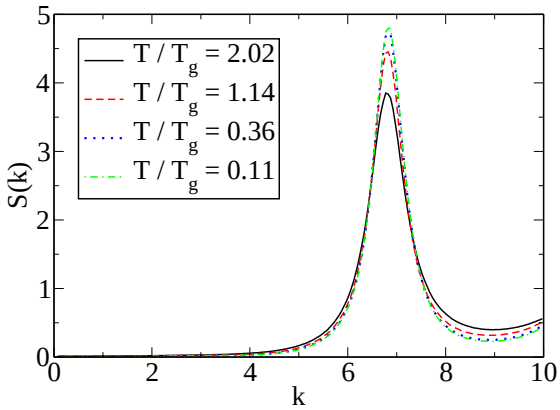

(b)

Figure 6.2: (Color online) Structure factors $S(k)$ for Z2 Dzugutov systems supercooled using $\tau_{10} = 500$ for various temperatures. The curves have been averaged over 10 realizations. (a) Cubic fits of the small-wavenumber ($k < 2$) structure factors. The type of fits and their cutoff are chosen such that they accurately reproduce the features of the structure factors, in particular the positive linear dependence near $k = 0$. (b) Larger-wavenumber structure factors.

function $h(r)$ decays, for large but finite r, as a power law $-1/r^4$ or, equivalently, the direct correlation function decays as $c(r) \sim -1/r^2$. The numerical value of $S(k=0)$ only changes by up to 5% between the cubic fit for $k < 2$ shown in Fig. 6.2(a) and a linear fit for $k < 1$. Since the linear fit is less susceptible to overfitting and complex behavior for $1 < k < 2$, we elect to use this linear fit to extrapolate the value of $S(k=0)$ for these systems. It is noteworthy that the values of $S(k=0)$ for the deeply quenched liquids are about 4 times smaller than those for the starting equilibrium liquid states. This demonstrates that a glass should not be viewed structurally as a "frozen liquid".

From the Fourier transform of the direct correlation function $\widetilde{c}(k)$, which has units of volume, we define the following length scale:

$$\xi_c \equiv [-\widetilde{c}(0)]^{1/d}, \tag{6.38}$$

where d is the Euclidean dimension. From Fig. 6.3(a), there is a striking evidence that $\widetilde{c}(k=0)$ grows to a large negative value in the supercooled regime, leading to a doubling in the value of the length scale ξ_c.

In the case of a single-component system at equilibrium, the compressibility relation links its isothermal compressibility $\kappa_T = -\frac{1}{V}\left.\frac{\partial V}{\partial p}\right|_T$ to its structure factor as follows:

$$\rho \kappa_T k_B T = S(0). \tag{6.39}$$

However, supercooled liquids and glasses are not equilibrium states and consequently Eq. (6.39) tends not to be satisfied. Following Ref. [7], we use the deviation from Eq. (6.39) to measure a nonequilibrium index X:

$$X \equiv \frac{S(0)}{\rho \kappa_T k_B T} - 1. \tag{6.40}$$

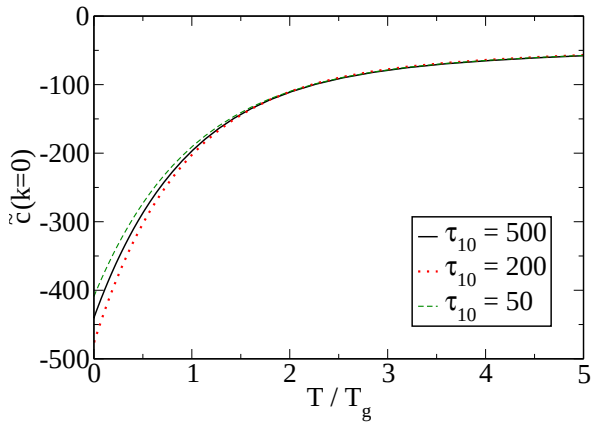

(a)

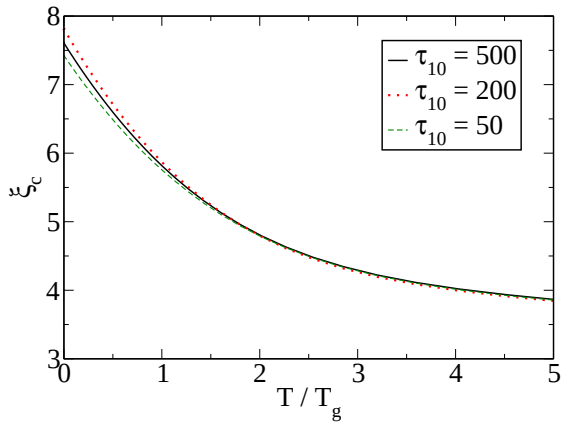

(b)

Figure 6.3: (Color online) Growing length scales for Z2 Dzugutov systems generated using various cooling schedules. For each cooling schedule, the results have been averaged over 10 realizations and fitted to the sum of an exponential and a linear function to smooth out the numerical noise. (a) Limit of $\widetilde{c}(k)$ for $k \to 0$, calculated using linear fits of $S(k)$. (b) The static length scale ξ_c, defined by relation (6.38), associated with these systems. Note that the nearest neighbor distance between particles at $T = 0$ is 1.0539.

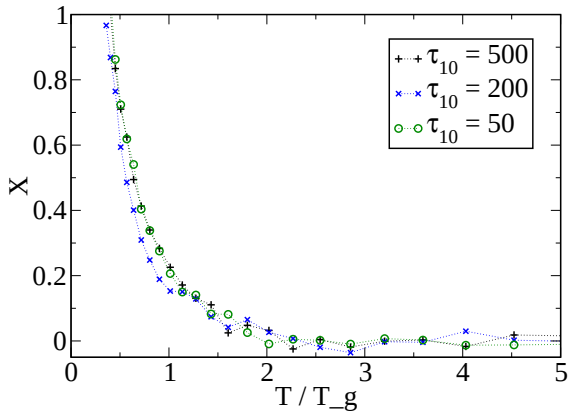

Figure 6.4: (Color online) Nonequilibrium index X for Z2 Dzugutov systems supercooled using various cooling schedules defined in Eq. (6.40).

The isothermal compressibility κ_T is computed by the following finite difference formula:

$$\kappa_T \simeq -\frac{\Delta V}{V}\frac{1}{\Delta P}, \tag{6.41}$$

where ΔV is the change in volume of the simulation box and ΔP is the resulting change in pressure of the system after it is allowed to relax at constant temperature. The pressure is calculated using the virial relation. It bears mentioning that since the system is not at equilibrium, it is not in a steady state even before the change in volume. To minimize the impact of the uncompressed system relaxation, both the uncompressed and compressed systems are allowed to relax for the same amount of time before measuring their pressures.

In the case of the Z2 Dzugutov system, we use a change of volume $\Delta V/V = 0.3\%$ and the pressure is sampled from $t = 5$ to $t = 10$, where $t = 0$ denotes the time at which the system is compressed. This sampling time is required to reduce the noise in the measured values of $S(k)$ and κ_T for a finite system. Since it is still much shorter than the system relaxation time, X can still be viewed as an instantaneous non-equilibrium property of the system. As can be seen in Fig. 6.4, X is zero [27] for $T/T_g > 2$, with only slight deviations due to noise and numerical inaccuracies. However, as the temperature is lowered to values approaching the glass transition, X

increases up to a value of ~ 0.2 at $T/T_g = 1$. For $T < T_g$, the inability of the system to relax in a time of the order of the cooling schedule time per decade τ_{10} results in nearly constant values of κ_T and $S(0)$ which leads to the asymptotic behavior of X as $T \to 0$.

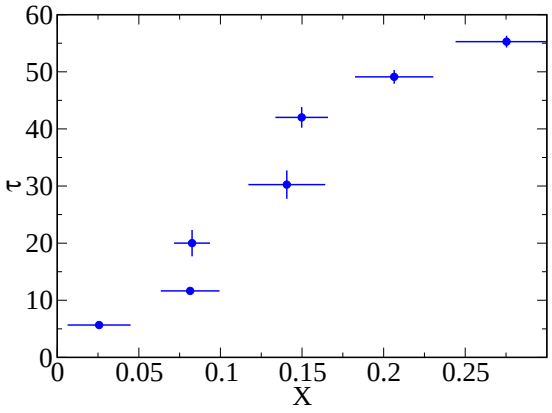

Figure 6.5: (Color online) Timescale τ of the early relaxation process of the system versus the nonequilibrium index X. Both quantities have been averaged over 10 configurations. The circle are centered on the averages of X and τ, while the horizontal and vertical lines represent their respective uncertainties, with their half-length set equal to the average standard deviations. The initial configurations which are allowed to relax at constant temperature are generated from the liquid phase through a cooling schedule employing $\tau_{10} = 50$. Each datum represents a single temperature. Observe that τ and X are positively correlated. Therefore, since X is a monotonically decreasing function of the temperature T (see Fig 6.4), τ also increases with decreasing T. The values of T/T_g associated with each datum are, in order of smallest to largest τ are as follows: 1.80, 1.61, 1.43, 1.28, 1.14, 1.01, and 0.90.

Is the growing nonequilibrium index X correlated with the growing relaxation times as the temperature decreases during the supercooling process? Figure 6.5 shows a positive correlation between X and τ, where τ is the timescale associated with the early relaxation process, extracted from an exponential fit function $\sim e^{-t/\tau}$ of the system total energy. To observe this process, we start with configurations that have been supercooled to a given temperature following a specific cooling schedule. These configurations are then allowed to evolve at constant temperature. It can be clearly seen that X and τ are strongly and positively correlated.

6.4.2 Kob-Andersen $A_{65}B_{35}$ Two-Component Glass

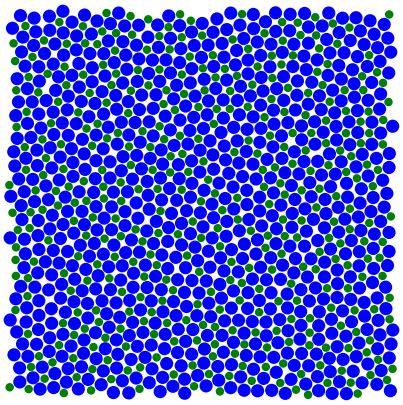

Figure 6.6: (Color online) Example of a decorated Kob-Andersen glass configuration (a small subregion of the configuration only). The larger disks represent the A particles, while the smaller disks represent B particles. The radii of the disks are chosen such that the two closest A particles of the whole configuration are in contact and the closest A–B pair of particles are in contact. The configuration shown has been generated using $\tau_{10} = 100$, and is at a temperature of $T/T_g = 6.7 \times 10^{-5}$. The particle radii are $R_A = 0.513720$ and $R_B = 0.329883$ ($R_A/R_B = 1.55728$).

To calculate the spectral density $\widetilde{\chi}(k)$, we decorate the systems by circumscribing disks of radius R_A and R_B centered around the point particles of species A and B, respectively. Since our derivation in Sec. 6.2 requires the disks to be nonoverlapping, we chose the largest possible radii that satisfy this condition. In the case of a Kob-Andersen glass, A particles are often located next to one another, while B particles can be further apart. This leads to our decision to use the distances between the closest A–A and A–B pairs of particles to define the particle radii for any particular configuration. Thus, there will be variability in the radii used from configuration to configuration, but these radii fluctuations are extremely small. Figure 6.6 shows part of a glass configuration decorated using this procedure.

In an identical fashion to the Z2 Dzugutov system, we use the change in slope of the total energy in terms of the temperature to estimate the glass transition temperature T_g for the Kob-Andersen system. Since the Kob-Andersen system that we analyze is two-dimensional, its harmonic contribution to the energy is $2k_BT$, which we subtract

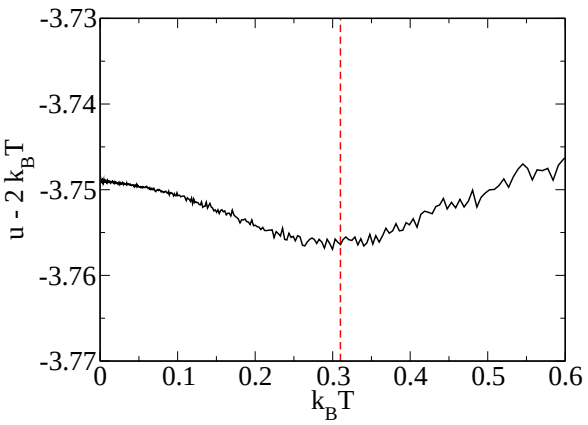

Figure 6.7: (Color online) Strictly anharmonic portion of the total average energy (kinetic and potential) per particle $u - 2k_BT$ of the system in terms of the thermostat temperature T. This is obtained by averaging 10 cooling simulations of supercooled Kob-Andersen systems using $\tau_{10} = 400$. $2k_BT$ has been subtracted from the energy to help identify the glass transition. The glass transition temperature $T_g \sim 0.31$ is estimated by finding the temperature at which the function slope changes the most rapidly. The vertical dashed line is located at $T = T_g$. The energy scale is normalized through our choice of potential parameters (see Sec. 6.3).

from the total average energy per particle u to detect any change of slope. The result obtained from Fig. 6.7 is $T_g \sim 0.31$, which is reasonably close to the previously-reported value of $T_g = 0.33$ [28].

As in the case of Z2 Dzugutov systems, the spectral densities $\widetilde{\chi}(k)$ for Kob-Andersen liquids, supercooled liquids, and glasses have nearly linear behavior for $k \lesssim 1$. It is thus possible to prescribe a linear fit to extrapolate the values of $\widetilde{\chi}(k = 0)$, which is required to calculate $\widetilde{C}(k = 0)$ using Eq. (6.22). We again define a length scale based on the $\widetilde{C}(k = 0)$:

$$\xi_C \equiv \left[-\widetilde{C}(0)\right]^{1/d}, \tag{6.42}$$

where d is the Euclidean dimension. Figure 6.9(a) shows the large change in value of $\widetilde{C}(k = 0)$ as the Kob-Andersen liquids are supercooled, leading to the length scale ξ_C to increase by a factor larger than 5 between the fluid states and the zero-temperature glassy states.

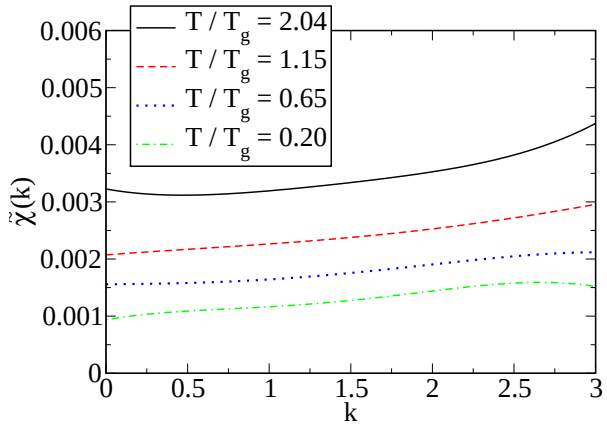

Figure 6.8: (Color online) Spectral density $\widetilde{\chi}(k)$ versus wavenumber k for Kob-Andersen $A_{65}B_{35}$ systems supercooled using $\tau_{10} = 400$. The curves have been averaged over 10 realizations and fitted using fourth degree polynomials. The type of fits have been chosen for their ability to reproduce accurately the features of the structure factors for the range presented ($0 < k < 3$). The disk radii for the decorations are calculated independently for each configuration.

As mentioned in Sec. 6.2.2, there is a second generalization of the direct correlation function which does not require any *a priori* knowledge about the particle shapes. Instead, one can use the matrix direct correlation function $\mathbf{C}(r)$ and its Fourier transform $\widetilde{\mathbf{C}}(k)$. As can be observed in Fig. 6.10, the qualitative behavior of the smallest eigenvalue of $\widetilde{\mathbf{C}}(k)$ in the $k \to 0$ limit is strikingly close to the behavior of $\widetilde{C}(k)$ in the same limit. This indicates that our decoration choice is appropriate for detecting long-range density fluctuations in Kob-Andersen glasses and supercooled liquids.

Since the compressibility relation (6.39) applies only to single-component systems, we must generalize the nonequilibrium index X for mixtures. The compressibility relation for multicomponent systems at equilibrium, is given by [29]:

$$\kappa_T k_B T = \frac{|\mathbf{B}|}{\sum_{\alpha=1}^{M} \sum_{\beta=1}^{M} |\mathbf{B}|_{\alpha\beta}}, \tag{6.43}$$

where the components $B_{\alpha\beta}$ of the matrix $\mathbf{B}$ are

$$B_{\alpha\beta} = \frac{\sqrt{N_\alpha N_\beta}}{V} \lim_{k\to 0} S_{\alpha\beta}(k), \tag{6.44}$$

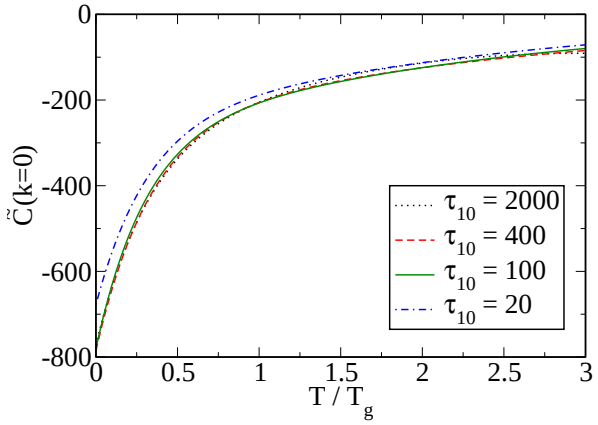

(a)

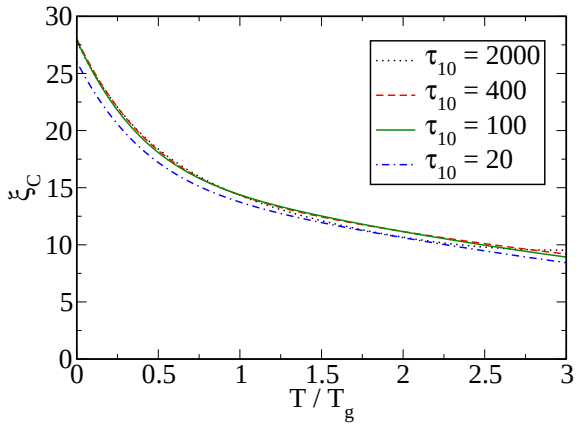

(b)

Figure 6.9: (Color online) Growing length scales for two-dimensional Kob-Andersen systems. For each cooling schedule, the results have been averaged over 10 realizations and fitted to the sum of an exponential and a quadratic functions to smooth out the numerical noise. (a) Limit of $\widetilde{C}(k)$ for $k \to 0$, calculated using the linear fits of $\widetilde{\chi}(k)$. (b) The static length scale ξ_C, defined by relation (6.42), associated with these systems.

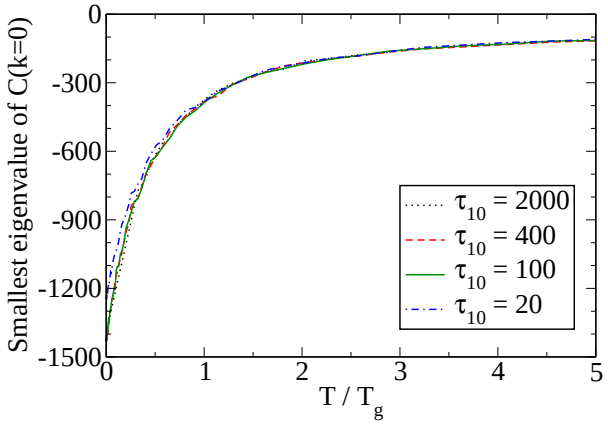

Figure 6.10: (Color online) Smallest eigenvalue of $\lim_{k\to 0}\mathbf{C}(k)$, calculated using a linear fit of the matrix structure factor $\mathbf{S}(k)$. While the qualitative behavior of this eigenvalue can be compared to $\widetilde{C}(k=0)$ (see Fig. 6.9(a)), their quantitative values cannot directly be compared because they have different units: $\widetilde{C}(k)$ has units of volume, while $\widetilde{\mathbf{C}}(k)$ is dimensionless.

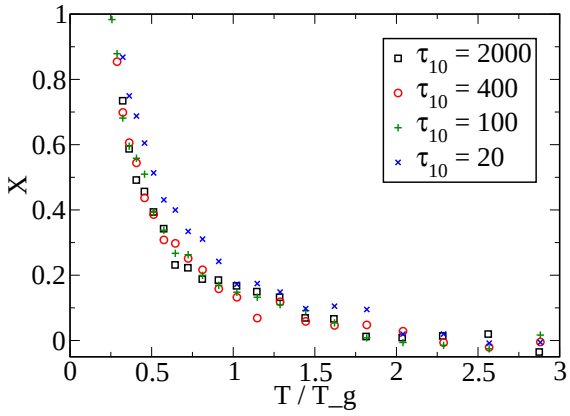

Figure 6.11: (Color online) Nonequilibrium index X for Kob-Andersen systems supercooled using various cooling schedules defined in Eq. (6.45).

$|\mathbf{B}|$ is the determinant of $\mathbf{B}$, and $|\mathbf{B}|_{\alpha\beta}$ is the $\alpha\beta$ minor of $\mathbf{B}$. The nonequilibrium index X for multicomponent systems can now be defined by using the mismatch between the left and right sides of Eq. (6.43), that is,

$$X \equiv \frac{|\mathbf{B}|}{\kappa_T k_B T \sum_{\alpha=1}^{M} \sum_{\beta=1}^{M} |\mathbf{B}|_{\alpha\beta}} - 1. \tag{6.45}$$

As for single-component systems, the isothermal compressibility for this multicomponent system is obtained by computing the virial pressure response to an incremental change in volume using Eq. (6.41).

For the Kob-Andersen system, we use a change of volume $\Delta V/V = 0.2\%$ and the pressure is sampled from $t = 20$ to $t = 40$, where $t = 0$ denotes the time at which the quenching is halted and the system is compressed. As can be seen in Fig. 6.11, X is zero [27] for $T > 2T_g$. Similarly to the phenomenon observed in the case of the Z2 Dzugutov system (see Fig. 6.4), X increases up to a value of a value of ~ 0.15 at $T = T_g$. The asymptotic behavior of X for $T < T_g$ is again the consequence of the system inability to relax in a time comparable to the cooling schedule time per decade τ_{10}.

6.5 Conclusions and Discussion

We have demonstrated here that the static structural length scales ξ_c and ξ_C are able to distinguish subtle structural differences between glassy and liquid states, which extends the analogous results for metastable hard spheres [7] to atomic thermal systems. Since these length scales are based on the volume integral of the direct correlation function $c(r)$ and its generalization $C(r)$, respectively, their growth as a liquid is cooled past its glass transition is a sign of the presence of long-range correlations in the glassy state that are not present in liquids. Additionally, the continuing increase of ξ_c and ξ_C past the glass transition indicates that, while particles primarily undergo

sequences of local rearrangements, the glass may still exhibit order on a significantly larger length scale as the system continues to cool. Our results using two-dimensional Kob-Andersen binary mixtures and three-dimensional Z2 Dzugutov single-component systems, as well as the previous results for MRJ packings as evidence, we postulate that these length scales are relevant in various glasses. This includes not only atomic systems possessing pair potentials with steep repulsions and short-range attractions, but network glasses as well. For example, in a recent computational study [30], which is supported by recent experimental results [31], it was shown that realistic models of amorphous silicon can be constructed to be nearly hyperuniform, which implies that such glassy tetrahedrally-coordinated networks are characterized by a large static length scale ξ_c. We also have shown that the nonequilibrium index X is positively correlated with a characteristic relaxation time scale, since they both increase as a system is supercooled. Our results also show that a glass cannot be viewed structurally as a "frozen liquid".

An interesting issue concerns the explication of the underlying geometrical reasons for the negative algebraic tail in the pair correlation function [13], which also has been observed in hard-sphere systems [7]. The local geometric diversity of particle arrangements in an amorphous solid medium inevitably creates short-range density fluctuations. In particular, this is true for the nearly hyperuniform cases examined in this study. Without being too specific, one can formally divide a "jammed" particle configuration into two equal subsets containing particles experiencing either lower or higher local densities than the overall system average. The fact that the pair correlation functions display negative algebraic tails with increasing separation r has basic implications for the relative spatial distributions of these low and high local density particles. In particular, it indicates that large numbers of either particle type cannot fit together to form arbitrarily large clusters that dominantly exclude the other particle types. Instead, their spatial patterns evidently involve interpenetrat-

ing percolating networks in three dimensions and highly non-convex clusters in two dimensions. The detailed statistical geometric description of these patterns and why they generate algebraic pair correlation function tails constitutes an important area for future investigation.

The quantity X introduced earlier in Eq. (6.40) as a measure of deviation from thermal equilibrium can be usefully interpreted in terms of system occupancy on the many-body potential energy landscape [32]. Specifically, this focuses on the comparative behaviors of isothermal compressibility at high-temperature thermal equilibrium in the liquid phase as opposed to the measured isothermal compressibility in the non-equilibrium glass phase in the $T \rightarrow 0$ limit. In the former case, an incremental pressure change and accompanying volume change will include shifts in occupancy probabilities for the separate basins that tile the landscape; these shifts involve interbasin local particle rearrangements that act to enhance the volume change induced by the pressure perturbation. In contrast, at very low temperatures, the system is trapped in its initial basin; intrabasin vibrational motions have insufficient amplitude to allow the system to take advantage of the previous kinds of local particle rearrangements. The resulting absence of enhanced volume change due to those interbasin transitions reduces isothermal compressibility, causing X to increase above zero.

Bibliography

[1] P. M. Chaikin and T. C. Lubensky, *Principles of Condensed Matter Physics* (Cambridge, 1995).

[2] L. Berthier, G. Biroli, J.-P. Bouchaud, J. W. Kob, K. Miyazaki, and D. R. Reichman, *Spontaneous and induced dynamic fluctuations in glass formers. I. General results and dependence on ensemble and dynamics*, J. Phys. Chem. **126**, 184503 (2007).

[3] S. Karmakar, C. Dasgupta, and S. Sastry, *Growing length and time scales in glass-forming liquids*, PNAS US **106**, 3675 (2009).

[4] D. Chandler and J. P. Garrahan, *Dynamics on the Way to Forming Glass: Bubbles in Space-Time*, Ann. Rev. Phys. Chem. **61**, 191 (2010).

[5] V. Lubchenko and P. G. Wolynes, *Theory of Structural Glasses and Supercooled Liquids*, Ann. Rev. Phys. Chem. **58**, 235 (2006).

[6] G. M. Hocky, T. E. Markland, and D. R. Reichman, *Growing Point-to-Set Length Scale Correlates with Growing Relaxation Times in Model Supercooled Liquids*, Phys. Rev. Lett. **108**, 225506 (2012).

[7] A. B. Hopkins, F. H. Stillinger, and S. Torquato, *Nonequilibrium static diverging length scales on approaching a prototypical model glassy state*, Phys. Rev. E, **82**, 021505 (2012).

[8] S. Torquato, T. M. Truskett, and P. G. Debenedetti, *Is Random Close Packing of Spheres Well Defined?*, Phys. Rev. Lett. **84**, 2064 (2000).

[9] S. Torquato and F. H. Stillinger, *Jammed hard-particle packings: From Kepler to Bernal and beyond*, Rev. Mod. Phys. **82**, 2633 (2010).

[10] S. Torquato and F. H. Stillinger, *Toward the jamming threshold of sphere packings: Tunneled crystals*, J. App. Phys. **102**, 093511 (2007); *Erratum: "Toward the jamming threshold of sphere packings: Tunneled crystals"*, J. App. Phys. **103**, 129902 (2008).

[11] S. Torquato and F. H. Stillinger, *Local density fluctuations, hyperuniformity, and order metrics*, Phys. Rev. E **68**, 041113 (2003).

[12] J. P. Hansen and I. R. McDonald, *Theory of Simple Liquids, 3rd ed.* (Academic, 2006).

[13] A. Donev, F. H. Stillinger, and S. Torquato, *Unexpected Density Fluctuations in Jammed Disordered Sphere Packings*, Phys. Rev. Lett. **95**, 090604 (2005a).

[14] J. P. K. Doye, D. J. Wales, F. H. M. Zetterling, and M. Dzugutov, *The favored cluster structures of model glass formers*, J. Chem. Phys. **118**, 2792 (2003).

[15] W. Kob and H. C. Andersen, *Scaling Behavior in the β-Relaxation Regime of a Supercooled Lennard-Jones Mixture*, Phys. Rev. Lett. **73**, 1376 (1994).

[16] M. D. Rintoul and S. Torquato, *Metastability and Crystallization in Hard-Sphere Systems*, Phys. Rev. Lett. **77**, 4198 (1996); M. D. Rintoul and S. Torquato, *Computer simulations of dense hardsphere systems*, J. Chem. Phys. **105**, 9258 (1996).

[17] K. S. Schweizer, *Relationships between the single particle barrier hopping theory and thermodynamic, disordered media, elastic, and jamming models of glassy systems*, J. Chem. Phys. **127**, 16506 (2007).

[18] C. E. Zachary, Y. Jiao, and S. Torquato, *Hyperuniform Long-Range Correlations are a Signature of Disordered Jammed Hard-Particle Packings*, Phys. Rev. Lett. **106**, 178001 (2011); *Hyperuniformity, quasi-long-range correlations, and void-space constraints in maximally random jammed particle packings. I. Polydisperse spheres*, Phys. Rev. E, **83**, 051308 (2011); *Hyperuniformity, quasi-long-range correlations, and void-space constraints in maximally random jammed particle packings. II. Anisotropy in particle shape*, Phys. Rev. E 83, 051309 (2011).

[19] The hyperuniformity of maximally random jammed packings has been extended to apply to polydisperse spheres and nonspherical objects in terms of the spectral density $\widetilde{\chi}(k)$ [18].

[20] S. Torquato and G. Stell, *Microstructure of twophase random media. V. The npoint matrix probability functions for impenetrable spheres*, J. Chem. Phys. **82**, 980 (1985).

[21] S. Torquato, *Random Heterogeneous Materials* (Springer, 2002).

[22] R. J. Baxter, *Ornstein–Zernike Relation and Percus–Yevick Approximation for Fluid Mixtures*, J. Chem. Phys. **52**, 4559 (1970).

[23] Using expression (6.32) to write $\mathbf{S}(\mathbf{k})$ for a single configuration, we can express $\mathbf{S}(\mathbf{k})$ as the product of a non-zero vector times its Hermitian transpose, the rank of which (equal to the number of non-zero eigenvalues) is 1. Taking an ensemble average of Eq. (6.32) breaks this symmetry, since the sum of M vectors multiplied by their transpose has a rank of M if the vectors are linearly independent.

[24] W. G. Hoover, *Canonical dynamics: Equilibrium phase-space distributions*, Phys. Rev. A **31**, 1695 (1985).

[25] B. Widom, *New Model for the Study of Liquid–Vapor Phase Transitions*, J. Chem. Phys. **52**, 3888 (1970).

[26] P. G. Debenedetti and F. H. Stillinger, *Supercooled liquids and the glass transition*, Nature (London) **410**, 259 (2001).

[27] Note that we found a very small systematic error due to a combination of the following factors: the thermostat, relaxation during the compressibility computation, and the finite difference method. To correct for this systematic error, we added to the computed value of X a constant such as to ensure that $X = 0$ for the high-temperature liquid phase, for which the compressibility relations (6.39) and (6.43) are satisfied. This constant is equal to 0.05 for the Z2 Dzugutov potential, and 0.015 for the Kob-Andersen potential.

[28] R. Brüning, D. A. St-Onge, S. Patterson, and W. Kob, *Glass transitions in one-, two-, three-, and four-dimensional binary Lennard-Jones systems*, J. Phys.: Conden. Matter **21**, 035117 (2009).

[29] J. G. Kirkwood and F. P. Buff, *The Statistical Mechanical Theory of Solutions. I*, J. Chem. Phys. **19**, 774 (1951).

[30] M. Hejna, P. J. Steinhardt, and S. Torquato, *Nearly hyperuniform network models of amorphous silicon*, Phys. Rev. B **87**, 245204 (2013).

[31] G. Long, R. Xie, S. Weigand, S. Moss, S. Roorda, S. Torquato, and P. Steinhardt, Proceedings of the Minerals, Metals and Materials Society (March 11th-15th, 2012), Orlando, FL (to be published); R. Xie, G. G. Long, S. J. Weigand, S. C. Moss, T. Carvalho, S. Roorda, M. Hejna, S. Torquato, and P. J. Steinhardt,

Hyperuniformity in armorphous silicon: measurement of the infinite-wavelength limit of the structure factor, Proceedings of the National Academy of Sciences. Published ahead of print July 29, 2013.

[32] P. G. Debenedetti, *Metastable Liquids* (Princeton University Press, Princeton, NJ, 1996).